

Multihazard Performance-Based Assessment of Multi- Storey Steel Braced Frame Buildings

Mohamad Dakour

A Thesis

in

The Department

of

Building, Civil and Environmental Engineering

Presented in Partial Fulfilment of the Requirements
for the Degree of Master of Applied Science (Civil Engineering) at

Concordia University

Montreal, Quebec, Canada

April 2022

© Mohamad Dakour,2022

CONCORDIA UNIVERSITY

School of Graduate Studies

This is to certify that the thesis prepared

By: Mohamad Dakour

Entitled Multihazard Performance-Based Assessment of Multi-Storey Steel Braced Frame Buildings

and submitted in partial fulfillment of the requirements for the degree of:

Master of Applied Science (Civil Engineering)

complies with the regulations of the University and meets the accepted standards with respect to originality and quality.

Signed by the final Examining Committee:

_____	Chair
Dr. A. Bhowmick	
_____	Examiner
Dr. E. Erkmen	
_____	Examiner
Dr. A. Bhowmick	
_____	Co-Supervisor
Dr. L. Tirca	
_____	Co-Supervisor
Dr. T. Stathopoulos	

Approved by

Dr. M. Nik-Bakht, Graduate Program Director

2022

Dr. M. Debbabi, Dean of Faculty

ABSTRACT

Multihazard Performance-Based Assessment of Multi-Storey Steel Braced Frame Buildings

Mohamad Dakour

Seismic codes have evolved to the point that allows integrating Structural System Reliability of buildings into the seismic analysis by limiting the building damage under earthquake input, while keeping a reasonable margin of safety. However, wind design following the major international standards, including the National Building Code of Canada, remains prescriptive and overall conservative.

Current wind design uses the first significant yielding of a structural member as a strength limit state and does not explore nonlinearity beyond the design level, neither accounts for the inherent system overstrength. In other words, it does not explore the wind response of the lateral force resisting system (LFRS) from yielding to the system's failure mechanism. For a building located in a seismic region, the LFRS has well-detailed ductile fuses that are allowed to yield under seismic loads and dissipate energy through hysteresis but are required to respond elastically under wind load. Further, the return period for the seismic and wind loads are not compatible in the building codes; hence, at design level, the seismic hazard is associated to 2500-year return period and the wind hazard (ultimate limit state) to 500-year return period.

This research presents a multihazard assessment of two multi-storey concentrically braced frame (CBF) buildings located in Montreal, Quebec, where both wind and earthquake load are critical.

The collapse margin safety under earthquake load is conducted according to FEMA P695 (2009) procedure and the wind reliability criterion is verified as per the ASCE PBWD (2019) pre-standard methodology.

In this study, the nonlinear dynamic response of the LFRSs of studied buildings was analyzed to different seismic and wind hazard levels using two-dimensional numerical models developed in the OpenSees framework. Then, these models were independently subjected to a set of seven artificial ground motions and aerodynamic data derived from the Tokyo Polytechnic University (TPU) aerodynamic database. Using data from seismic and wind Incremental Dynamic Analyses (IDA), the fragility curves were constructed and the failure mechanisms of multi-storey Concentrically Braced Frames (CBF) under wind and earthquake was identified. The progressive development of dynamic response from yielding to collapse is also discussed.

The study concluded that more flexibility could be permitted to wind design by accounting for the inherent structural overstrength and limited ductility, while challenging aspects may still arise due to inherent differences between earthquake and wind loads.

Acknowledgments

First and foremost, I owe my sincere gratitude to Professor Lucia Tirca and Professor Theodore Stathopoulos for offering me the chance to switch to the Master of Applied Science (MASc) program and for their continuous support throughout my entire study. My deep thanks to Prof. Tirca from whom I have learned so much about the concepts of designing the steel structures under seismic loads and to Prof. Stathopoulos who is simply one of the best in the field of building aerodynamics and wind effects. I have had the privilege to work under their supervision for the past two years and I hope to continue with them in the future.

Besides my supervisors, I would like to gratefully thank Dr. Anastasia Athanasiou who has helped me in my work with her precious advice and the insightful comments. Thank you so much.

Financial support from the Natural Sciences and Engineering Research Council of Canada (NSERC) and “Le Centre d'études interuniversitaire des structures sous charges extrêmes (CEISCE), financed by Fonds de Recherche du Québec-Nature et Technologies (FRQNT) are gratefully acknowledged.

I also would like to express my deepest gratitude to my parents and my two brothers whom I have not seen for 7 years due to the war conditions my country is going through. Your endless love and sacrifice will not be in vain. I love you.

Finally, I would like to thank my caring and compassionate beautiful wife for her support along the way to reach my goals. Also, my little beloved 5-years old girl, Jasmine, who is always helping me in her own way and draws her amazing paintings on my important papers. You are the light of my life and I love you both.

Table of Contents

List of Figures	ix
List of Tables	xviii
List of Abbreviations	xx
1. CHAPTER 1. Introduction	1
1.1 General	1
1.2 Objectives and Scope	3
1.3 Methodology	4
1.4 Thesis Organization.....	6
2. CHAPTER 2. Literature Review	8
2.1 General	8
2.2 Earthquake Load Design According to NBC 2015	9
2.2.1 Equivalent Static Force Procedure.....	9
2.2.2 P- Δ Effect and Notional loads.....	11
2.2.3 Capacity Design Principle.....	12
2.2.4 Dynamic Analysis Procedure.....	14
2.3 Wind Load Design According to NBC 2015	14
2.3.1 General	14
2.3.2 Wind Load Calculation.....	15

2.3.3	Static Procedure	16
2.3.4	Dynamic Procedure.....	18
2.3.5	Wind Tunnel Procedure	19
2.4	The Open System for Earthquake Engineering Simulation	20
2.4.1	Centrically Braced Frames model developed in OpenSees.	20
2.5	Performance-Based Design	26
2.5.1	Performance-Based Seismic Design (PBSD)	26
2.5.2	Incremental Dynamic Analysis.....	29
2.5.3	Fragility Analysis and Collapse Margin Ratio (CMR).....	31
2.5.4	Performance-Based Wind Design (PBWD).....	35
2.5.5	Previous Studies on Performance-Based Multihazard Design	42
3.	CHAPTER 3. Seismic and Wind Design of Centrically Braced Frame Buildings	45
3.1	Case Study.....	45
3.1.1	Building Design	47
3.1.2	Design of the 12-storey MD-CBFs building ($R_d = 3$).....	50
3.1.3	Design of the 16-storey LD-CBFs building ($R_d = 2$)	56
4.	CHAPTER 4. Modeling and Nonlinear Dynamic Analysis	64
4.1	Seismic data for the Nonlinear Dynamic Analysis	64
4.2	Wind Aerodynamic Database of High-rise Buildings.....	67

4.2.1	Monte Carlo Simulations	73
4.3	Numerical Model in OpenSees	74
5.	CHAPTER 5. Performance Assessment.....	77
5.1	Nonlinear Response Assessment at Design Level	77
5.1.1	Seismic response of buildings under design spectrum-compatible ground motion suite	78
5.1.2	Wind response of buildings to selected random events (Rand #1 - Rand #5) scaled to the design level	86
5.2	Incremental Dynamic Analysis of Buildings under Seismic Loads.....	91
5.3	Assessment of the Collapse Safety under Seismic Loads	98
5.4	Incremental Dynamic Analysis under Wind Loads	101
5.5	Wind Assessment.....	111
5.6	Comparison of buildings response under Wind and Earthquake	112
6.	CHAPTER 6. Conclusions and Future Work	115
6.1	Conclusions	115
6.2	Future Work	117
7.	References	119

List of Figures

Fig. 2.1. Decision tree for selecting appropriate design method for the main structural system in accordance with NBC (2015).....	16
Fig. 2.2. Modeling the HSS brace: a) numerical model of the HSS brace with end connection, b) discretization technique applied to HSS brace cross section, (Tirca et al 2015).	24
Fig. 2.3. Illustration of HSS brace to frame gusset plate connection model (Hsiao et al 2012)...	25
Fig. 2.4. The effect of out-of-straightness on the buckling strength of S1B specimen (Tirca and Chen, 2014).....	25
Fig. 2.5. Representation of the four Performance Levels (Fajfar et al. 2004).	27
Fig. 2.6. Flowchart of the performance assessment methodology (FEMA P-85, 2018).	29
Fig. 2.7. IDA curves of a 5-storey steel braced frame ($T_I = 1.8$ s) under 4 different ground motions that input various responses: a) softening response, b) a bit of hardening response, c) severe hardening and d) weaving behaviour (Vamvatsikos and Cornell 2002).....	30
Fig. 2.8. IDA response of a 5-storey braced frame building: a) IDA curves under 30 ground motions and b) the 16%, 50% and 84% fractile curves in log-log scale (Vamvatsikos and Cornell 2002).	31

Fig. 2.9. Building response under a suite of GMs: a) IDA curves and b) collapse fragility curve using a lognormal cumulative distribution function, (FEMA P695, 2009).	32
Fig. 2.10. Variation of collapse fragility curve as a function of total uncertainty $\beta_{TOT} = 0.4; 0.65$	33
Fig. 2.11. Idealized nonlinear static pushover curve (FEMA P695, 2009).	35
Fig. 2.12. Performance Based Wind Engineering Framework in accordance with Griffis et al (2012).	38
Fig. 2.13. Wind tunnel test for a tall building in a compound (El Damatty and Elezaby, 2018). 40	
Fig. 2.14. Load-displacement curves and seismic performances. (Jeong et al. 2021).	41
Fig. 2.15. PBWE Framework in accordance with Bezabeh et al. (2020).	42
Fig. 2.16. Probability of hurricane and earthquake damage in Charleston, USA: a) minimum hazard-resistance construction practice, b) enhanced hazard-resistance construction practice, (Li et al., 2009).	44
Fig. 3.1. Building plan and CBFs distribution for the 12-storey and 16-storey buildings. All dimensions are in meter.	46
Fig. 3.2. 2-D elevations of buildings with CBF-1 acting in the N-S direction carrying $\frac{1}{4}$ of the load with the participating gravity columns: a) 12-storey; b) 16-storey. Dimensions are in meter. ..	46

Fig. 3.3. 3D ETABS model for the 12-storey CBF building: a) structural components and b) the Lateral Force Resisting System (LFRS).	50
Fig. 3.4. Vertical distribution of seismic loads and wind loads in the N-S direction (MD-CBF1) over the height of the 12-storey MD-CBF building ($R_d = 3.0$).....	54
Fig. 3.5. 12-storey MD-CBF building: (a) demand to capacity ratio of the axial forces in the HSS braces, (b) elastic interstorey drift under earthquake and wind at serviceability level.....	56
Fig. 3.6. Vertical distribution of seismic loads and wind loads along LD-CBF1 of 16-storey building ($R_d = 2.0$), considering N-S direction.	61
Fig. 3.7. 16-storey LD-CBF building: a) demand to capacity ratio of the axial forces in the HSS braces, b) elastic interstorey drift for earthquake and wind at serviceability level.....	63
Fig. 4.1. The seven simulated ground motions used in NRHA.	65
Fig. 4.2. Design spectrum for Montreal, Site class C, and response spectra of 7 spectrum compatible ground motions and their mean for: a) 12-storey MD-CBF and b) 16-storey LD-CBF buildings.....	66
Fig. 4.3. TPU database: a) geometric dimensions query ratio for high-rise buildings, and b) vertical profiles of incoming wind flow for $\alpha = 1/6$ & $1/4$ (www.wind.arch.t-kougei.ac.jp/info_center/windpressure/highrise/Homepage/homepageHDF.htm).....	68

Fig. 4.4. Locations of the pressure taps on the windward, leeward and sideward faces of the considered high-rise building model with $H = 0.2\text{m}$, $B = 0.2\text{m}$, $D = 0.1\text{m}$, length scale = $1/400$ (http://www.wind.arch.t-kougei.ac.jp/info_center/windpressure/highrise/Test_Result/T212_4_channels.jpg). 69

Fig. 4.5. Peak values of the net pressure coefficients, $C_p C_{g,max}$ derived from the TPU database for wind directions $0-90^\circ$ and assessed at each storey level for the: a) 12-storey and b) 16-storey buildings..... 70

Fig. 4.6. Positive extreme wind pressure coefficients on a high-rise building at windward, leeward and sideward faces of the TPU scaled model with $H = 0.2\text{ m}$, $B = 0.2\text{ m}$, $D = 0.1\text{ m}$, model scale = $1/400$, $\theta = 0^\circ$ (http://www.wind.arch.t-kougei.ac.jp/info_center/windpressure/highrise/Test_Result/T212_4_000_max.jpg). 70

Fig. 4.7. Net pressure coefficient time histories at the floor levels of the 12-storey building model for wind acting at $\theta=0^\circ$. The mean coefficient is shown in red. 72

Fig. 4.8. Net pressure coefficient time histories at the floor levels of the 16-storey building model for wind acting at $\theta=0^\circ$. The mean coefficient is shown in red. 72

Fig. 4.9. Peak and mean values of the experimental wind load compared to the design wind load ($1.4W$) calculated as per the (NBC, 2015) for the, a) 12-storey building, b) 16-storey building. 73

Fig. 4.10. The typical floor plan and $\frac{1}{4}$ floor area considered in the analysis. 75

Fig. 4.11. OpenSees model of the a) 12-storey and b) 16-storey buildings with CBF-1 acting in the N-S direction and carrying $\frac{1}{4}$ of the load with the participating gravity columns.....	75
Fig. 5.1. The ISD distribution along the building height under GMs scaled to D.L.: a) 12-storey MD-CBF ($R_d = 3$) and b) 16-storey LD-CBF ($R_d = 2$).....	79
Fig. 5.2. The RISD distribution along the building height under GMs scaled to D.L.: a) 12-storey MD-CBF ($R_d = 3$) and b) 16-storey LD-CBF ($R_d = 2$).....	80
Fig. 5.3. The FA distribution along the building height under GMs scaled to D.L.: a) 12-storey MD-CBF ($R_d = 3$) and b) 16-storey LD-CBF ($R_d = 2$).....	81
Fig. 5.4. Mean ISD distribution along the 12-storey building height under GMs scaled to D.L., when the 1 st , 6 th and 7 th storey braces are increased for wind demand ($W=Wind$).	82
Fig. 5.5. Response of the 12-storey MD-CBF and 16-storey LD-CBF buildings under M7C1_25_6 record scaled to D.L.: a)-b) scaled accelerogram, c) time history ISD series at roof.	83
Fig. 5.6. Hysteresis response of the left and right HSS braces of top floor of studied buildings under M7C1_25_6 scaled to D.L.: a)-b) 12-storey MD-CBF and c)-d) 16-storey LD-CBF.....	84
Fig. 5.7. Response of the 16-storey LD-CBF building under M7C1_13_8 scaled to D.L.: a) accelerogram, b) time history response of ISD of 14 th floor, c)-d) hysteresis response of the left and right HSS braces of 14 th floor.	85

Fig. 5.8. First storey response of the 12-story MD-CBF building under Rand #3 realization, scaled to design level (<i>ULS</i>): a) 120 min. drag force history (Rand #3), b) time history of ISD and c)- d) hysteresis response of left and right HSS braces.	87
Fig. 5.9. Second storey response of the 16-storey LD-CBF building under Rand #5 realization, scaled to design level (<i>ULS</i>): a) 120 min. drag force history (Rand #5), b) time history of ISD and c)- d) hysteresis response of left and right HSS braces.	88
Fig. 5.10. Distribution of ISDs along the building height under wind Rand #1 - #5 at (<i>SLS</i>) and (<i>ULS</i>) for: a) 12-storey MD-CBF and b) 16-storey LD-CBF.....	89
Fig. 5.11. Distribution of FAs along the building height under wind Rand #1 - #5 at (<i>SLS</i>) and (<i>ULS</i>) for: a) 12-storey MD-CBF and b) 16-storey LD-CBF.....	90
Fig. 5.12. IDA curves in terms of ISD resulted under the incremented GM suite: a) 12-storey MD-CBF building and b) 16-storey LD-CBF building.....	92
Fig. 5.13. IDA curves expressed in terms of RISD resulted under the incremented GM suite: a) 12-storey MD-CBF building and b) 16-storey LD-CBF building.....	93
Fig. 5.14. IDA curves expressed in terms of FA resulted under the incremented GM suite: a) 12-storey MD-CBF building and b) 16-storey LD-CBF building.	94
Fig. 5.15. Response of 12-storey MD-CBF building under the GM suite scaled to $2.4S_a(T_l)$: a) ISDs, b) RISDs and, c) FAs.....	95

Fig. 5.16. Response of 16-storey LD-CBF building under the GM suite scaled to $2.4S_a(T_1)$: a) ISDs, b) RISDs and, c) FAs. 95

Fig. 5.17. Failure mechanism of buildings associated to Near Collapse limit state: a) 12-storey MD-CBF under M7C2_50.3 at $S_a(T_1) = 0.272g$ intensity and b) 16-storey LD-CBF buildings under M7C1_25.8 at $S_a(T_1) = 0.184g$ intensity. 96

Fig. 5.18. Response of 12-storey MD-CBF building under M7C2_50_3 record scaled to near-collapse intensity: a) input ground acceleration, b) interstorey drift, c)-d) hysteresis response of the 1st floor left and right HSS braces. 97

Fig. 5.19. Response of 16-storey LD-CBF building under M7C1_28_8 record scaled to near-collapse intensity: a) input ground acceleration, b) interstorey drift, c)-d) hysteresis response of the 1st floor left and right HSS braces. 98

Fig. 5.20. Seismic fragility curves at near collapse for the 12-storey MD-CBF and 16-storey LD-CBF buildings. 100

Fig. 5.21. IDA curves in term of ISD under Rand #1 - #5 wind: a) 12-storey MD-CBF building, and b) 16-storey LD-CBF buildings. 103

Fig. 5.22. IDA curves in term of RISD under Rand #1 - #5 wind: a) 12-storey MD-CBF building and, b) 16-storey LD-CBF building. 104

Fig. 5.23. IDA curves in terms of FAs under Rand #1 - #5: a) 12-storey MD-CBF building and, b) 16-storey LD-CBF building.....	105
Fig. 5.24. Distribution of EDPs along the height of 12-storey MD-CBF building subjected to Rand #1-#5 winds scaled to $V_C = 58.67$ m/s (note that $V_C = V_{C, \#3} = 58.67$ m/s means the near-collapse limit state under Rand #3): a) ISD, b) RISD and c) FA.....	106
Fig. 5.25. Distribution of EDPs along the height of 16-storey LD-CBF building subjected to Rand #1-#5 winds scaled to $V_C = 58.67$ m/s (note that $V_C = V_{C, \#3} = 58.67$ m/s is the near-collapse limit state under Rand #3): a) interstorey drift, b) residual drift and c) floor acceleration.	106
Fig. 5.26. Failure mechanism of buildings associated to near collapse: a) 12-storey MD-CBF under wind Rand #3 and b) 16-storey LD-CBF under wind Rand #5	107
Fig. 5.27. Response of the 3 rd floor of 12-story MD-CBF building under Rand #3 realization scaled to near collapse intensity: a) time history drag force at 3 rd floor, b) time history ISD and c)-d) hysteresis behaviour of the left and right HSS braces.	108
Fig. 5.28. Response of the 1 st floor of 16-storey LD-CBF building under Rand #5 realization scaled to the near collapse intensity: a) time history drag force at 1 st floor, b) time history ISD, and c)-d) hysteresis behaviour of the left and right braces.....	109
Fig. 5.29. Wind collapse fragility curves for the 12-storey MD-CBF and the 16-storey LD-CBF buildings.....	112

Fig. 5.30. Progressive development of peak interstorey drift under earthquake and wind incremented intensity for the 12- and 16-storey buildings under: a)-b) M7C2_50.3 and wind Rand #3 for 12-st MD-CBF and, c)-d) M7C1_25.8 and wind Rand #5 for 16-st LD-CBF building. . 114

List of Tables

Table 2.1. Seismic Data for Site Class C, Montreal.	10
Table 3.1. Vertical distribution of seismic force over the height of the 12-storey MD-CBFs building, $R_d = 3$, Site class C, Montreal.	52
Table 3.2. Calculation of the wind force in the N-S direction for the 12-storey MD-CBF building, $R_d = 3$ in Montreal.	53
Table 3.3 . Members' sections for MD-CBF1 of the 12-storey building and the governing load (1.0E) or (1.4W).	55
Table 3.4. Vertical distribution of the seismic shear force over the height of the 16-storey LD-CBFs building, $R_d = 2$, Site class C, Montreal.	58
Table 3.5. Calculation of the wind force in the N-S direction for the 16-storey LD-CBFs building, $R_d = 2$ in Montreal.	60
Table 3.6. Members' sections for LD-CBF1 of the 16-storey building and the governing load (1.0E) or (1.4W).	62
Table 4.1. Ground motion characteristics and scaling factors (SF) for the 12- and 16-storey buildings.	66
Table 5.1. Characteristics of the studied CBFs buildings.	77

Table 5.2. Parameters for collapse safety verification of studied buildings under seismic GMs	100
Table 5.3. Summary of seismic demand and response parameters at and beyond design level.	101
Table 5.4. Summary of wind demand and response parameters at and beyond design level.	110
Table 5.5. Total system collapse uncertainty and reliability criterion evaluation as per PBWD pre-standard (ASCE, 2019) under wind loads.....	112

List of Abbreviations

Δ_{\max}	maximum inelastic interstorey drift
ACMR	Adjusted Collapse Margin Ratio
ACMR _{10%}	acceptable value of the Adjusted Collapse Margin Ratio (ACMR)
A_g	gross cross-sectional area of an element
B	width of a building
B_x	ratio at level x to determine torsional sensitivity
C_a	shape factor
C_b	basic roof snow load factor
CBF(s)	Centrally Braced Frame(s)
C_e	the exposure factor
C_g	the gust effect factor
CMR	collapse margin ratio
C_p	the external pressure coefficient
CP	collapse prevention
C_r	factored compressive resistance of a member or component
CR	component reliability
C_s	slope factor
C_t	the topographic factor
C_u	probable compressive resistance of bracing members
C_u'	probable post-buckling compressive resistance of bracing members
C_w	wind exposure factor

D	the width of the building parallel to the wind direction
DGM(s)	design ground motion(s)
DI	damage index
DL	dead load
DM	damage measure
D_{nx}	plan dimension of the building at level x perpendicular to the direction of seismic loading being considered
E	elastic modulus of steel (200 000 MPa assumed)
EDP	engineering demand parameter
e_x	distance measured perpendicular to the direction of earthquake loading between center of mass and center of rigidity at the level being considered
F_a	site coefficient
FA(a)	floor acceleration(s)
$F_{i, x}$	lateral force applied to level x,i respectively
F_u	specified minimum tensile strength (MPa)
F_y	specified minimum yield stress, yield point or yield strength (MPa)
G	shear modulus for steel
g_p	the peak factor
H, h_n	total height of a building
h_i	the height above the base ($i = 0$) to level i
h_x	the height above the base ($i = 0$) to level x
IDA	Incremental Dynamic Analysis
I_E	earthquake importance factor of the structure
IM	intensity measure

IO	immediate occupancy
I_s	snow importance factor of the structure
ISD(s)	interstorey drift(s)
J	torsional constant
J_x	numerical reduction coefficient for overturning moment at level x
K_{gusset}	out-of-plane rotational stiffness of the gusset plate
KL	effective length
kl/r	slenderness ration
L_b	brace length
LFRS	Lateral Force Resisting System
LL	live load
LLRF	live load reduction factor
LS	life safety
m	fatigue ductility exponent
MCI	median collapse intensity
M_f	factored flexural moment
M_r	factored flexural moment resisting
M_v	higher mode factor
M_x	overturning moment at level x
N_f	number of cycles that causes failure
NRHA	nonlinear response history analysis
N_x	notional load at level x

OpenSees	the Open System for Earthquake Engineering Simulation
P	external pressure acting statically in a direction normal to the surface
PBD	performance-based design
PBSD	performance-based seismic design
PBSE	performance-based seismic engineering
PBWD	performance-based wind design
PGA	peak ground acceleration
PGV	peak ground velocity, in m/s
P_x	gravity load used in seismic load combination
q	reference velocity pressure
r	radius of gyration
R	a parameter that defines the shape of the unload curve
R_0	overstrength-related force modification factor
R_d	ductility-related force modification factor
RISD(s)	residual interstorey drift(s)
R_y	the overstrength factor
S	snow load
s	size reduction factor
S(T)	design spectral response acceleration
$S_a(T)$	5% damped spectral response acceleration
$\hat{S}CT$	median value of collapse level
SFRS	Seismic Force Resisting System(s)

SLS	serviceability limit state
S_r	1-in-50-year associated snow load
SSF	spectral shape factor
SSR	structural system reliability
t	thickness
T_a	fundamental lateral period of vibration of the building
t_g	thickness of the gusset plate
TPU	Tokyo Polytechnic University
T_u	probable tensile resistance of bracing members
T_x	floor torque at level x
U_C	median collapse wind speed
ULS	ultimate limit state
\bar{V}	reference wind speed at a height of 10 m
V_E	static lateral earthquake design force at the base of the structure
V_{Ed}	dynamic lateral earthquake design force at the base of the structure
$V_{elastic}$	elastic base shear calculated from the 5% damped response spectrum
V_H	mean wind speed at the top of the structure
w	web thickness
W_w	Whitmore width
β_{DR}	design requirements-related collapse uncertainty
β_{MDL}	modeling-related collapse uncertainty
B_{RTR}	record-to-record collapse uncertainty

β_{TD}	test data-related collapse uncertainty
β_{TOT}	total system collapse uncertainty
δ_{ave}	average displacement of the structure at level x
δ_{max}	maximum displacement of the structure at level x
δ_u	ultimate roof drift displacement corresponding to 80% of the total base shear capacity
$\delta_{y,effe}$	effective yield roof drift displacement
ε^*	effective strain depending on the unload/reload interval
ε_0	fatigue ductility coefficient
ε_i	strain amplitude
θ_x	stability factor at level x
λ	non-dimensional slenderness ratio for compression members
μ_T	period-based ductility of an index archetype model
ν	average fluctuation rate
ξ	damping ratio
ρ	air density
σ^*	effective stress depending on the unload/reload interval

1. CHAPTER 1. INTRODUCTION

1.1 General

Driven by the necessity to ensure the safety of the occupants in the aftermath of natural disasters, new advancements were incorporated in the building code and design standards. Thus, Performance-Based Seismic Engineering (PBSE) has made great advancements in terms of seismic hazard analysis, nonlinear dynamic analysis, and probabilistic and deterministic methods of damage quantification (Porter, 2003). Known also as Performance-Based Seismic Design (PBSD), this methodology, allows the quantification of structural reliability, defined as the probability of a structural system to remain functional despite the failure of any component. (Der Kiureghian, 2006).

Since 1990, the National Building Code of Canada (NBC) (NRC, 1990) and the associated design standards are based on the ductility concept and the seismic force resisting systems (SFRS) were designed to yield and dissipate energy through well-detailed members; therefore, to respond beyond the elastic limit. The main idea behind such philosophy is to take advantage of the structure's inherent overstrength and ductility in the events of strong earthquakes and to allow controlled damage of some members designed to behave as ductile fuses. The current NBC (NRC, 2015) uses explicitly the ductility-related force modification factor (R_d) and the overstrength-related force modification factor (R_o) to reflect the structures' ability to dissipate energy through the inelastic behavior. Moreover, the steel design standard CSA/S16 -14 employs the capacity

design principle to size the adjacent beam and column members of ductile fuses (braces) in the case of concentrically braced frames (CBF).

Prior to the 2005 edition of NBC (NRC, 2005), the seismic hazard was based on a return period of 500 years which is equivalent with 10% probability of exceedance in 50 years. However, in NBC 2005, this has changed with the adoption of 2% probability of exceedance in 50 years associated with 2475 years return period.

Although the Performance-Based framework was initially developed for the seismic assessment of new structures, recently, it was adapted in wind engineering in an effort to optimize structural performance and therefore economy under wind events. However, the complex nature of wind and the significant computational effort required to perform wind history simulations, delayed the developments of performance-based wind design methodologies. In response to the increasing interest in performance-based approaches for the wind design of buildings, the Structural Engineering Institute (SEI) of the American Society of Civil Engineers (ASCE) developed a pre-standard for Performance-Based Wind Design in 2019.

Meanwhile, wind design following the major international codes, and NBC in particular, has remained prescriptive to the Component Reliability (CR) in which it only considers the first significant yielding point in the wind design of buildings under ultimate limit state combinations. Regarding wind hazard, the annual probability of exceedance was reduced from 3.3% (30-year return period) in NBC editions prior to 2005, to 2% (50-year return period) thereafter. Wind design practice in Canada requires the building to respond elastically to the factored wind load, having a 10% in 50 years (500-year return period) wind hazard (NRC, 2015). The seismic design philosophy which is based on the ductile behavior of building's structure is not used when designing buildings to resist wind loads.

Current wind design does not explore nonlinearity beyond the design level, neither account for the inherent system overstrength. In fact, the actual intended building performance is not explicitly part of the wind design process (Griffis et al. 2012), resulting in an uneconomical building design or extensive repair cost for existing buildings. Design becomes more challenging in the case of structures sited in areas subject to both wind and earthquake, since the lateral force resisting elements should be proportioned to yield under seismic loads and dissipate energy through hysteresis, whereas should respond elastically under the factored wind load (Athanasίου et al., 2022).

Winds and earthquakes are mutually exclusive hazards, and they are neither concurrent nor successive; hence, neither triggers nor intensifies the other (Zaghi et al. 2016). A possible mode of hazard interaction is the aftershocks following the main shock of an earthquake or flying debris after a strong wind. However, a building that experiences earthquake damage will be more sensitive to wind during the repair time span. Other potential hazard interacting effects, for instance network and system disruption, or social consequences that could amplify the losses, are not considered herein. Insights for interacting hazards can be found in Petrini et al. (2020).

1.2 Objectives and Scope

This study focusses on the multihazard assessment of multi-storey steel buildings located in Montreal, QC, on rough terrain and Site class C. Both the plan and elevation of the studied buildings are regular. These buildings are laterally supported by steel concentrically braced frames (CBF) with X-split tension-compression braces. Under earthquake load, the preliminary design was based on the Equivalent Static Force procedure (ESFP) as per NBC (2015). The notional loads and the $P-\Delta$ effects were considered in the analysis while the accidental torsional effect was not

accounted for herein. The capacity design approach was applied to proportion the members of the lateral forces resisting system. Because these buildings are dynamic sensitive under wind load, the dynamic method was employed to calculate the wind-induced shear force.

The main objectives are:

- Assess the seismic and wind response of the Lateral Force Resisting System (LFRS) buildings at the design level and beyond under a set of spectrum-compatible ground motions and wind realizations generated from wind tunnel data.
- Construct the IDA curves and fragility curves under wind and earthquake and identify the failure mechanisms of multi-storey Concentrically Braced Frames (CBF) buildings, respectively.
- Verify the collapse safety under seismic load following the FEMA P695 (2009) procedure ($ACMR \geq ACMR_{10\%}$) and check the wind reliability criterion following the ASCE PBWD prestandard (2019). The reliability criterion defined in the PBWD prestandard (ASCE, 2019) requires that the wind design velocity ($V_{1/500}$) to be greater than the wind velocity at which there is a 0.01% conditional probability of failure ($V_{0.01\%}$).

1.3 Methodology

To achieve the main objectives of this research, the following methodology is used:

- Two tall steel office buildings are analyzed under wind and earthquake load in order to assess their response to multihazard events. These buildings have the same floor plan, different heights (12-storey and 16-storey) and different seismic force resisting systems such as LD-CBF and MD-CBF. Herein, the 12-storey building is designed and analyzed considering the MD-CBF as seismic force resisting systems, while the 16-storey building

is braced by the LD-CBFs. All buildings are designed to satisfy the ultimate and serviceability limit state criteria according to NBC (2015) provisions and the Steel Design Standard S16-14 under seismic and wind loads. As per the NBC, LD-CBF and MD-CBF are the limited ductility concentrically braced frame and moderately ductile concentrically braced frame, respectively.

- A numerical two-dimensional model was developed using the OpenSees framework. The model is capable of replicating brace fracture caused by the low-cycle fatigue. The computational algorithm is the same as used by Uriz (2005). The non-simulated failure mode of CBF columns was also monitored by triggering the bending moment and axial force time-histories series.
- A reliable performance assessment of studied buildings is carried out through nonlinear dynamic analysis. For this purpose, a set of seven artificial ground motions, compatible with the design spectrum were selected from the Engineering Seismology Toolbox database (<http://www.seismotoolbox.ca>). To analyze the wind effect on high-rise buildings, wind time-history series were generated using aerodynamic data from the Tokyo Polytechnic University (TPU) database.
- To provide insights in the progressive development of failure mechanism of MD-CBFs or LD-CBFs, from yielding to collapse, seismic and wind Incremental Dynamic Analyses (IDA) were performed independently for each individual ground motion and wind sequence.
- The performance assessment under earthquake and wind loads was conducted according to FEMA P69 5(2009) procedure and ASCE PBWD (2019) pre-standard methodology. Hence, using data from IDA curves, the fragility curves were performed in order to assess

the collapse margin safety. Then, the wind reliability criterion was checked following the ASCE PBWD pre-standard. Finally, the effect of multihazard assessment is discussed.

1.4 Thesis Organization

Details on the work done in this research are documented in six chapters. A Brief summary for each chapter is highlighted below:

- Chapter 1 serves as the introduction providing a general review on the evolution of the Performance-Based Seismic Design (PBSD) over the last decades and highlighting the need to revise the traditional design philosophy of tall buildings under wind hazard. The objectives of the research and the methodology followed herein are also outlined in this chapter.
- Chapter 2 includes the literature review. It discusses the design requirements for tall buildings, under seismic and wind loads, according to NBC (2015) and S16-2014 standard. It also familiarizes the reader with the performance-based seismic and wind engineering as well as the performance-based multihazard design. The numerical modeling concepts adapted to simulate the response of the CBFs under seismic and wind loads using the OpenSees framework are described. Guidelines for the implementation of Incremental Dynamic Analysis (IDA) and construction of fragility curves are also provided herein.
- Chapter 3 introduces two prototype buildings, selected as the case study, located in Montreal, QC. The structural system of the 12-storey MD-CBF and 16-storey LD-CBFs buildings were designed to withstand the seismic load. Then, the design ensured that the LFRSs respond in the elastic range under the wind loads associated to design level.

- Chapter 4 elaborates on the detailed finite element computational models of the case study. The analysis setup for the nonlinear time history, including the selecting and scaling the ground motions and wind realizations, derived from aerodynamic wind tunnel test data, are presented herein.
- Chapter 5 presents the results obtained from the nonlinear time history analysis of the finite element models under the set of the seven artificial ground motions and the five wind realizations provided in Chapter 4. Information collected from the Incremental Dynamic Analysis (IDA) was used to predict the failure mechanism and build the fragility curves of the prototypes considering seismic and wind loads. The assessment of the collapse safety criteria was based on FEMA P695 (2009) procedure, whereas the wind reliability criterion was checked following the ASCE PBWD (2019) pre-standard guidelines.
- Chapter 6 presents the conclusions and suggests useful future work in the same field.

2. CHAPTER 2. LITERATURE REVIEW

In this chapter, a literature review on the performance-based seismic and wind design, as well as the performance-based multihazard design is reported. General review on the seismic and wind load design in accordance with *NBC (2015)* and *CSA S16-14* is discussed. In addition, detailed concepts of modeling the Concentrically Braced Frames (*CBFs*) using the OpenSees framework are described. Finally, guidelines for performance evaluation and collapse assessment including Incremental Dynamic Analysis (*IDA*) and fragility analysis are also reviewed, as well as the framework presented in FEMA P695 (2009) procedure and PBWE pre-standard (2019).

2.1 General

While seismic codes have evolved to the point that allows to integrate Structural System Reliability (SSR) or collapse safety into the seismic analysis (Aswegan et al. 2017), wind design has remained prescriptive to the Component Reliability (CR). Der Kiureghian (2006) defined the Structural System Reliability (SSR) as a probability of a structural system to remain functional despite the failure of any structural component. Hence, the wind design of tall buildings is associated with the ultimate limit state and the design is deemed satisfactory if no yielding of a structural member occurs.

The complex nature of wind loads, and the significant computational effort that is required to perform wind history response simulations, delayed the developments in wind design and assessment of existing buildings.

Wind design practice in Canada requires the design of the building to respond elastically to the 10% in 50 years (500-year return period) wind hazard (NRC, 2015), while ASCE (2017) refers to a 700-year return period for Risk Category II buildings (e.g., residential and office buildings). In

either case, wind design in North America is code-prescriptive and overly conservative; in fact, the actual intended building performance assessment is not explicitly part of the design process (Griffis et al. 2012) which leads to an uneconomical design of lateral force resisting system (LFRS) of a building or extensive repair cost for existing LFRS of buildings.

2.2 Earthquake Load Design According to NBC 2015

2.2.1 Equivalent Static Force Procedure

In accordance with NBC (2015), there are two procedures to analyze a building under earthquake actions: The Equivalent Static Force Procedure (ESFP) and the Dynamic Analysis Procedure by means of modal response spectrum method (elastic) and nonlinear time-history integration method.

The former can be used for the structures where: i) $I_E F_a S_a(0.2) < 0.35$, ii) regular structures that are less than 60 m in height with a fundamental lateral period $T_a < 2$ s in each of the two orthogonal directions and iii) structures with structural irregularity of type 1,2,3,4,5,6 or 8 but not more than 20 m in height and have a fundamental lateral period $T_a < 0.5$ s in each of the two orthogonal directions.

As per NBC (2015), the equivalent static force corresponds to a 2% probability of exceedance in 50-years (2475 years return period).

Table 2.1 shows the acceleration response spectra ordinates for 0.2, 0.5, 1.0, 2.0, 5.0 and 10 s for site Class C in Montreal in addition to the horizontal Peak Ground Acceleration (PGA) and the horizontal Peak Ground Velocity (PGV).

Table 2.1. Seismic Data for Site Class C, Montreal.

Seismic Data for Montreal							
S (0.2)	S (0.5)	S (1.0)	S (2.0)	S (5.0)	S (10.0)	PGA	PGV
0.595	0.311	0.148	0.068	0.018	0.0062	0.379	0.255

The minimum lateral earthquake force V is calculated as:

$$V_E = \frac{S(T_a)M_v I_E W}{R_d R_0} \quad 2.1$$

where $S(T_a)$ is the 5% damped spectral response acceleration for the fundamental lateral period T_a , M_v is a factor to account for higher mode effect on base shear, I_E is the importance factor for earthquake design, W is the seismic weight taken as 100% of the dead load (D) plus 25% of the design snow load (SL), R_d is the ductility-related force modification factor and R_0 is the overstrength-related force modification factor, respectively.

For buildings with Seismic Force Resisting System (SFRS) with $R_d \geq 1.5$ and located on sites other than Class F, the maximum base shear is the maximum value provided by Eq. (2.2); hence, the value is bounded to V_{max} .

$$V_{max} = Max \left\{ \begin{array}{l} \frac{2S(0.2)M_v I_E W}{3 R_d R_0} \\ \frac{S(0.5)M_v I_E W}{R_d R_0} \end{array} \right\} \quad 2.2$$

Meanwhile, if the building fundamental period is larger than 2 s, the minimum base shear given in Eq. (2.3) is used in design.

$$V_{E,min} = \frac{S(2)M_v I_E W}{R_d R_0} \quad 2.3$$

Since the concentrically braced frames (CBF) are used as the Lateral Force Resisting System (LFRS), the fundamental lateral period (T_a) is determined using the following equation:

$$T_a = 0.025 \cdot h_n \quad 2.4$$

where h_n is the building height in meters.

The lateral seismic force V is distributed using the inverted triangle pattern over the height of the building using the following equation:

$$F_x = (V_E - F_t)W_x h_x / \left(\sum_{i=1}^n W_i h_i \right) \quad 2.5$$

where

h_x is the reference height and F_t is a concentrated force at the top of the building. When $T_a \geq 0.7$ s, F_t is calculated using the following equation:

$$F_t = 0.07T_a V_E \leq 0.25V_E \quad 2.6$$

If $T_a < 0.7$ s, consider $F_t = 0$.

2.2.2 P-Δ Effect and Notional loads

The laterally deformed building under lateral forces shall also sustain the gravity loads. This reduces the structure's capacity to resist these lateral loads causing an increment in the lateral displacement and moments. Hence, the second-order effects that are due to the relative transitional displacement shall be determined from a second-order analysis. This effect is known as P-delta effect and can increase the displacement and drives the building into the inelastic range.

In general, the CSA/S16-14 standard follows a simplified procedure to take P-delta effect into consideration by increasing earthquake-induced forces, shear, overturning and torsional moments at each storey by an amplification factor $U_2 = (1 + \theta_x)$. Herein, θ_x is the stability factor at the considered level, calculated using the following equation:

$$\theta_x = \frac{\sum_i^n C_f}{\sum_i^n V_f} \cdot \frac{R_d \Delta_f}{h_s} \quad 2.7$$

where

$\sum_{I=x}^n V_f$ = design seismic shear force at level x, which is the sum of the design lateral seismic forces acting at and above level x.

$\sum_{i=x}^n C_f$ = factored axial force associated with the gravity component of earthquake load combination (DL + 0.5LL + 0.25SL + E) at and above level x.

Δ_f = inelastic interstorey drift at level x.

h_s = interstorey height

R_d = ductility – related force modification factor.

It is worth noting that when the stability factor θ_x is less than 0.1 or the amplification factor $U_2 < 1.1$ then, the P-delta effects is neglected. Moreover, when U_2 is greater than 1.4, the structure is instable and should be redesigned.

In addition to the P-delta effect, the CSA/S16-14 standard requires to account for notional lateral loads that is added to the lateral loads. The notional lateral loads are computed in both orthogonal directions independently by considering a fraction of the gravity load as follow:

$$N_x = 0.005 \sum C_{f,x} \quad 2.8$$

where N_x is the notional load at level x and $\sum C_f$ was defined above.

2.2.3 Capacity Design Principle

In accordance with the National Building Code of Canada (NBC, 2015), earthquakes with a magnitude as large as 7 can occur in Montreal. Prior to the 2005 edition of the National Building

Code of Canada, the definition of the seismic hazard was based on a 10% probability of exceedance in 50-years equivalent to 475 years return period. However, this has changed in the last editions of NBC with the adoption of 2% probability of exceedance in 50 years associated with a return period of 2475 year.

Seismic design following the current NBC (2015) edition accounts for the explicit overstrength factor (R_0) and ductility-related force modification factor (R_d) when calculating the shear forces used in addition to shear caused by P-delta and notional load effects to design braces of CBFs. These braces are designed and detailed as ductile fuses while the adjacent CBF members are designed to resist brace member forces according to capacity design principle. Thus, the beams, columns, and connections of CBFs do not dissipate the input energy and shall remain elastic by ensuring adequate strength to resist the maximum loads transferred from the fuses. This approach has led to improved performance under increased ground motions.

In the capacity design of concentrically braced frames (CBFs), the probable tensile resistance T_u , the probable compressive resistance C_u and the probable post-buckling compressive resistance C_u' are computed using the following equations:

$$T_u = A_g R_y F_y \quad 2.9$$

$$C_u = \min \left\{ \begin{array}{l} A_g R_y F_y \text{ and} \\ 1.2 A_g R_y F_y (1 + \lambda^{2n})^{-1/n} \end{array} \right\} \quad 2.10$$

$$C_u' = \min \left\{ \begin{array}{l} 0.2 A_g R_y F_y \text{ and} \\ A_g R_y F_y (1 + \lambda^{2n})^{-1/n} \end{array} \right\} \quad 2.11$$

For W-shape sections, $R_y = 1.1$, while the probable yield stress is $R_y F_y$. For hollow structural sections (HSS), the probable yield strength shall not be less than 460 MPa as stipulated in CSA/S16-14.

It is worth mentioning that the member compression resistance, C_r , is calculated as $\Phi A_g F_y (1 + \lambda^{2n})^{-1/n}$, where $\Phi = 0.9$, A_g is the area of brace, F_y is the steel yield strength, λ is the slenderness and $n = 1.34$.

2.2.4 Dynamic Analysis Procedure

For irregular buildings, or buildings with $B > 1.7$ and $I_E F_a S_a(0.2) \geq 0.35$, the static force procedure is no longer valid, and the Dynamic Analysis is required.

The Dynamic Analysis can be carried out in the linear or non-linear domain. The linear analysis can be performed using the 5% damped linear modal response spectrum method. The non-linear numerical integration time history method can be applied using the design-spectrum compatible ground motion histories. The structural model should comply with the requirement of NBC (2015) and CSA/S16-14 standard.

The dynamic base shear V_{Ed} , is obtained by multiplying the elastic design base shear $V_{elastic}$ by the importance factor I_E and dividing it by the ductility-related force modification factor (R_d) and the overstrength-related force modification factor (R_o). The dynamic (design) base shear (V_{Ed}) should not be less than 80% of the lateral earthquake design force (V_E) obtained from the equivalent static force procedure. However, such reduction rule does not apply to irregular buildings where V_{Ed} should be taken equal to V_E .

2.3 Wind Load Design According to NBC 2015

2.3.1 General

Regarding the wind hazard, the annual probability of exceedance was reduced from 3.3% (30-year return period) in NBC editions prior to 2005, to become 2% (50-year return period) thereafter. The

seismic design philosophy, which is based on the ductile behavior of the structure is not used when designing buildings to resist wind loads. Instead, a factor of 1.4 provided in the load combination case in NBC is used in wind load design considering that the hourly mean wind speed is based on a return period of 50 years. Thus, the factored wind load corresponds to a return period of about 500 years and is used to design the LFRS of buildings using the traditional wind design. In the traditional wind design prescriptive, the first significant yielding point is considered a limit state, beyond which, the building is not expected to respond. This can result in an uneconomical design or extensive repair cost for existing buildings since the procedure does not explore what happens in case of allowing a controlled nonlinear response.

2.3.2 Wind Load Calculation

In accordance with NBC (2015), buildings are classified as not dynamically sensitive, dynamically sensitive, or very dynamically sensitive. On this basis, three design procedures are recommended: i) the static procedure, ii) the dynamic procedure and iii) the wind tunnel procedure.

The flowchart below, illustrates the complete procedure to determine the wind load acting on a building depending on its configurations and the lowest natural frequency.

In Fig. 2.1, H is the building height, f_n is the frequency, and w is the effective width considering all wind directions of the building calculated as follow:

$$w = \frac{\sum h_i w_i}{\sum h_i} \quad 2.12$$

where the summations are over the height of the building for a given wind direction, h_i is the height above grade to height h_i . Thus, according to Fig. 2.1, the Wind Tunnel Procedure is an acceptable compliance method for all cases.

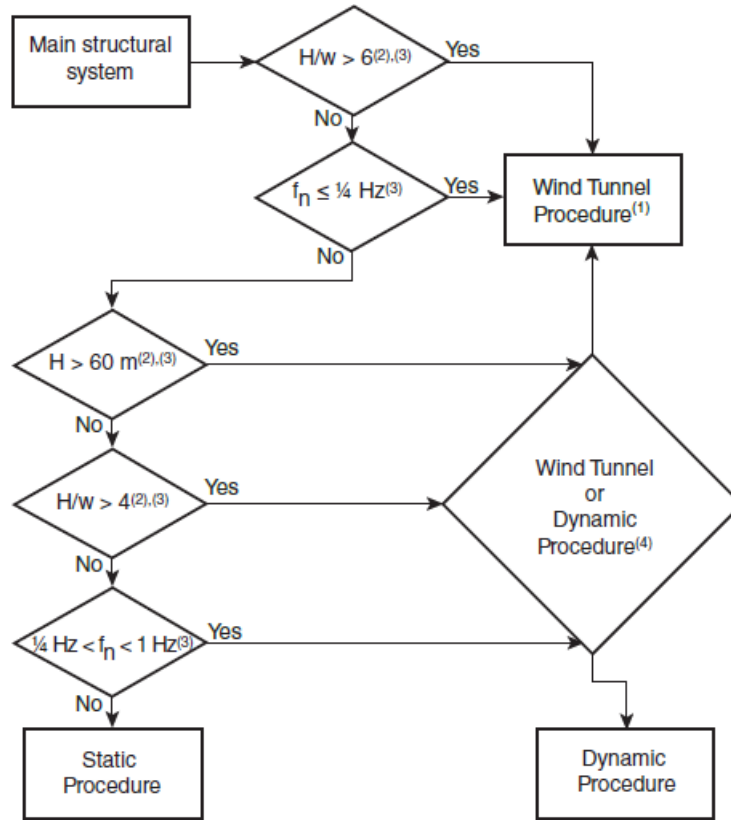


Fig. 2.1. Decision tree for selecting appropriate design method for the main structural system in accordance with NBC (2015).

2.3.3 Static Procedure

The static procedure is used to calculate the lateral wind load on buildings that are classified as not dynamically sensitive.

The following equation is used to calculate the external static pressure acting on part or all of a surface due to wind:

$$p = I_W q C_e C_t C_g C_p \quad 2.13$$

where

p is the external pressure acting statically in a direction normal to the surface, I_W is the importance factor for wind, C_e, C_t, C_g, C_p are the exposure, topographic, gust effect and external pressure factors, respectively. Herein, q is the reference velocity pressure, which is calculated from the annual maxima of 60 minutes moving average wind speed in open flat terrain at height of 10 m and has an annual probability of 1 in 50 years.

The exposure factor C_e is based on the reference height, h , and calculated as follows:

$$C_e = \left(\frac{h}{10}\right)^{0.2} \geq 0.9 \quad \text{for open terrain} \quad 2.14$$

$$C_e = 0.7\left(\frac{h}{12}\right)^{0.3} \geq 0.7 \quad \text{for rough terrain} \quad 2.15$$

The gust effect factor is taken $C_g = 2.0$ for the building as a whole and main structural members.

The external pressure coefficients C_p , is computed as a function of H/D , where H is the building height and D is the building's dimension parallel to the applied wind force.

a) On the windward face:

$$C_p = 0.6 \text{ for } \frac{H}{D} < 0.25 \quad 2.16$$

$$C_p = 0.27\left(\frac{H}{D} + 2\right) \text{ for } 0.25 \leq \frac{H}{D} < 1.0 \quad 2.17$$

$$C_p = 0.8 \text{ for } H/D \geq 1.0 \quad 2.18$$

b) On the leeward face:

$$C_p = -0.3 \text{ for } \frac{H}{D} < 0.25 \quad 2.19$$

$$C_p = -0.27\left(\frac{H}{D} + 0.88\right) \text{ for } 0.25 \leq \frac{H}{D} < 1.0 \quad 2.20$$

$$C_p = 0.5 \text{ for } H/D \geq 1.0 \quad 2.21$$

c) On the walls parallel to the wind, $C_p = -0.7$

2.3.4 Dynamic Procedure

For the Dynamic Procedure, the external static pressure is always evaluated using Eq. (2.13); however, the exposure factor C_e and gust effect factor C_g are now calculated from the following equations:

a) For buildings in open terrain, the exposure factor C_e is calculated as:

$$0.5 \leq C_e = 0.5 \left(\frac{h}{12.7} \right)^{0.5} \leq 2.5 \quad 2.22$$

b) For buildings in rough terrain, the exposure factor C_e is equal to:

$$1.0 \leq C_e = \left(\frac{h}{10} \right)^{0.28} \leq 2.5 \quad 2.23$$

c) The gust effect factor C_g shall be taken as:

$$C_g = 1 + g_p \frac{\sigma}{\mu} \quad 2.24$$

where

$$g_p = \sqrt{2 \ln(\gamma T)} + \frac{0.577}{\sqrt{2 \ln(\gamma T)}} \quad 2.25$$

$$\frac{\sigma}{\mu} = \sqrt{\frac{K}{C_{eH}} \left(B + \frac{sF}{\beta} \right)} \quad 2.26$$

$$\gamma = f_{nD} \sqrt{\frac{sF}{sF + \beta B}} \quad 2.27$$

$$s = \frac{\pi}{3} \left[\frac{1}{1 + \frac{8f_n H}{3V_H}} \right] \left[\frac{1}{1 + \frac{10f_n W}{V_H}} \right] \quad 2.28$$

Herein, g_p is the peak factor and γ is the average fluctuation rate; $T=3600$ s; $K=0.8$ for open terrain and 0.1 for rough terrain; C_{eH} is the exposure factor evaluated at reference height $h = H$. Then, B is the background turbulence factor; s is the size reduction factor and F is the gust energy ratio calculated as:

$$F = \frac{(x_0)^2}{(1 + x_0^2)^{4/3}} \quad 2.29$$

where: $x_0 = 1220 f_n / V_H$ 2.30

and f_n is the lowest natural frequency, while V_H is the mean wind speed at the top of the structure calculated as per Eq. (2.31).

$$V_H = \bar{V} \sqrt{C_{eH}} \quad 2.31$$

Moreover, β is the damping ratio equal to 0.01 for steel structures; w is the effective width of windward face of the building calculated as per Eq. (**Error! Reference source not found.**) and V is reference wind speed at a height of 10 m as per Eq. below:

$$\bar{V} = \sqrt{\frac{2 \cdot I_q \cdot q}{\rho}} C_{eH} \quad 2.32$$

where $\rho = 1.2929 \text{ kg/m}^3$ is the air density.

2.3.5 Wind Tunnel Procedure

Wind Tunnel Procedure on scale models can be conducted as an alternative to the Static and Dynamic Procedures to determine wind loads on buildings as specified in NBC 2015 and more in detail in ASCE/SEI 49 (2012), “Wind Tunnel Testing for Buildings and Other Structures”. It is

especially recommended for buildings that may be subjected to buffeting or channeling effects caused by upwind obstructions, vortex shedding, or to aerodynamic instability.

This procedure consists of tests that take into account the dynamic properties of a building as its natural frequency. Thus, this procedure is required for buildings whose lowest natural frequency f_n is $\leq \frac{1}{4}$ Hz or whose height is more than 6 times their minimum effective width as depicted in Fig. 2.1.

2.4 The Open System for Earthquake Engineering Simulation

The Open System for Earthquake Engineering Simulation (OpenSees) is an open-source in which its framework has been developed by the Pacific Earthquake Engineering Research Center (PEER) in 2004 (PEER, 2015), as a tool to simulate the nonlinear response of structures/ building structures subjected to seismic loads. It provides the users around the world with a wide range of elements and material models supported by different algorithms to simulate the nonlinear response of systems. OpenSees is a programmable environment written in C++ and a very efficient tool to perform the nonlinear dynamic analysis.

2.4.1 Concentrically Braced Frames model developed in OpenSees.

Concentrically Braced Frames (CBFs) are commonly used as a Lateral Force Resisting System (LFRS) to dissipate the input energy through the inelastic response of braces that buckle in compression and yield in tension, while sustaining large deformations until failure of braces occur. Meanwhile, the adjacent columns and beams should remain in the elastic range. This highly nonlinear behavior of the braces requires an accurate analytical model to simulate the inelastic response over different response stages.

During earthquakes, it is unlikely for a component of LFRS to be subjected to constant amplitude cycling (Uriz & Mahin, 2008). For that reason, a rainflow cycle counting method can be applied to monitor the exceedance of the fatigue life for each individual uniaxial fiber in the cross section. The rainflow counting technique introduced by Matsuishi and Endo (1968) is the first accepted method used to extract closed loading reversals or cycles. However, this approach requires a computational effort. As such, Uriz (2005) proposed a modified procedure for modeling the effect of low-cycle fatigue by considering only the four most recent peaks of strain reversals at any given time and implemented it in the OpenSees. The overall damage index is calculated using the following equation, known as Miner's rule, where the overall damage, caused by the low-cycle fatigue, is calculated by considering the linear accumulation of damage at each cycle (ε_i).

$$DI = \sum \frac{n_i(\varepsilon_i)}{N_{fi}(\varepsilon_i)} \quad 2.33$$

In Eq. (2.33), DI is the accumulative damage index for each amplitude of cycling, n_i is number of cycles at that amplitude cycles, N_{fi} is the number of cycles necessary to cause failure. The value of DI varies between 0 when there is no damage in the material and 1 at failure.

The relationship between the strain amplitude (ε_i) and the number of cycles that causes failure is defined using the empirical Coffin-Manson equation:

$$\varepsilon_i = \varepsilon_0(N_f)^m \quad 2.34$$

In this equation, ε_0 is the fatigue ductility coefficient and (m) is the fatigue ductility exponent. Hence, at any point, if the damage index $DI > 1$, the corresponding stress of the fiber in the cross section fall to zero.

Following the linear accumulation damage procedure and considering the experimental results obtained by Yang (2005) after testing HSS braces to failure, Uriz (2005) found that using $\varepsilon_0 =$

0.095 and $m = -0.5$ match the test results. However, later studies showed that these constant parameters are not adequate when using other HSS brace sections. Considering 158 HSS brace sections, Lignos and Karamanci (2013) developed a predictive equation for modeling the inelastic cycle buckling and fracture for HSS based on a power-law fitting model with a 95% confidence bound:

$$\varepsilon_0 = 0.291 \left(\frac{kl}{r}\right)^{-0.484} \left(\frac{w}{t}\right)^{-0.613} \left(\frac{E}{F_y}\right)^{0.3} \quad 2.35$$

where: w/t is the width-to-thickness ratio of the HSS cross section. This equation was derived using slenderness ratio (kl/r) varying between 27 and 85.

By using $m = -0.3$ in the Eq. (2.35) as a constant value, a good match was reported between the value of the predicted and the calibrated ε_0 for the rectangular HSS sections with an approximate mean value of 0.064.

Hsiao et al. (2013) developed a regression analysis based on the results of 44 specimens to predict the limiting maximum strain range and proposed the following equation:

$$Max. \varepsilon_{range,pred.} = 0.1435 \left(\frac{kl}{r}\right)^{-0.3} \left(\frac{w}{t}\right)^{-0.4} \left(\frac{E}{F_y}\right)^{0.2} \quad 2.36$$

However, at the upper floors of multi-storey buildings, the slenderness ratio of the HSS braces might be bigger than 85.

Tirca and Chen (2014) proposed the following empirical equation for modeling the nonlinear response of the square HSS sections, with slenderness ratio between 50 and 150, and predicting the failure strain as:

$$\varepsilon_0 = 0.006 \left(\frac{kl}{r}\right)^{0.859} \left(\frac{w}{t}\right)^{-0.6} \left(\frac{E}{F_y}\right)^{0.1} \quad 2.37$$

Herein, the fatigue ductility exponent that was used is $m = -0.5$.

The formulation of the fiber-based brace model was discussed by Uriz (2005), Agüero et al. (2006), Hsiao et al. (2013), Lignos and Karamanci (2013), Tirca and Chen (2014) and others. Hsiao et al. (2013) concluded that using 16 force-based nonlinear beam-column elements with distributed plasticity and fiber based cross section discretization is sufficient to capture the HSS brace fracture. Each element contains three Gauss-Lobatto integration points to represent the curvature distribution along the element. The Giuffre-Menegotto-Pinto steel material (*Steel02* in OpenSees) with isotropic strain hardening is used to assign the nonlinear behavior of the elements.

$$\sigma^* = b\varepsilon^* + \frac{(1 - b)\varepsilon^*}{(1 + \varepsilon^{*R})^{1/R}} \quad 2.38$$

Herein, σ^* and ε^* are the effective stress and strain depending on the unload/reload interval, respectively, b is the ratio of the final to initial tangent stiffness, R is a parameter that defines the shape of the unload curve.

The HSS cross section is defined by using the Fiber Discretization Technique with rounded fibers at the corners to detect any potential yielding or buckling. It generates a total of 240 quadrilateral shaped patches within the HSS cross section, 40 fibers for each edge segment and 20 fibers for corner segments as illustrated in Fig. 2.2.

The behavior of the HSS brace to frame gusset plate connection is simulated by using two nonlinear rotational springs and one linear torsional spring, defined in the Zero-length element that connects the end of the brace to a rigid link representing part of column's section and that of gusset plate, as shown in Fig. 2.3. The out-of-plane rotational stiffness of the gusset plate, K_{gusset} , assigned to rotational spring, is defined using the following expression (Hsiao et al 2012):

$$K_{gusset} = \frac{E}{L_{ave}} \left(\frac{W_w t_g^3}{12} \right) \quad 2.39$$

In Eq. (**Error! Reference source not found.**), E is the Young's modulus, W_w is the Whitmore width defined by a 30° projection angle, L_{ave} is the average of L_1 , L_2 and L_3 as shown in Fig. 2.3, and t_g is the thickness of the gusset plate (Hsiao et al 2012).

The linear torsional stiffness is calculated using the equation below:

$$K_t = \frac{GJ}{L_{ave}} \quad 2.40$$

where G is the shear modulus of the steel material and J is the torsional constant.

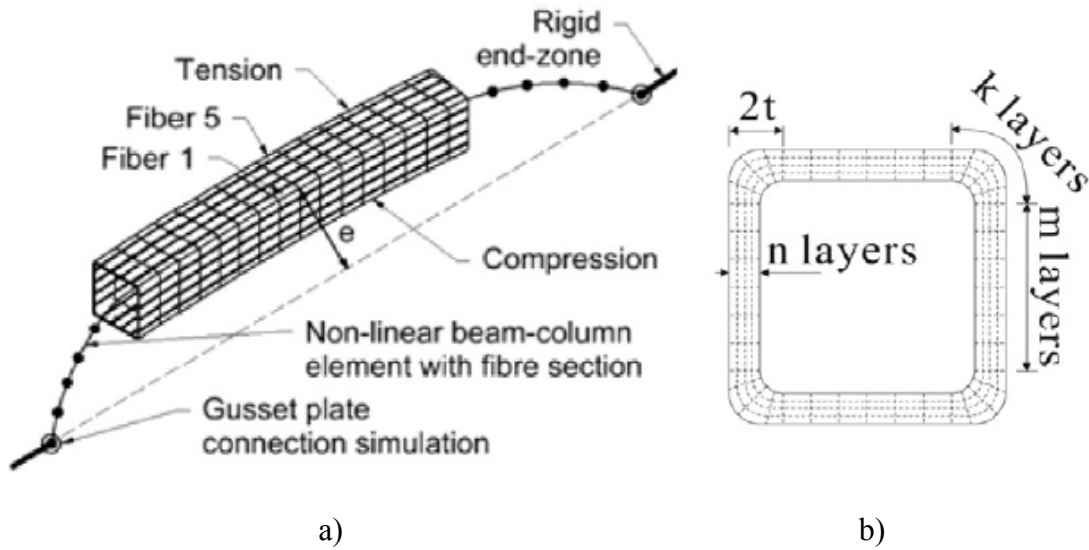


Fig. 2.2. Modeling the HSS brace: a) numerical model of the HSS brace with end connection, b) discretization technique applied to HSS brace cross section, (Tirca et al 2015).

leading to a false inelastic mechanism. An out-of-straightness imperfection of $L_b/500$ was found to give matching results with the tested specimens.

2.5 Performance-Based Design

The primary intention stipulated in code and design standard provisions was to avoid seismic-induced collapse on buildings and to preserve lives when subjected to relatively extreme seismic events. Loma Prieta (1989) and Northridge (1994) earthquakes proved the reliability of the current code provisions in high seismic zones to avoid collapse and to protect the occupants. However, the economic loss was devastating and demands raised to adopt more effective practices to limit the damage in future events. Thus, the first Performance-Based Design (PBD) procedure is presented in FEMA 356 (2000) and was elaborated by Fajfar et al. (2004) and other researchers.

2.5.1 Performance-Based Seismic Design (PBSD)

Performance-Based Seismic Design (PBSD) has allowed structural engineers to better understand the performance of buildings that are subjected to a specific level of seismic demand and removed any limit of what engineers can accomplish. It provides the design team with the freedom to design new facilities of any complexity that meet specific performance objectives.

Starting with FEMA 365 (2000), four discrete structural performance levels and two intermediate structural ranges associated with different seismic hazard levels, applied to both structural and non-structural components, were proposed in the aim of assessing the building performance. These performance levels are identified as Operational, Immediate Occupancy (IO), Life Safety (LS) and Collapse Prevention (CP), as schematically shown in Fig. 2.5.

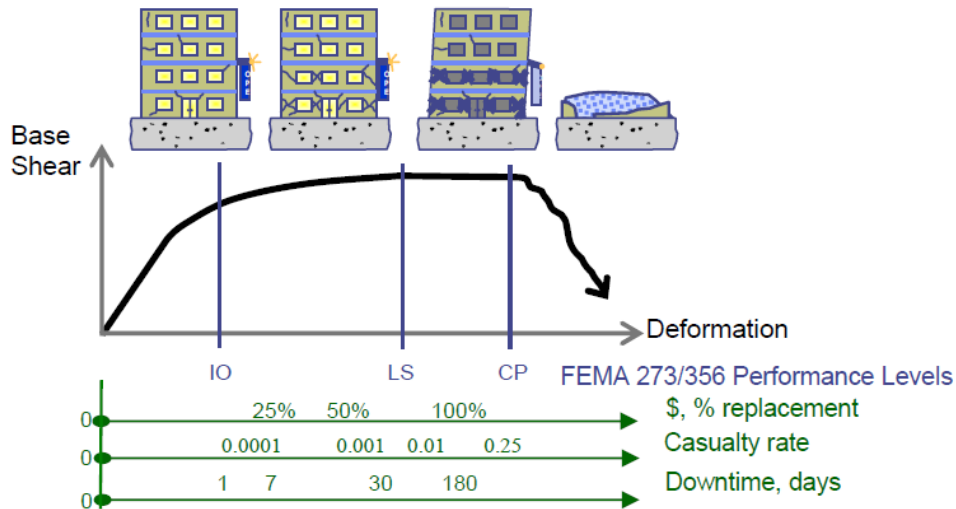


Fig. 2.5. Representation of the four Performance Levels (Fajfar et al. 2004).

Extensive analytical research, experimentations, and observations of seismic responses of buildings promoted the integration of earthquake engineering knowledge to develop earthquake-resistant structures. Knowing the hazards, the Performance-Based Seismic Design (PBSD) uses a strength hierarchy to proportion members of seismic force resistance systems (SFERS) able to reach the targeted performance goals and objectives (Cornell and Krawinkler, 2000).

Deformation-controlled (ductile) elements, such as braces of CBFs dissipate the input energy through yielding, whereas force-controlled elements (beams and columns supporting gravity loads) remain elastic.

Building design procedure is code-prescriptive and its main intention is to meet the life-safety performance level when a design-level earthquake occurs. However, it is not possible to determine if the building can achieve other performance levels under the same event. Besides, the designed building could suffer from a significant damage so the repair cost is too expensive, and demolition may be the only option.

The Federal Emergency Management Agency (FEMA) contracted the Applied Technology Council (ATC) in 2006, and initiated Phase 1 development of a seismic performance assessment methodology. The work was completed in 2012 with the publication of FEMA P-85, *Seismic Performance Assessment of Buildings*, including *Volume 1–Methodology* and *Volume 2–Implementation Guide*, in addition to various supporting electronic material and technical references. FEMA P-58 was revamped and presented in the 2018 edition.

FEMA P-58 methodology is probabilistic in nature which describes the seismic performance as the probable consequence, in terms of human and economic loss due to earthquake shaking. It also includes the development of basic building information, response quantities, fragilities, and consequence data used as inputs to the methodology. It enables three major analytical steps to predict statically the seismic performance of a structure;

1. Seismic hazard analysis in terms of intensity measures (IM).
2. Seismic demand analysis given in terms of demand parameters or response quantities.
3. Fragility analysis associated with the damage under different limit state.

Since most casualties occurs as result of partial or total collapse, it is necessary for engineers to define a collapse fragility function in which it determines the probability of collapse as a function of the intensity measure.

In this methodology, the assessment of a structure can be expanded further to loss analysis under different hazard events, which is considered of great interest to stakeholders and decision-makers.

The FEMA P-58 performance assessment methodology is illustrated in Fig. 2.6. Thus, the performance is expressed in terms of direct economic loss, repair time/ repair cost, and casualties.

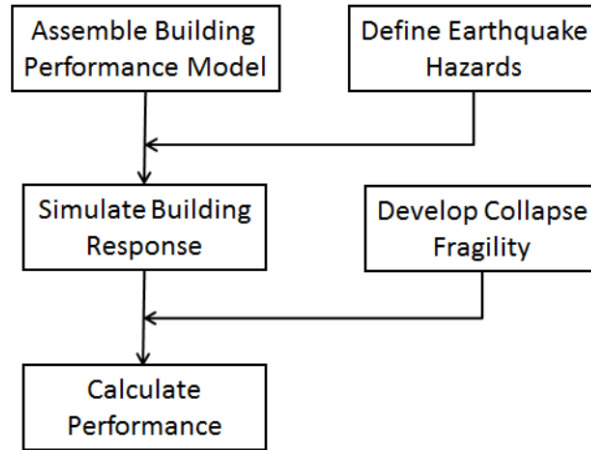


Fig. 2.6. Flowchart of the performance assessment methodology (FEMA P-85, 2018).

2.5.2 Incremental Dynamic Analysis

To follow the methodology presented in Fig. 2.6, the collapse fragility is based on the results obtained from the application of Incremental Dynamic Analysis (IDA). The concept of IDA was firstly introduced by Bertero (1977) and refined by Vamvatsikos and Cornell (2002) who defined the IDA analysis as a valuable tool of seismic engineering. According to their study, a building may exhibit a different response, such as softening or hardening and weaving behavior, under a different ground motion as illustrated in Fig. 2.7. Thus, a single-record IDA curve may not be enough to predict the response of a structure under the events that could hit the building in the future and it is highly recommended to consider a suite of ground motions in order to capture the response in full scale. In Fig. 2.7, the intensity measure (IM) is represented by the spectral acceleration of the first mode $S_a(T_1, 5\%)$ for earthquake. Hence, $S_a(T_1, 5\%)$ is incrementally scaled to increasing values until collapse occurs. Each point of the IDA curve corresponds to a nonlinear dynamic analysis which represents the relation between the Intensity Measure (IM) (on the vertical axis) and the Damage Measure (DM) (on the horizontal axis).

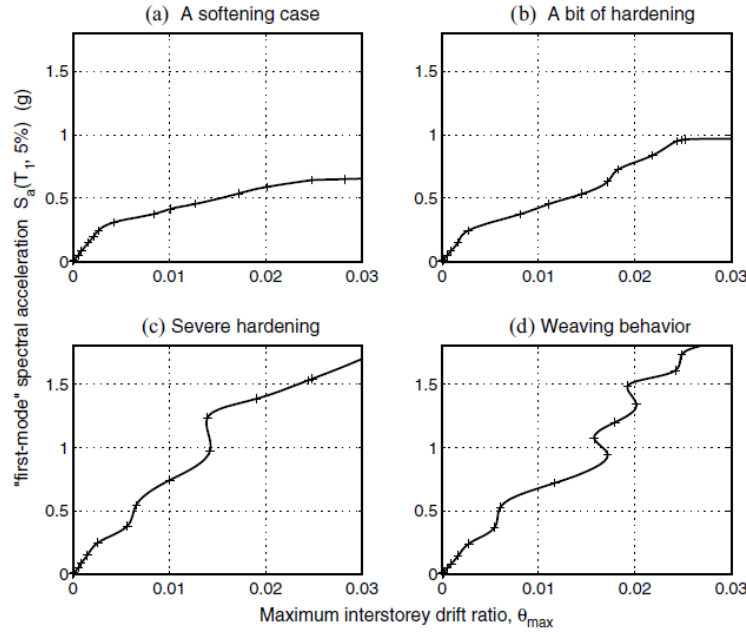


Fig. 2.7. IDA curves of a 5-storey steel braced frame ($T_1 = 1.8$ s) under 4 different ground motions that input various responses: a) softening response, b) a bit of hardening response, c) severe hardening and d) weaving behaviour (Vamvatsikos and Cornell 2002).

Hence, the Damage Measure is a perceptible quantity of the corresponding nonlinear dynamic analysis which is expressed in function of the selected Engineering Demand Parameter (EDP) that can be the peak interstorey drift among floors, the peak residual interstorey drift among floors or the peak floor acceleration (on the horizontal axis). In general, the IM is plotted on the vertical axis and the associated EDP on the horizontal axis. The vertical component of the ground motions is not considered in analysis, since it does not have a significant impact on the building seismic response (FEMA P695, 2009).

Fig. 2.8 shows the differences in the seismic response of the same structural model under a suite of seismic ground motions. Taking into consideration the inherent randomness in the response, a probabilistic characterization should be used to predict the building response. Thus, the IDA method representing the relation between the IM and DM is no longer deterministic due to the

wild range of behavior (Vamvatsikos and Cornell 2002). A typical way to predict the collapse is by considering the median collapse intensity curve when half (50th percentile value) of the ground motions leads to the collapse of the building. To summarize the building's seismic response, a set of IDA curves representing the 50%, 16% and 84% fractile values are computed and illustrated in Fig. 2.8.b.

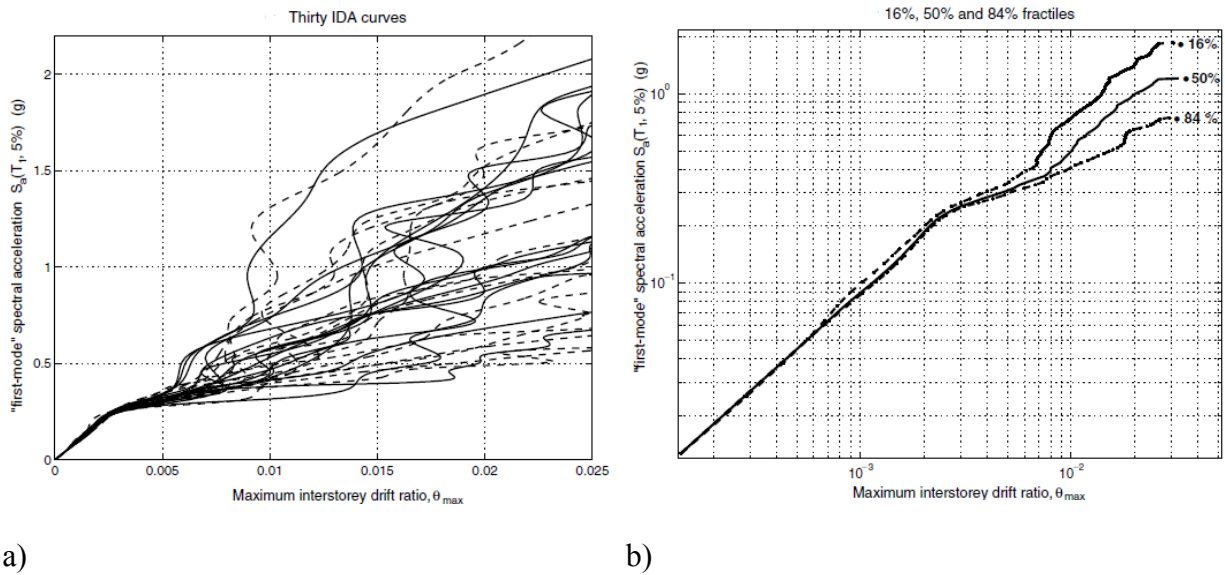


Fig. 2.8. IDA response of a 5-storey braced frame building: a) IDA curves under 30 ground motions and b) the 16%, 50% and 84% fractile curves in log-log scale (Vamvatsikos and Cornell 2002).

The IDA approach can be similarly apply to analyse the wind response of a building. In this case the Intensity Measure can be the U_{ref} for wind, where U_{ref} is the wind velocity at 10 m and the engineering demand parameter (EDP) can be the interstorey drift or the floor acceleration.

2.5.3 Fragility Analysis and Collapse Margin Ratio (CMR)

The concept of fragility analysis is used to predict the probability of reaching a failure or a certain damage state under certain demand. The collapse fragility curve, expressed mathematically by the

cumulative distribution function (CDF), relates probabilistically the Intensity Measure (IM) and the associated probability of collapse. Hence, a direct method represented by the IDA is used to gather data that are necessary to build the fragility curve.

Fig. 2.9.b illustrates an example of a cumulative distribution plot using a cumulative lognormal distribution of spectral acceleration at the first mode period through the collapse data collected from the results of a set of IDA curves. These curves presented in Fig. 2.9.a (FEMA P695, 2009) are plotted as a function of the intensity measure (IM) represented by the spectral intensity of the ground motion, and the peak interstorey drift among floors as an EDP.

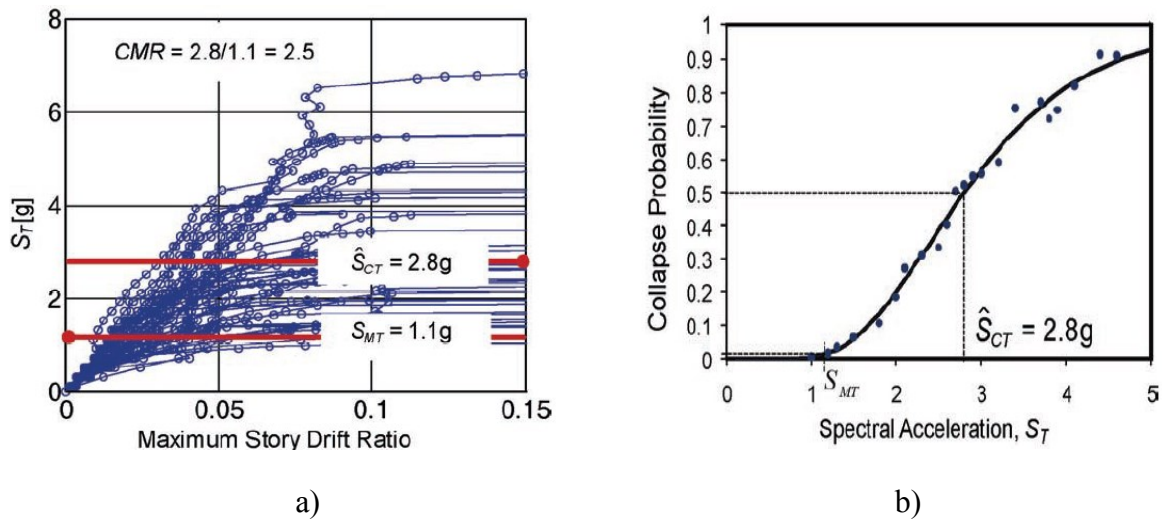


Fig. 2.9. Building response under a suite of GMs: a) IDA curves and b) collapse fragility curve using a lognormal cumulative distribution function, (FEMA P695, 2009).

Two parameters are used to define the lognormal collapse fragility, the median collapse intensity (\hat{S}_{CT}), and the standard deviation (β_{TOT}). The latter describes the total collapse uncertainty given by the following equation (FEMA P659, 2009):

$$\beta_{TOT} = \sqrt{\beta^2_{RTR} + \beta^2_{DR} + \beta^2_{TD} + \beta^2_{MDL}} \quad 2.41$$

where:

- β_{TOT} = total system collapse uncertainty but not more than 0.5
- β_{RTR} = record-to-record collapse uncertainty (0.20 – 0.40)
- β_{DR} = design requirements-related collapse uncertainty (0.10 – 0.50)
- β_{TD} = test data-related collapse uncertainty (0.10 – 0.50)
- β_{MDL} = modeling-related collapse uncertainty (0.10 – 0.50)

The shape of the collapse fragility curve can be affected by the total uncertainty in which it leads to flatten the curve for bigger values. However, the median collapse intensity (\hat{S}_{CT}), is still the same as illustrated in Fig. 2.10. Hence, the dashed curve represents the collapse fragility curve with a total system collapse uncertainty $\beta_{TOT} = 0.4$, while the solid line reflects a fragility curve associated to $\beta_{TOT} = 0.65$.

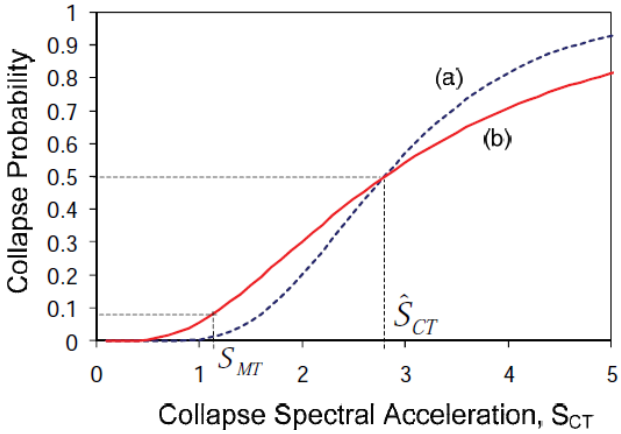


Fig. 2.10. Variation of collapse fragility curve as a function of total uncertainty $\beta_{TOT} = 0.4; 0.65$

For conventional framed structures, a simplified two-dimensional model can be used to calculate the median collapse intensity \hat{S}_{CT} for all the archetype buildings. Studies have demonstrated that there are differences between the two and the three-dimensional analysis. However, the three-dimensional analysis shows a conservative bias in which it results in the median collapse intensity to be on average 20% less than the value resulting from the two-dimensional analysis. Thus, an

adjustment should be made on the collapse margin ratio (CMR) calculated based on the median collapse intensity \hat{S}_{CT} (FEMA P695, 2009). The Collapse Margin Ratio (CMR) is defined as the ratio between the median collapse intensity \hat{S}_{CT} and the design spectral acceleration intensity obtained from the response spectrum at the design level $S_a(T_1, 5\%)$ for earthquake hazard 2% probability of exceedance in 50 years.

$$CMR = \hat{S}_{CT}/S_a(T_1) \quad 2.42$$

The frequency content (spectral shape) of the ground motion record set can also have a significant impact on the collapse margin ratio (CMR) (Baker and Cornell 2006). Spectral shape effects may be quantified through the definition of the simplified spectral shape factor (SSF). The SSF adjusts the collapse margin ratio (CMR) to obtain the adjusted collapse margin ratio (ACMR):

$$ACMR = SSF * CMR \quad 2.43$$

Hence, (SSF) is a function of the first-mode period (T_1), the period-base ductility (μ_T) and the applicable Seismic Design Category (FEMA P695, 2009). Accordingly, the period-based ductility (μ_T) represents the ratio between the ultimate roof drift displacement corresponding to 80% of the total base shear capacity, δ_u , and the effective yield roof drift displacement, $\delta_{y,eff}$ that is calculated using a nonlinear static pushover analysis as shown in Fig. 2.11.

$$\mu_T = \frac{\delta_u}{\delta_{y,eff}} \quad 2.44$$

As per FEMA P695, the spectral shape factor (SSF) results from a table.

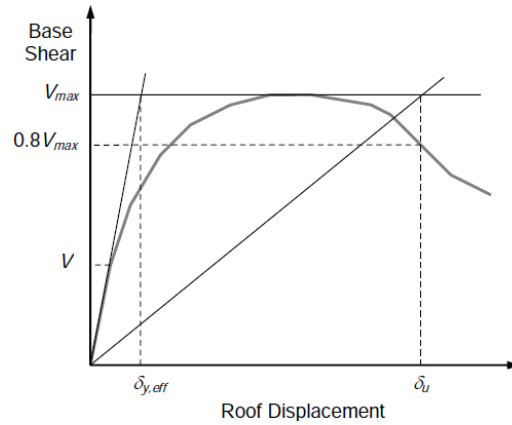


Fig. 2.11. Idealized nonlinear static pushover curve (FEMA P695, 2009).

To pass the collapse safety criteria, the following equation should be verified:

$$ACMR \geq ACMR_{10\%} \quad 2.45$$

where $ACMR_{10\%}$ is the acceptable value of $ACMR$ corresponding to an appropriate total uncertainty value β_{TOT} and 10% probability of collapse. The $ACMR_{10\%}$ results from tables provided in FEMA P695 (2009).

Tirca et al. (2015) evaluated the collapse safety of 8-storey and 12-storey CBF buildings located in Vancouver, B.C. Canada that were subjected to crustal and subduction ground motion sets. It was concluded that the 12-storey CBF building subjected to subduction ground motions was not able to pass the collapse safety criteria.

2.5.4 Performance-Based Wind Design (PBWD)

In response to the increasing interest in using performance-based approaches for the design of buildings, the Structural Engineering Institute (SEI) of the American Society of Civil Engineers (ASCE) developed a pre-standard for Performance-Based Wind Design in 2019. Meanwhile, researchers used the concept of fragility to develop design frameworks and quantify the failure at

discrete limit states probabilistically (Ellingwood et al., 2004; Van de Lindt and Dao, 2009; Li and Ellingwood, 2009; Ciampoli et al., 2011).

Ellingwood et al. (2004) developed a methodology based on the fragility analysis to assess the response of light-frame wood construction exposed to extreme windstorms. The initial applications of this methodology appeared to be promising in predicting the performance of the building. However, before being applied to improve building codes, it must be validated as a tool to predict the losses from postulated natural hazards.

Van de Lindt and Dao (2009) presented the concept of performance-based wind engineering for wood-frame buildings by applying a fragility-based approach to form different performance expectations. They developed fragilities for four different performance descriptors by examining the idea of linking the performance expectation level back to a peak 3-s gust using a comprehensive finite-element model.

Ciampoli et al. (2011) expanded the approach proposed by the Pacific Earthquake Engineering Research Center (PEER) for Performance-Based Earthquake Engineering to the case of Performance-Based Wind Engineering (PBWE). By applying the general framework of the approach to an example case, they concluded that PBWE is feasible and can be applied. However, more improvements should be carried further on the probabilistic description of the parameters of the wind field at the site and the phenomena that represent the interaction between the wind actions and the structure to make the PBWE more reliable.

Judd (2018) used a set of wind load time histories derived from the wind tunnel test database in Tokyo Polytechnic University (TPU) to predict the resilience of a 10-storey steel-frame office building in windstorms. By implementing the FEMA P-58 procedure (FEMA 2012a) and using the corresponding software for performance-based seismic engineering, the nonlinear finite

element model predicts that the building could resist the service-level windstorms with a mild impact and the average floor acceleration was below the recommended value on High-rise buildings and Urban Habitat (Judd, 2018). However, rare or extreme events would cause a significant damage.

Wind engineering shows a great potential interest for further developments of Performance-Based Design (Petrini et al., 2009). Recently, many studies in wind engineering have been carried out to adopt the consolidated concept of Performance-Based Seismic Design (PBSD) into Performance-Based Wind Design (PBWD) by expanding the approach which was proposed for (PBSD) by the Pacific Earthquake Engineering Research Center (Porter 2003), and released the first PBWD pre-standard (ASCE, 2019).

In a study conducted by Griffis et al. (2012), a framework for performance-based wind design was proposed and depicted in Fig. 2.12. They conducted a nonlinear dynamic analysis using wind tunnel data. Their motivation was to explore a more economical design by pushing the structure beyond the first significant yielding point. They illustrated that by allowing controlled inelastic behavior, most economic buildings can be designed.

Mohammadi et al. (2019) developed a 3D nonlinear finite-element model using OpenSees (PEER, 2015) to assess the dynamic wind performance of an existing 47-storey steel building with perimeter steel moment-resisting frames and interior steel gravity columns, located in Houston, Texas. The building was designed in early 1971 for limited wind design criteria and survived hurricane Alicia 1983, which is considered a near-design wind event by current ASCE 7 standards, without any significant structural damage. The building response to different wind hazard levels was evaluated through incremental dynamic analysis (IDA). More details can be found in Mohammadi (2016). The study concluded that the under-designed building possesses adequate

nonlinear capacity to resist a relatively high wind speed and fulfill the performance levels. However, the extreme flexibility of the building led to a compromise in the serviceability performance related to the interstorey drifts and floor accelerations. Hence, allowing some limited inelastic actions in the lateral force resisting system (LFRS) while providing an acceptable serviceability performance could improve the cost-benefit relationship.

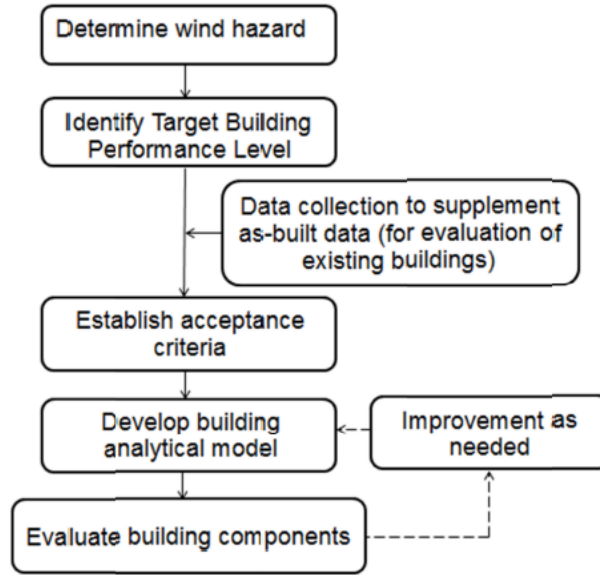


Fig. 2.12. Performance Based Wind Engineering Framework in accordance with Griffis et al (2012).

To achieve a cost-effective wind design of structures, several researchers combined PBWD procedures with optimization algorithms (Spence and Kareem, 2014; Chuang and Spence 2017; Suksuwan and Spence, 2018; Athanasiou et al., 2020; Kleingesinds et al., 2020).

A critical review of the current state of PBWD development and wind design practice in Canada can be found in Bazabeh et al. (2020). In Bazabeh et al. (2020) it was mentioned that the design methods provided in the Canadian code (NBC, 2015) stipulate that the building reaches the ultimate limit state when the first yielding of a member of LFRS occurs, but the collapse behavior

of building structure under the effect of extreme windstorms is not described. Also, design methods are prescriptive and ignore the inherent overstrength and plasticity of structural systems. This can augment the cost of tall buildings due to the uncertainties in design and more precisely in the exhibition of an excessively large margin of safety. Furthermore, while the current Performance-Based Wind formulations, which are derived from the earthquake engineering methodology, are the key to establish the roadmap for a complete Performance-Based Wind Design, the inherent differences between earthquake and wind loads especially the frequency content and load duration can accumulate and trigger brittle collapse in tall buildings. Hence, more study should be conducting.

When the pre-standard for PBWD of tall buildings (ASCE 2019) was released by the American Society of Civil Engineers (ASCE), it covered the fundamental aspect of the PBWD including the risk category definition, performance objectives and wind demand characterization. It also allowed specific elements or components of the structural system, such as braces, to respond inelastically to dissipate energy under wind load with a mean recurrence interval (MRI) of 700-years for Risk Category II (residential and office buildings) as per ASCE (2017). However, the design approach in the pre-standard does not explicitly define force-reduction factor (R) which is considered as an important factor in achieving an economical design through (PBWD).

El Damatty and Elezaby (2018) were among the first to propose a load reduction factor (R) that could be applied in wind design. This reduction factor was applied only to the fluctuation components of the time history, which was then modified in accordance, to take into consideration the larger flexibility that the building acquires due to the reduction in demand. They applied time history data, derived from wind tunnel testing of a rigid model of the case building, on a three-dimensional finite element model as shown in Fig. 2.13. Then, a nonlinear time history analysis

was conducted. By assuming a reduction factor of $R = 2$, they could reduce the thickness of the shear walls which were subjected to reduced flexural moment. However, no significant increase in the resulting natural period is indicated. Moreover, the pushover analysis conducted on the building with the reduced members showed a value of the ductility demand between 1.17 and 1.3, and the target performance is mainly in the Immediate Occupancy (IO) level.



Fig. 2.13. Wind tunnel test for a tall building in a compound (El Damatty and Elezaby, 2018).

Because of the difficulty in estimating the post-yield stiffness of the conventional structure in the early stage of the design, Jeong et al. (2021) followed the assumption of El Damatty and Elezaby (2018) and considered the reduction factor (R_w) for only the resonant component; then, expanded it to involve more values of the reduction factor $R_w = 1, 2$ and 3 . They used a time history of wind loads generated from power spectral density (PSD) functions to conduct a performance-based wind design for a high-rise building. The lateral force resisting system was selected as RC core walls and coupling beams in addition to the frame system. By performing nonlinear static analysis (pushover), the inelastic behavior was concentrated in the coupling beams in where the collapse

first occurred. However, when designing the building to resist the applied wind load in the elastic range ($R_W = 1$), the corresponding shear force is increased resulting in a reduction of ductility capacity. In conclusions, buildings that are designed with a reduction factor of $R_W = 2$ and 3, satisfy both Immediate Occupancy (IO) performance objective and drift limit in ASCE (2019). The load-displacement curve is shown in Fig. 2.14.

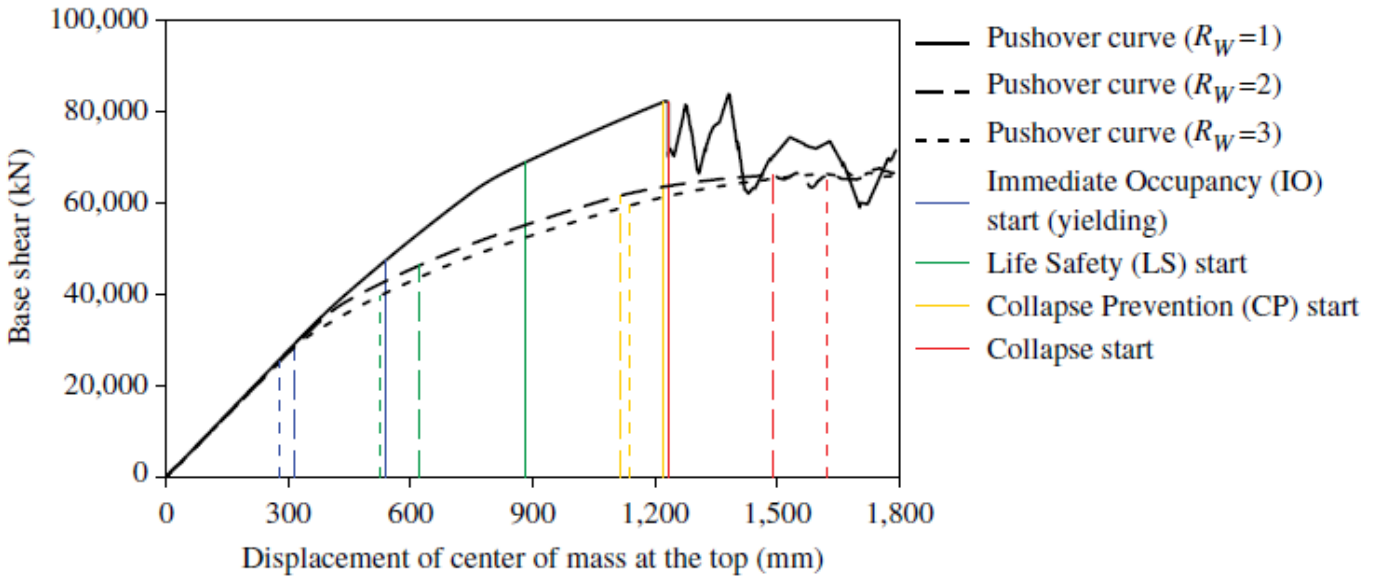


Fig. 2.14. Load-displacement curves and seismic performances. (Jeong et al. 2021).

The need to propose an R_w factor to design the LFRS under wind loads was also discussed by Bazabeh et al. (2020). They have also proposed a performance-based design framework that is shown in Fig. 2.15.

It is expected that the upcoming editions of building codes will prescribe structural systems capable of exhibiting controlled inelasticity when resisting wind loads.

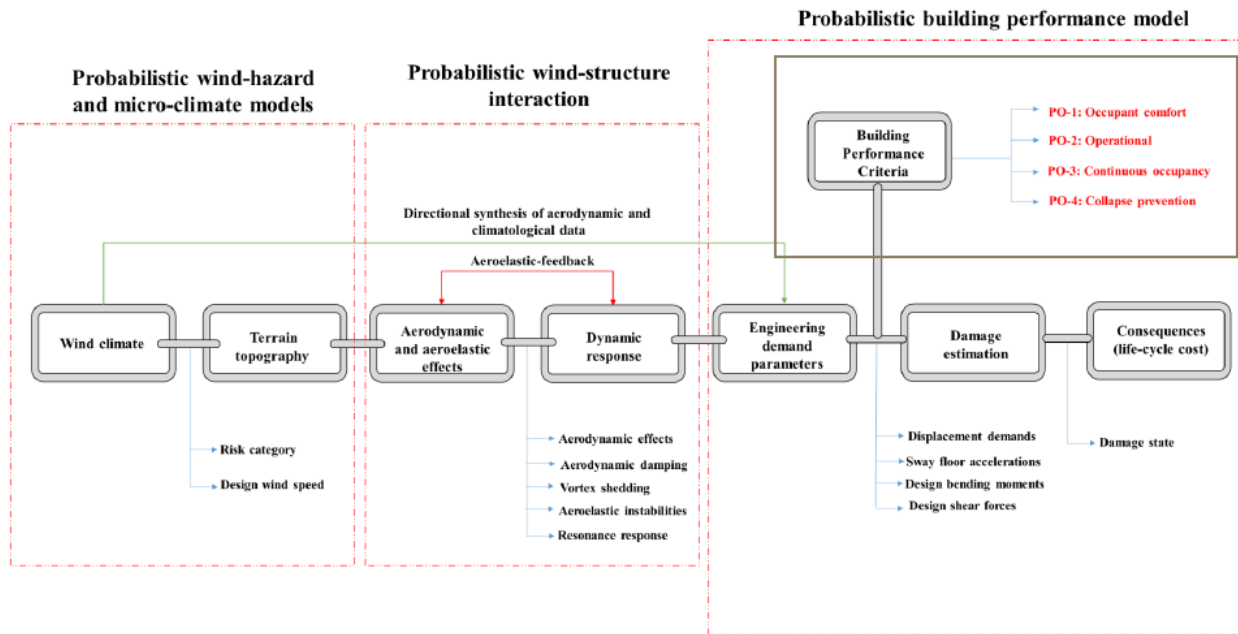


Fig. 2.15. PBWE Framework in accordance with Bezabeh et al. (2020).

2.5.5 Previous Studies on Performance-Based Multihazard Design

Regarding the multihazard design approach, an optimal design of a system does not require uniform reliability against different hazards (Wen and Kang, 2001). Meanwhile, Wen and Kang (2001) were among the first to estimate the expected life-cycle cost of engineering systems under wind and earthquake excitations. They concluded that the optimal hazard intensity used in design depends on the building lifetime due to the longer hazard exposure time. However, this intensity depends to a great extent on the hazard with large uncertainty and the consequence of failure which can be the most important factor in design.

Aswegan et al. (2017) mentioned that although the dominant hazard controls the design of structural members, the less intense hazard may contribute significantly to the overall damage and life-cycle cost. According to their study, in tall buildings where elastic wind demand controls the

design of the Lateral Force Resisting System (LFRS), using larger buckling-restrained braces (BRB) in outriggers, it produces a stiffer building with higher seismic demands which is critical for seismic performance. By considering the collapse prevention for wind demand and permitting controlled inelastic response under extreme wind loads, they could reduce the size of the BRBs in outriggers, which have higher capacity than required for seismic design objectives. Their conclusion was critical for seismic performance leading to a better performance of buildings under both wind and seismic hazards.

Building codes assume implicitly that in case of buildings in seismic regions, which are also exposed to high wind demand that may occur anywhere, the risk of exceedance of specified limit state is identical to the inherent risk assumed in the provisions for a single hazard (Duthinh and Simiu, 2010). However, this assumption is unwarranted and the notional risk of exceedance of limit states can be twice bigger than those in the areas where only one hazard is dominating.

Mahmoud and Cheng (2017) showed, by using the closed-form equations proposed by Kang and Wen (2000), that the optimal design is dependent on the natural frequency of the structure and the probability of exceedance for both hazards in which it would not be possible in case of evaluating the seismic load or wind load separately.

A multihazard assessment framework, under hurricane and earthquake hazards, was presented by Li and Ellingwood (2009). They evaluated the impact of multihazards and the effectiveness of mitigation strategies on residual drift of studied buildings by comparing the probability of various damage levels with the design-basis events. The hazard return period was set as a common control variable. Following their assumptions, they inferred that the probability of moderate-to-severe damage under design-basis events, when adopting enhanced construction standards, could be

reduced more considerably than when taking on the probability of only one minor damage as illustrated by fragility curves in Fig. 2.16.

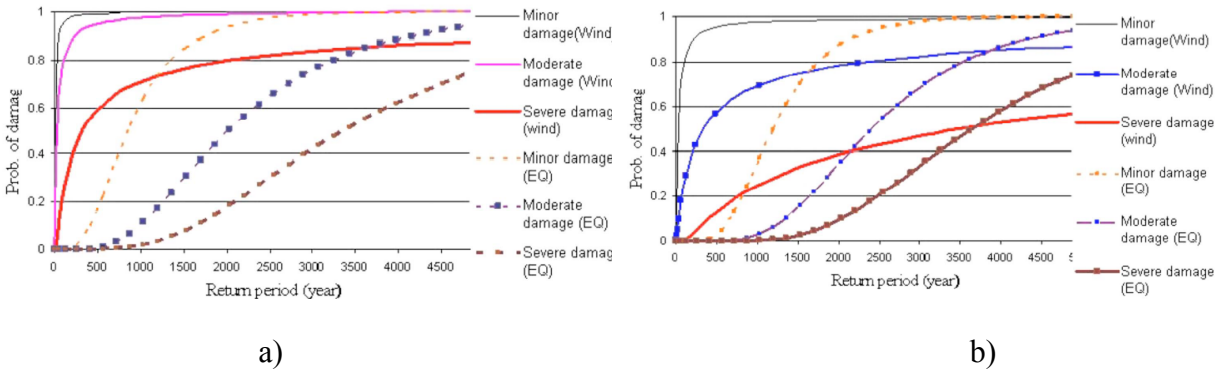


Fig. 2.16. Probability of hurricane and earthquake damage in Charleston, USA: a) minimum hazard-resistance construction practice, b) enhanced hazard-resistance construction practice, (Li et al., 2009).

Nikellis et al. (2019) performed extensive nonlinear wind and earthquake analyses using a 2D numerical model developed in OpenSees. They considered several buildings to identify whether the risk associated with the probability of collapse due to increasing wind excitation, beyond ASCE Standard 7, would result in cost-effective investment. It is also true that neglecting one hazard (worst case scenario approach) results in large errors to the predicted life-cycle losses.

More information on multihazard life-cycle cost assessment for tall buildings can be found in (Venanzi et al., 2018; Kleingesinds et al., 2021; Kleingesinds et al., 2021).

3. CHAPTER 3. SEISMIC AND WIND DESIGN OF CONCENTRICALLY BRACED FRAME BUILDINGS

Two multi-storey CBF buildings, located in Montreal, Quebec, were considered in this study. Concentrically Braced Frames (CBFs) were chosen as the Lateral Force Resisting System (LFRS) to withstand the seismic and wind loads, while the gravity columns and beams are designed to carry the vertical loads. Each building was analyzed and designed in accordance with the National Building Code of Canada (NBC 2015) under seismic and wind loads, as well as the CSA/S16-14 standard. To emphasize the difference between both types of loading, earthquake and wind loads were compared at each floor level before the building was designed for the governing load.

3.1 Case Study

The case study comprises 12-storey and 16-storey tall buildings with office occupancy located in Montreal (rough terrain) on Site class C (very dense soil). The building's plan and elevation are regular and shown in Fig. 3.1 and Fig. 3.2, respectively. These buildings are laterally braced by four concentrically braced frames (CBF) in each orthogonal direction. Thus, CBFs 1-4 span along the short direction of the building (N-S) and CBFs 5-8 span in the long direction (E-W). The design was conducted according with the provisions of NBC (2015) and CSA/S16-14 steel design standard. The matrix of building studied is as follows:

- 12-storey building braced by Moderately Ductile CBFs (MD-CBF), $R_d = 3.0$ and $R_o = 1.3$;
- 16-storey building braced by Limited Ductility CBFs (LD-CBF), $R_d = 2.0$ and $R_o = 1.3$.

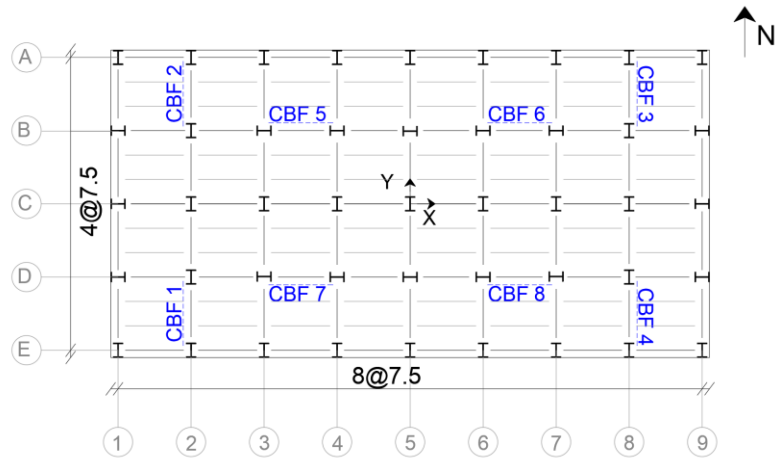


Fig. 3.1. Building plan and CBFs distribution for the 12-storey and 16-storey buildings. All dimensions are in meter.

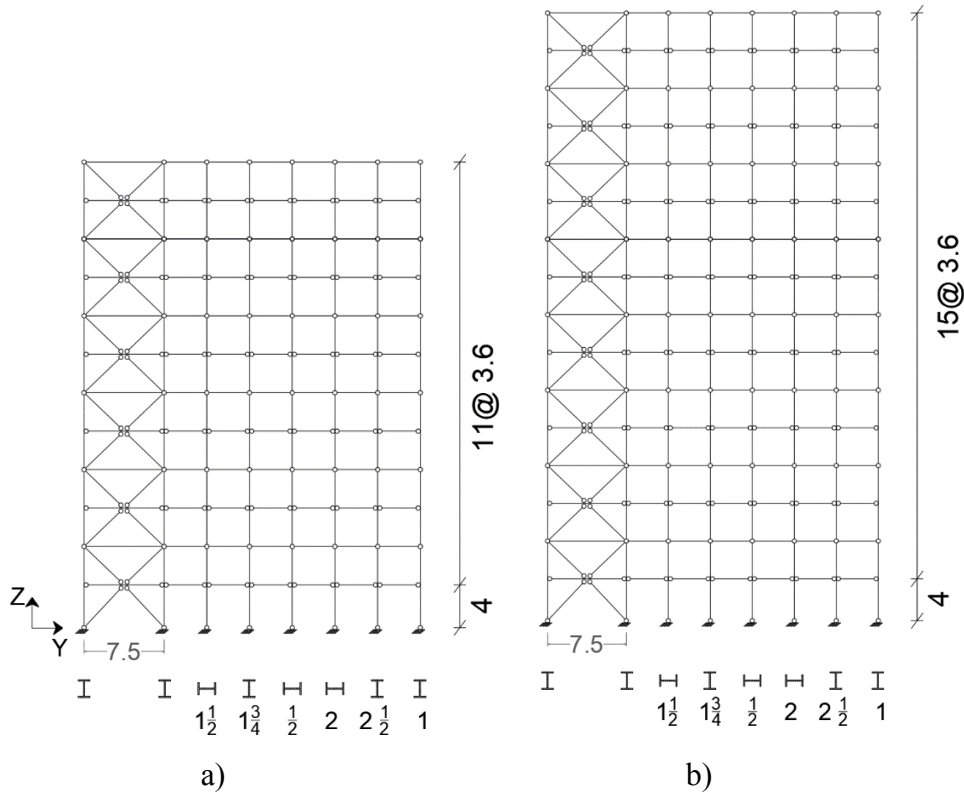


Fig. 3.2. 2-D elevations of buildings with CBF-1 acting in the N-S direction carrying $\frac{1}{4}$ of the load with the participating gravity columns: a) 12-storey; b) 16-storey. Dimensions are in meter.

In both cases, X-split bracing configuration systems with tension-compression members were considered. The beam-to-column connections, as well as, the braces-to-beam connections were assumed to be pinned. Columns are continuous over each 2 stories and pinned at the base.

The dead load (DL) is 3.3 kPa at the roof and 4.0 kPa at the typical floor levels. From calculation, the snow load is 2.48 kPa and the live load (LL) is 2.4 kPa, while 1.5 kPa is considered for cladding. The torsional effect was neglected in the analysis, while the notional loads and the $P-\Delta$ effects were considered.

The CBFs locations are identical in both case studies, are shown in Fig. 3.1. For all the buildings, there are 4 CBFs placed in each orthogonal direction in a symmetric way to avoid the torsional effect; each CBF supports $\frac{1}{4}$ of the building area. The numerical model associated with $\frac{1}{4}$ of the building is illustrated in Fig. 3.2. The typical span is 7.5 m, the floor area is 60.5 m x 30.5 m = 1845.25 m², the typical storey height is 3.6 m and that of the ground floor is 4.0 m. The height of the 12-storey and 16-storey buildings are 43.6 and 58.0 m, respectively.

3.1.1 Building Design

All buildings comprise two systems to withstand the applied loads:

- i. the gravity system including gravity columns and beams.
- ii. the lateral force resisting system (LFRS).

Each system carries the combined vertical loads such as the dead load (DL), the live load (LL) and the snow load on the roof (S) and transfer them to the foundation. The LFRS withstands the lateral forces, such as seismic load (E) and wind load (W) as well.

For design, the NBC (2015) requires two principal criteria to be satisfied:

- i. the ultimate limit state (ULS) concerning the strength of the structure members.

- ii. the serviceability limit state (SLS) to ensure the safety and comfort of people.

3.1.1.1 Design for gravity loads

The critical load combinations considered in the design of the gravity system are:

1. $1.4 DL$
2. $1.25 DL + 1.5 LL + 1.0 SL$
3. $1.25 DL + 1.0 LL + 1.5 SL$

The self-weight of the structural elements and the weight of the partition walls were included in the load combination cases.

The snow load on the roof was calculated in accordance with (NBC, 2015) as follows:

$$S = I_s [S_s (C_b C_w C_s C_a) + S_r] \quad 3.1$$

where I_s is the importance factor for snow load, S_s is 1-in-50 years ground snow load, C_b is the basic roof snow load factor, C_w is the wind exposure factor, C_s is the slope factor, C_a is the shape factor, S_r is 1-in-50 years associated snow load. For buildings of normal importance category, $I_s = 1$. The other parameters are: $C_b = 0.8$, $C_w = 1$, $C_a = 1$, $S_s = 2.6$ kPa and $S_r = 0.4$ kPa. Employing Eq. (3.1) it results $S = 2.48$ kPa.

All girders and secondary beams were designed to satisfy both strength and serviceability limit state. As for the strength requirement, the sections were selected to fulfill the equation: $M_f/M_r < 1$, where M_f is the factored moment obtained from the gravity load combinations, and M_r is the beam's moment resisting. The girders were designed to carry the reactions of the secondary beams, which run along the E-W direction, and resist the loads coming from the slabs. The beams are pinned to the column faces.

To design the gravity columns, the live load reduction factor was taken into consideration as specified in NBC 2015; hence, for office buildings where LL is less than 4.8 kPa and the tributary area is greater than 20 m^2 , the live load reduction factor is calculated as follows:

$$\text{LLRF} = 0.3 + \sqrt{9.8/B} \quad 3.2$$

where B is the cumulated tributary area.

The slenderness of gravity columns loaded in compression is limited to 200 as per CSA/S16-14 and the sections were selected to be at least Class 3. Columns are continuous over two storeys and are pinned at their base. Beams, girders and gravity columns are made of W-shape with $F_y = 345$ MPa.

3.1.1.2 Seismic and wind design

Office buildings are of normal importance category and the importance factor for earthquake is $I_E = 1$. In accordance with the Equivalent Static procedure, the seismic weight W is taken as the total dead load in addition to 25% of the snow load and the fundamental period T_a is calculated as per Eq. (2.4). However, NBC allows using a greater fundamental period up to $2T_a$ when using dynamic analysis for final design.

A three-dimensional building model was developed using ETABS (CSI, 2018). The model was used to assess the first mode period of the building and to estimate the interstorey drifts at the service level associated with the dynamic distribution of the forces through the linear Response Spectrum Analysis (RSP) corresponding to Site class C in Montreal.

As aforementioned, columns of braced frames are continuous over two storeys and are pinned at their base. All beam-to-column and brace-to-column connections are pinned. The composite steel

deck was defined as rigid diaphragm and the distribution of the storey shear along the building height is used to design the brace members of LFRSs.

The brace members are made of hollow structural sections (HSS) with yield strength $F_y = 350 \text{ MPa}$ and the probable yield stress $R_y F_y$ not less than 460 MPa. For beams and columns of CBFs, W-shape sections are considered.

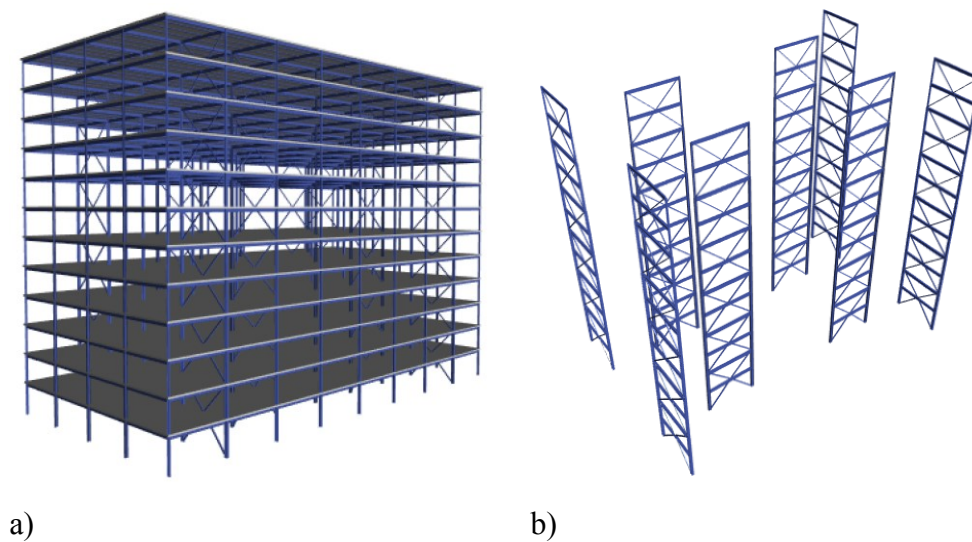


Fig. 3.3. 3D ETABS model for the 12-storey CBF building: a) structural components and b) the Lateral Force Resisting System (LFRS).

3.1.2 Design of the 12-storey MD-CBFs building ($R_d = 3$)

Following the Equivalent static procedure, the design period is $2T_a = 2.18 \text{ s}$, where T_a is the fundamental period calculated from the Eq. (2.4). The seismic weight for the 12-storey building is $W = 89632 \text{ kN}$. In this case study, the ductility and overstrength-related force modification factors are $R_d = 3$, $R_0 = 1.3$, respectively. Since the design period $2T_a$ is greater than 2 s, the base shear used in the design is $V_{E,min} = 1563 \text{ kN}$, where the design spectral acceleration $S(2.0) =$

0.068 g for site class C in Montreal. The concentrated force at the top of the structure is $F_t = 219 \text{ kN}$ as per Eq. (2.6).

The fundamental period of the first mode in the N-S direction obtained from ETABS is $T_1 = 2.57 \text{ s}$ and the base shear obtained from the nonlinear response spectrum analysis is $V_{E_dyn} = 1403 \text{ kN}$, where $V_{E_dyn}/V_E = 0.898 \geq 0.8$ which is acceptable for regular buildings.

The distribution of the lateral seismic force, 1.0E (1-in-2475 years) along the building height is shown in Table 3.1. Due to the symmetry of the building, the base shear is distributed equally between the 4 MD-CBFs located in the N-S direction. Then the notional load and the P- Δ effect are added. As resulted, the P- Δ effect contributes to the increase of shear force as resulted from Table 3.1.

The first mode frequency $f_n = 1/2.568 = 0.39 \text{ Hz}$. Hence, the building is classified as dynamically sensitive to wind load (NBC, 2015) and the dynamic procedure is required. The wind importance factor is $I_W = 1$ for office buildings; the reference velocity pressure $q = 0.42 \text{ kPa}$ and the topographic factor $C_t = 1$. The gust factor $C_g = 2.358$ is calculated by considering the values $g_p = 3.834$, $\frac{\sigma}{\mu} = 0.354$ calculated from the following Eqs. (2.24; 2.25; 2.26).

Since the building is located in rough terrain in Montreal, the exposure factor C_e is calculated as per Eq. (2.23), Then, $C_{p_Windward} = 0.8$ and $C_{p_Leeward} = 0.5$ are calculated according with Eqs. (2.17) and (2.20), respectively.

Table 3.1. Vertical distribution of seismic force over the height of the 12-storey MD-CBFs building, $R_d = 3$, Site class C, Montreal.

St.	h_x	W_x	F_x	V_E	F_x/V_E	Notional load	U_2	V_E/CBF
	(m)	(kN)	(kN)	(kN)	-	(kN)	-	(kN)
12	3.6	7724.8	430.5	430.5	0.28	40.8	1.000	117.8
11	3.6	7441.2	187.1	617.7	0.12	86.7	1.113	193.6
10	3.6	7441.2	170.3	788.0	0.11	132.2	1.141	257.7
9	3.6	7441.2	153.4	941.4	0.10	177.6	1.140	312.6
8	3.6	7441.2	136.6	1078.0	0.09	223.0	1.154	366.9
7	3.6	7441.2	119.8	1197.8	0.08	268.3	1.133	406.4
6	3.6	7441.2	102.9	1300.7	0.07	313.6	1.145	450.6
5	3.6	7441.2	86.1	1386.8	0.06	358.9	1.127	480.3
4	3.6	7441.2	69.2	1456.0	0.04	404.2	1.139	515.6
3	3.6	7441.2	52.4	1508.4	0.03	449.5	1.126	537.1
2	3.6	7441.2	35.6	1544.0	0.02	494.7	1.142	564.3
1	4.0	7495.8	18.9	1562.8	0.01	540.0	1.115	570.7
Σ	43.6	89632	1563		1.00			

Table 3.2 shows the distribution of the factored wind load $1.4W_{wind}$ (1-in-500 years). Due to the symmetry of the building, the load is distributed equally between the 4 MD-CBFs in the N-S direction. Then, Fig. 3.4 shows the distribution of the factored wind load $1.4W_{wind}$ (1-in-500 years) and earthquake $1.0E$ (1-in-2475 years) for MD-CBF1 in the N-S direction. The wind load governs the design over the total height, except in the last three stories where the earthquake load prevails.

Table 3.2. Calculation of the wind force in the N-S direction for the 12-storey MD-CBF building, $R_d = 3$ in Montreal.

St.	h_x	Tributary area	$C_{e, \text{windward}}$	$C_{e, \text{leeward}}$	$C_{p, \text{windward}}$	$C_{p, \text{leeward}}$	p	W_{wind}	$1.4W_{\text{wind}}$	$1.4W_{\text{wind}}/\text{CBF}$
	(m)	(m ²)					(kPa)	(kN)	(kN)	(kN)
12	43.6	108.9	0.93	0.66	0.8	-0.5	1.06	115.23	161.33	40.33
11	40.0	217.8	0.89	0.66	0.8	-0.5	1.03	223.72	313.21	78.30
10	36.4	217.8	0.85	0.66	0.8	-0.5	0.99	216.67	303.34	75.84
9	32.8	217.8	0.80	0.66	0.8	-0.5	0.96	209.26	292.97	73.24
8	29.2	217.8	0.76	0.66	0.8	-0.5	0.92	201.43	282.01	70.50
7	25.6	217.8	0.71	0.66	0.8	-0.5	0.89	193.11	270.35	67.59
6	22.0	217.8	0.66	0.66	0.8	-0.5	0.85	184.17	257.84	64.46
5	18.4	217.8	0.60	0.66	0.8	-0.5	0.80	174.47	244.25	61.06
4	14.8	217.8	0.54	0.66	0.8	-0.5	0.75	163.76	229.26	57.31
3	11.2	217.8	0.50	0.66	0.8	-0.5	0.72	156.90	219.66	54.91
2	7.6	217.8	0.50	0.66	0.8	-0.5	0.72	156.90	219.66	54.91
1	4.0	229.9	0.50	0.66	0.8	-0.5	0.72	165.61	231.86	57.96
Σ								2161	3026	756

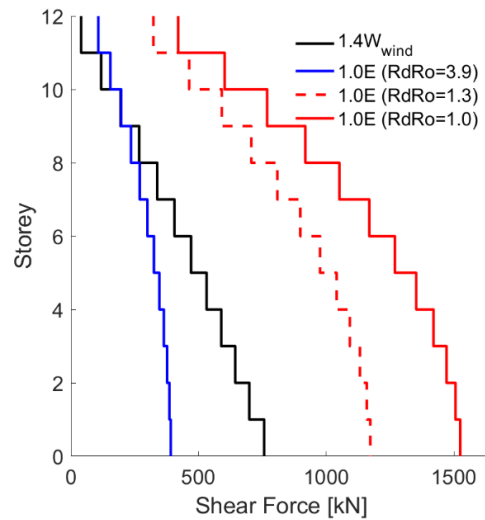


Fig. 3.4. Vertical distribution of seismic loads and wind loads in the N-S direction (MD-CBF1) over the height of the 12-storey MD-CBF building ($R_d = 3.0$).

The member sections of MD-CBF1 and the demand to capacity ratio of HSS braces, C_f/C_r , resulted under wind and earthquake loads are provided in Table 3.3. In the upper floors, the ratio C_f/C_r resulted under the wind load is relatively small when comparing to the corresponding ratio under earthquake load. Still, this ratio is almost equal to “1”: 0.99 and 0.98 in the first and second floors respectively, and the wind demand in the third floor slightly exceeds the capacity by 10% which is expected to be accommodated by the inherent system overstrength ($R_0 = 1.3$).

The selected sections provide a sufficient stiffness to satisfy the serviceability limits. The largest drift under the service wind ($0.75W$) was within the code limits ($0.25\% h_s$), while the earthquake-induced drifts take larger value but still in the code range ($< 2.5\% h_s$) for office buildings as plotted in Fig. 3.5.b.

Table 3.3 . Members' sections for MD-CBF1 of the 12-storey building and the governing load (1.0E) or (1.4W).

St.	Braces (HSS)	Beams	Columns	Governing act. E or W _{wind}	C _{f,E} /C _r	C _{f,Wind} /C _r
12	88.9X88.9X4.8	W460X128	W200X41.7	E	0.68	0.31
11	102X102X7.9	W460X128	W200x41.7	E	0.93	0.81
10	102X102X7.9	W460X128	W250x89	E	0.65	0.60
9	114.3X114.3X7.9	W460X128	W250x89	W (14%>E)	0.93	0.95
8	114.3X114.3X7.9	W460X128	W310x129	W (25%>E)	0.70	0.78
7	139.7X139.7X7.9	W460X128	W310x129	W (36%>E)	0.98	0.77
6	139.7X139.7X7.9	W460X128	W310x202	W (45%>E)	0.76	0.66
5	139.7X139.7X7.9	W460X128	W310x202	W (53%>E)	0.75	0.94
4	139.7X139.7X7.9	W460X128	W310x283	W (62%>E)	0.60	0.82
3	139.7X139.7X7.9	W460X128	W310x283	W (71%>E)	0.82	1.10
2	139.7X139.7X7.9	W460X128	W310x375	W (81%>E)	0.65	0.98
1	152.4X152.4X9.5	W460X128	W310x375	W (94%>E)	0.82	0.99

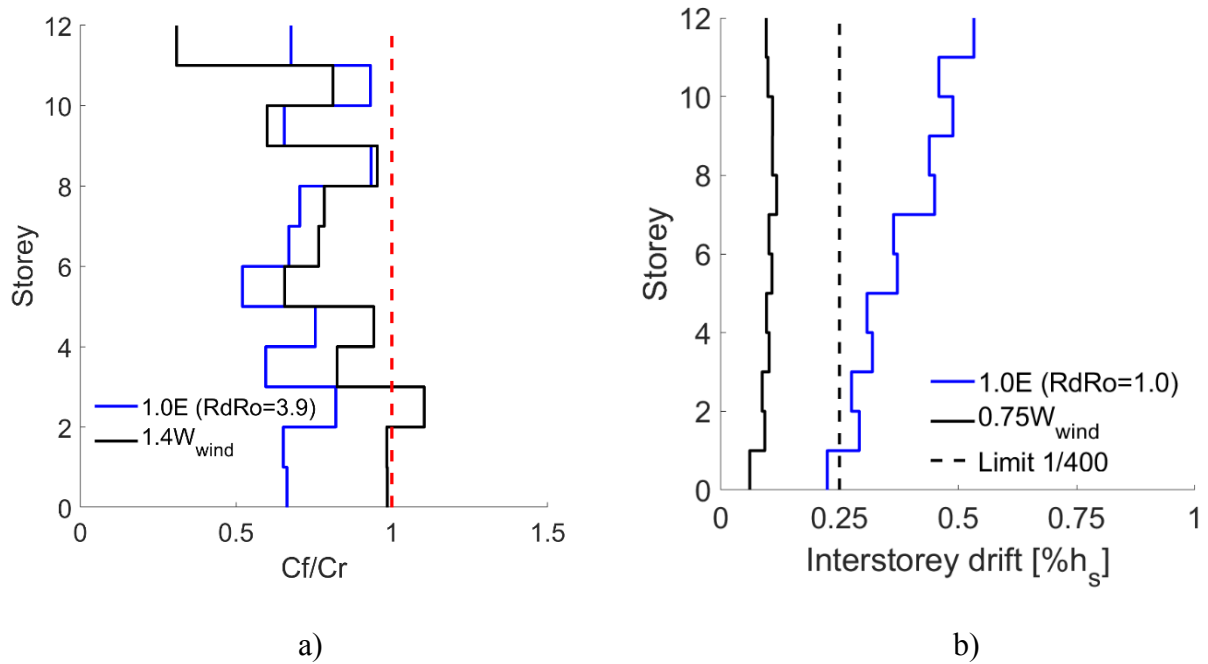


Fig. 3.5. 12-storey MD-CBF building: (a) demand to capacity ratio of the axial forces in the HSS braces, (b) elastic interstorey drift under earthquake and wind at serviceability level.

3.1.3 Design of the 16-storey LD-CBFs building ($R_d = 2$)

Regarding the 16-storey LD-CBFs building, the design period is $2T_a = 2.9$ s, where T_a is the fundamental period calculated with Eq. (2.4), where the building height is 58 m.

The seismic weight of building is $W = 119397$ kN. The ductility and overstrength-related force modification factors are $R_d = 2$ and $R_o = 1.3$, respectively. Since the design period is $2T_a > 2.0$ s, the base shear used in design is $V_{E_min} = 3123$ kN, where $S(2.0) = 0.068$ g for site class C, in Montreal. The concentrated force at the top of the building is $F_t = 437$ kN and the distribution of lateral force along the building height is computed using Eq. (2.5). The distribution of the lateral seismic force, 1.0E (1-in-2475 years), is shown in Table 3.4. Due to the symmetry of the building,

the base shear is distributed equally between the 4 CBFs in the N-S direction. Then, the notional load and the P- Δ effects are added.

Meanwhile, the first mode period in the N-S direction obtained from ETABS model is $T_1 = 3.551$ s and the base shear obtained from the nonlinear response spectrum analysis is $V_{E_dyn} = 2628$ kN where $V_{E_dyn}/V_E = 0.842 \geq 0.8$ which is acceptable for regular buildings.

The first mode frequency $f_n = 1/3.551 = 0.28$ Hz. Therefore, the building is also classified as dynamically sensitive to wind load (NBC, 2015) and the dynamic procedure is required. The wind importance factor is $I_W = 1$ for the office buildings, the reference velocity pressure is $q = 0.42$ kPa for Montreal and the topographic factor is $C_t = 1$. The gust factor $C_g = 2.52$ is calculated by considering the values $g_p = 3.809$, $\frac{\sigma}{\mu} = 0.399$ calculated from the following Eqs. (2.24), (2.25) and (2.26), respectively.

Table 3.4. Vertical distribution of the seismic shear force over the height of the 16-storey LD-CBFs building, $R_d = 2$, Site class C, Montreal.

St.	h_x	W_x	F_x	V_E	F_x/V_E	Notional load	U_2	V_E/CBF
	(m)	(kN)	(kN)	(kN)	-	(kN)	-	(kN)
16	3.6	7724.8	761.7	761.7	0.24	40.8	1.000	200.6
15	3.6	7441.2	293.2	1054.9	0.09	86.7	1.000	285.4
14	3.6	7441.2	273.8	1328.7	0.09	132.2	1.122	405.8
13	3.6	7441.2	254.4	1583.1	0.08	177.6	1.117	486.6
12	3.6	7441.2	235.0	1818.2	0.08	223.0	1.130	569.2
11	3.6	7441.2	215.6	2033.8	0.07	268.3	1.123	638.2
10	3.6	7441.2	196.2	2229.9	0.06	313.6	1.132	709.7
9	3.6	7441.2	176.8	2406.7	0.06	358.9	1.123	765.2
8	3.6	7441.2	157.4	2564.1	0.05	404.2	1.131	825.8
7	3.6	7441.2	138.0	2702.1	0.04	449.5	1.119	868.6
6	3.6	7441.2	118.6	2820.7	0.04	494.7	1.127	918.6
5	3.6	7441.2	99.2	2919.9	0.03	540.0	1.109	944.7
4	3.6	7441.2	79.8	2999.6	0.03	585.3	1.117	984.1
3	3.6	7441.2	60.4	3060.0	0.02	630.5	1.102	1000.5
2	3.6	7441.2	41.0	3101.0	0.01	675.8	1.111	1030
1	4.0	7495.8	21.7	3122.7	0.01	721.0	1.000	961
Σ		119397	3123		1.00			

Since the building is located in rough terrain in Montreal the exposure factor C_e is calculated with Eq. (2.23). Then, $C_{p_Windward} = 0.8$ and $C_{p_Leeward} = 0.6$ are calculated according with Eqs. (2.17) and (2.20), respectively.

Table 3.5 shows the elevation of the factored wind load $1.4W_{wind}$ (1-in-500 years) over the building height. Due to the symmetry of the building, the load is distributed equally between the 4 LD-CBFs located in the N-S direction.

Fig. 3.6 shows the distribution of the factored wind load $1.4W_{wind}$ (1-in-500 years) and earthquake $1.0E$ (1-in-2475 years) along the height of LD-CBF1, located in N-S direction. In the upper five floors, the wind load ($1.4W_{wind}$) is smaller than the earthquake ($1.0E$) and design is governed by earthquake load. The opposite is true in the case of lower floors where the wind load governs the design.

Table 3.5. Calculation of the wind force in the N-S direction for the 16-storey LD-CBFs building, $R_d = 2$ in Montreal.

St.	h_x	Tributary area	$C_{e, \text{windward}}$	$C_{e, \text{leeward}}$	$C_{p, \text{windward}}$	$C_{p, \text{leeward}}$	p	W_{wind}	$1.4W_{\text{wind}}$	$1.4W_{\text{wind}}/$ CBF
	(m)	(m ²)					(kPa)	(kN)	(kN)	(kN)
16	58.0	108.9	1.07	0.76	0.80	-0.50	1.30	142.0	198.9	49.72
15	54.4	217.8	1.03	0.76	0.80	-0.50	1.28	277.9	389.0	97.26
14	50.8	217.8	1.00	0.76	0.80	-0.50	1.25	271.5	380.0	95.01
13	47.2	217.8	0.96	0.76	0.80	-0.50	1.22	264.8	370.7	92.68
12	43.6	217.8	0.93	0.76	0.80	-0.50	1.18	257.9	361.1	90.26
11	40.0	217.8	0.89	0.76	0.80	-0.50	1.15	250.7	351.0	87.74
10	36.4	217.8	0.85	0.76	0.80	-0.50	1.12	243.2	340.4	85.10
9	32.8	217.8	0.80	0.76	0.80	-0.50	1.08	235.2	329.3	82.33
8	29.2	217.8	0.76	0.76	0.80	-0.50	1.04	226.9	317.6	79.40
7	25.6	217.8	0.71	0.76	0.80	-0.50	1.00	218.0	305.2	76.29
6	22.0	217.8	0.66	0.76	0.80	-0.50	0.96	208.4	291.8	72.94
5	18.4	217.8	0.60	0.76	0.80	-0.50	0.91	198.0	277.3	69.31
4	14.8	217.8	0.54	0.76	0.80	-0.50	0.86	186.6	261.2	65.31
3	11.2	217.8	0.50	0.76	0.80	-0.50	0.82	179.3	251.0	62.74
2	7.6	217.8	0.50	0.76	0.80	-0.50	0.82	179.3	251.0	62.74
1	4.0	229.9	0.50	0.76	0.80	-0.50	0.82	189.2	264.9	66.23
Σ								3529	4940	1235

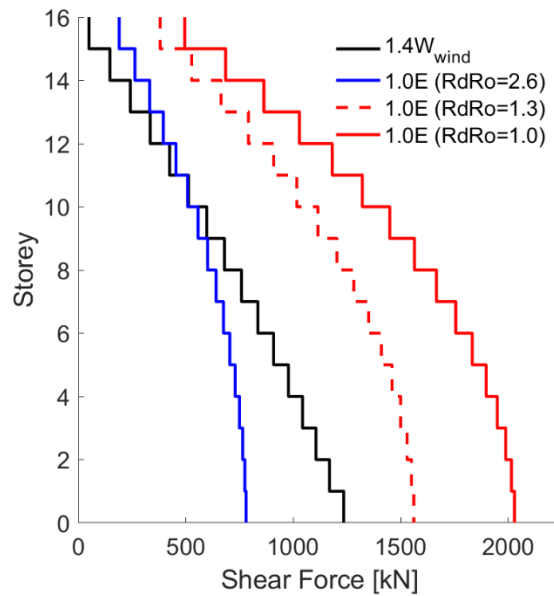


Fig. 3.6. Vertical distribution of seismic loads and wind loads along LD-CBF1 of 16-storey building ($R_d = 2.0$), considering N-S direction.

The member sections of LD-CBF1 and the ratio of the demand C_f to the capacity C_r for braces subjected to wind and earthquake loads are given in Table 3.6. In the upper floors, the ratio C_f/C_r of braces resulted under wind load is relatively small compared to the corresponding ratio resulted under earthquake. However, this ratio increases toward the lower floors. The wind demand in the first, third, and seventh floors slightly exceed by 2%, 4% and 1% respectively; however, such demand is expected to be accommodated by the inherent system overstrength ($R_0 = 1.3$).

The selected sections provide a sufficient stiffness to satisfy the serviceability limit state which is evident when checking the interstorey drift. The largest drift under the service wind ($0.75W_{wind}$) was within the code limits ($0.25\% h_s$), while the earthquake-induced drifts take larger value but still in the code range ($< 2.5\% h_s$) for office buildings, as plotted in Fig. 3.7.b

Table 3.6. Members' sections for LD-CBF1 of the 16-storey building and the governing load (1.0E) or (1.4W).

St.	Braces (HSS)	Beams	Columns	Governing action E or W_{wind}	$C_{f,E}/C_r$	$C_{f,Wind}/C_r$
16	88.9X88.9X7.9	W460X106	W250X58	E	0.79	0.22
15	102X102X9.5	W460X128	W250X58	E	1.02	0.71
14	102X102X9.5	W460X128	W250X89	E	0.90	0.54
13	114.3X114.3X12.7	W460X128	W250X89	E	0.93	0.71
12	114.3X114.3X12.7	W460X128	W310X129	E	0.80	0.60
11	139.7X139.7X9.5	W460X106	W310X129	W (1%>E)	0.81	0.68
10	139.7X139.7X9.5	W460X128	W310X202	W (7%>E)	0.71	0.60
9	139.7X139.7X9.5	W460X106	W310X202	W (13%>E)	0.94	0.85
8	139.7X139.7X9.5	W460X128	W310X283	W (18%>E)	0.82	0.76
7	139.7X139.7X9.5	W460X106	W310X283	W (24%>E)	1.04	1.01
6	139.7X139.7X9.5	W460X144	W310X375	W (29%>E)	0.92	0.91
5	152.4X152.4X9.5	W460X106	W310X375	W (34%>E)	0.91	0.94
4	152.4X152.4X9.5	W460X144	W360X421	W (39%>E)	0.80	0.85
3	152.4X152.4X9.5	W460X106	W360X421	W (45%>E)	0.96	1.04
2	152.4X152.4X9.5	W460X144	W360X509	W (51%>E)	0.84	0.95
1	152.4X152.4X12.7	W460X144	W360X509	W (58%>E)	0.82	1.02

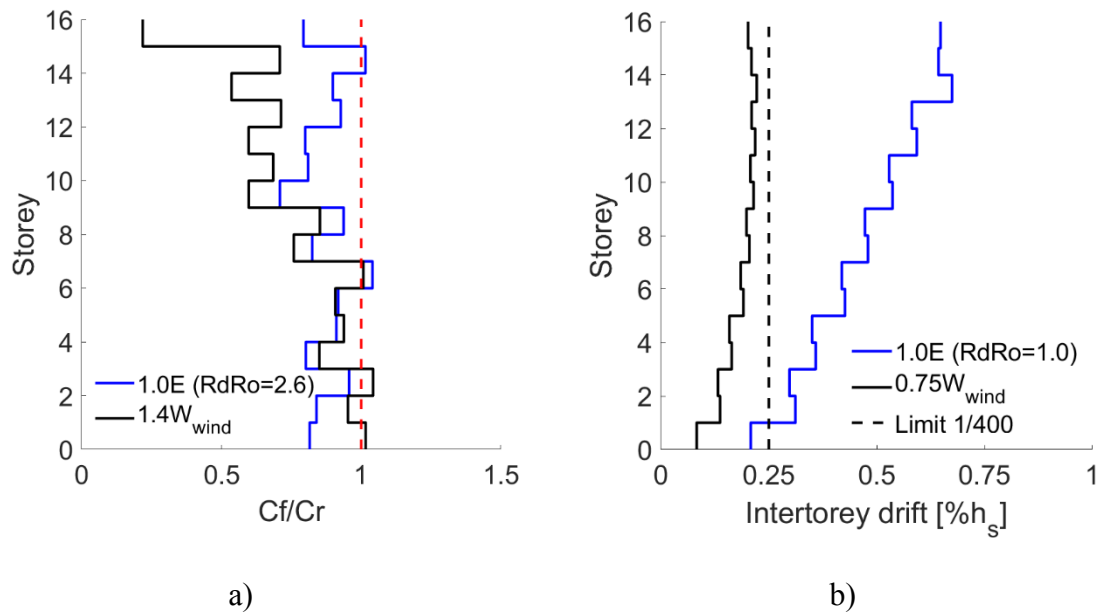


Fig. 3.7. 16-storey LD-CBF building: a) demand to capacity ratio of the axial forces in the HSS braces, b) elastic interstorey drift for earthquake and wind at serviceability level.

4. CHAPTER 4. MODELING AND NONLINEAR DYNAMIC ANALYSIS

4.1 Seismic data for the Nonlinear Dynamic Analysis

Montreal is located in Eastern Canada and is in a moderate seismic region. According to the NBC Guidelines (NRC 2015), a set of minimum seven ground motions are required to perform a reliable performance assessment of a building through the nonlinear dynamic analysis. Due to the lack of historical records in Eastern Canada, a set of seven artificial ground motions selected from the Engineering Seismology Toolbox (<http://www.seismotoolbox.ca>) are considered in the analysis. The duration of each record ranges between 18.0 and 20.0 s. Then, 10 s zero pads were added in the end of the signal to allow for free vibration simulations and accurate prediction of the residual structural response during nonlinear response history analysis (NRHA).

The artificial ground motions correspond to magnitude $M=7$ with epicentral distance ranging between 13.8 km and 50.3 km. Their main features are illustrated in Table 4.1, where PGA and PGV stand for the peak ground acceleration and the peak ground velocity respectively, t_D is the significant duration, and T_p and T_m are the peak and the mean periods of the ground motion, respectively. It is worth mentioning that the significant duration, t_D , is the time interval in which the central 90%, spaced between the 5% and the 95%, of the contribution to the integral of the square of the accelerogram take place (Trifunac and Brady 1975).

The seven artificial ground acceleration time histories are illustrated in Fig. 4.1.

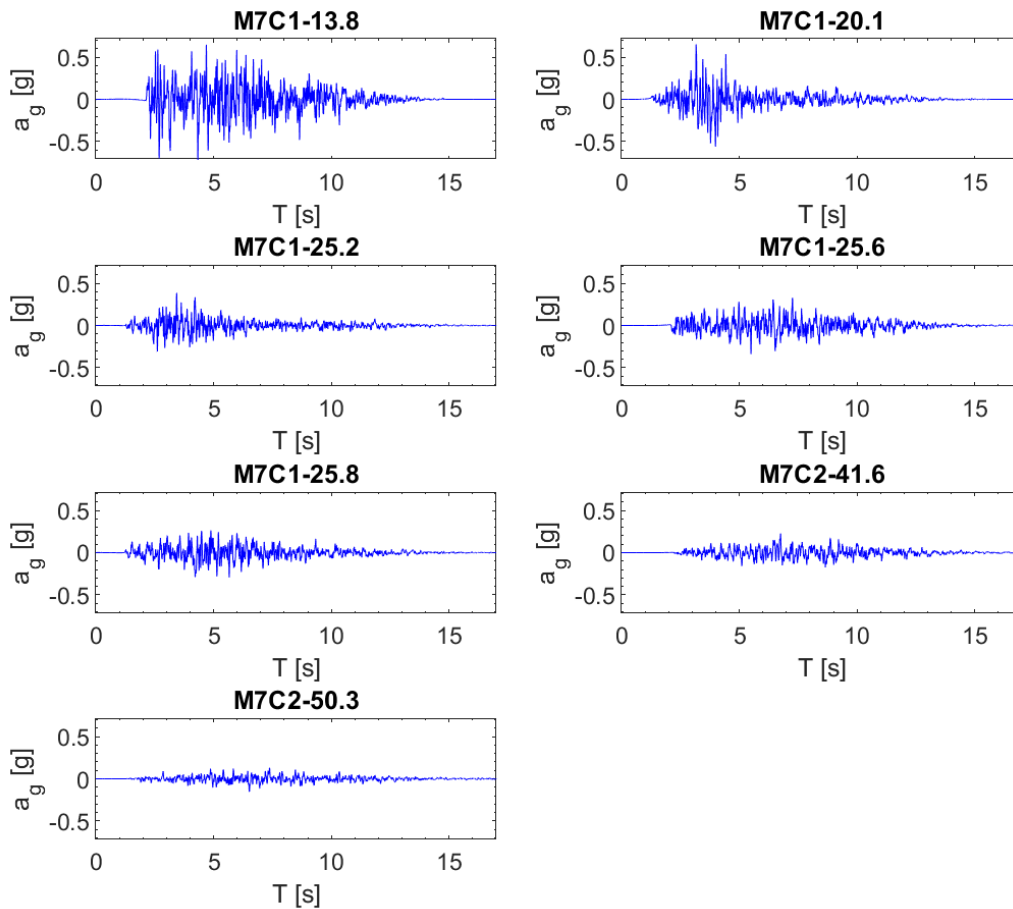


Fig. 4.1. The seven simulated ground motions used in NRHA.

The ground motions were scaled linearly in time in the range $0.2T_l - 2T_l$ so that their mean response spectrum matches or be above the NBC design spectrum for Montreal, Site class C, which corresponds to a probability of exceedance of 2% in 50 years (2475-year return period).

Note that the scaled mean spectrum should not fall below 90% of the design spectrum in the range of interest. The scale factors used in the analysis of the 12-storey and 16-storey buildings are also provided in Table 4.1. The design spectrum for Montreal, Site class C, and the scaled spectrum

compatible response spectra and their mean associated with the 12-storey and 16-storey buildings period are shown in Fig. 4.2.a and b respectively.

Table 4.1. Ground motion characteristics and scaling factors (SF) for the 12- and 16-storey buildings.

Event*	M _w	Station	PGA (g)	PGV (m/s)	PGA/PGV	t _D [s]	T _P [s]	T _m [s]	SF	SF
									12-st	16-st
M7C1-13.8	7.0	Simulated	0.727	0.370	0.052	7.180	0.12	0.244	0.44	0.6
M7C1-20.1	7.0	Simulated	0.653	0.396	0.062	6.012	0.14	0.296	0.8	0.6
M7C1-25.2	7.0	Simulated	0.386	0.187	0.049	7.320	0.06	0.243	1.3	1.2
M7C1-25.6	7.0	Simulated	0.339	0.194	0.058	7.846	0.16	0.266	1.2	1.0
M7C1-25.8	7.0	Simulated	0.293	0.178	0.062	7.308	0.08	0.282	1.0	1.1
M7C2-41.6	7.0	Simulated	0.229	0.144	0.064	7.614	0.14	0.306	1.2	1.4
M7C2-50.3	7.0	Simulated	0.151	0.075	0.051	8.744	0.16	0.277	2.1	2.2

*<http://www.seisnotoolbox.ca>

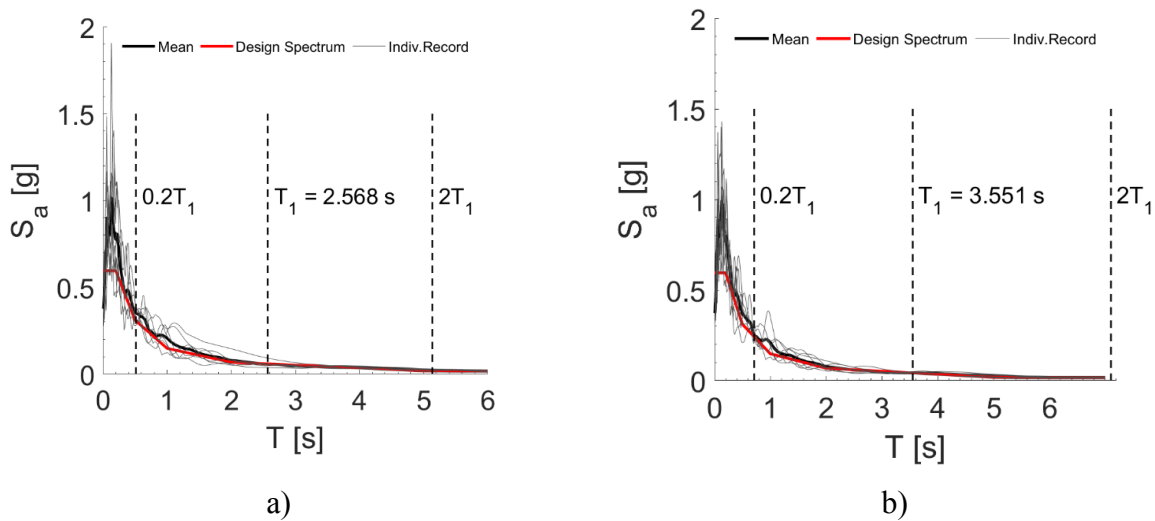


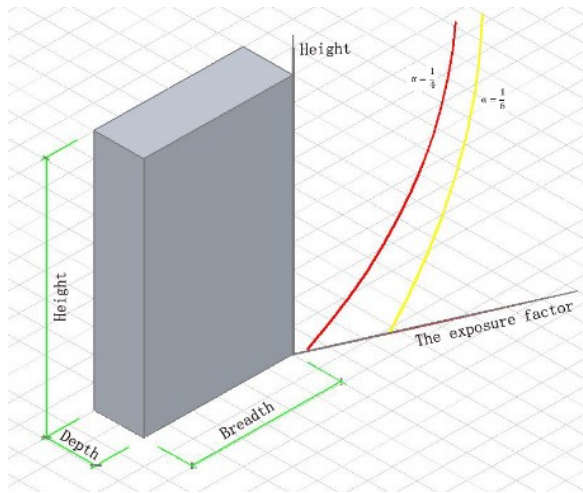
Fig. 4.2. Design spectrum for Montreal, Site class C, and response spectra of 7 spectrum compatible ground motions and their mean for: a) 12-storey MD-CBF and b) 16-storey LD-CBF buildings.

4.2 Wind Aerodynamic Database of High-rise Buildings

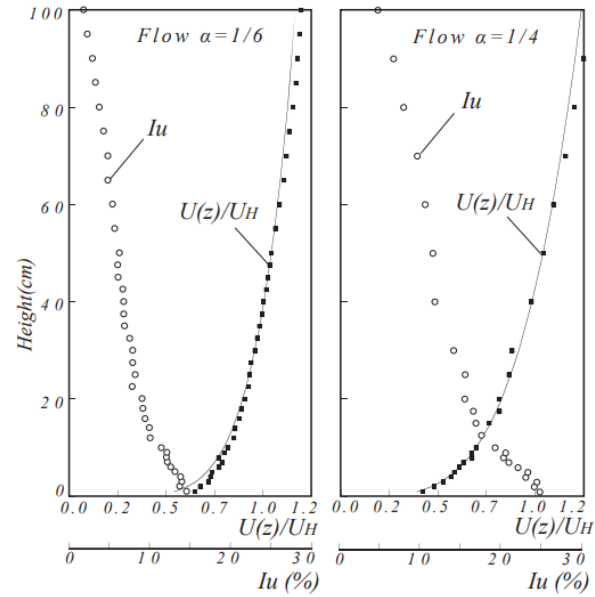
The aerodynamic data were derived from the Tokyo Polytechnic University (TPU) aerodynamic database available at <http://wind.arch.t-kougei.ac.jp/system/eng/contents/code/tpu>. The TPU database was developed as part of the *Wind Effects on Buildings and Urban Environment, the 21st Century Center of Excellence Program* in Tokyo, Japan (TPU, 2021). The database provides researchers and engineers with aerodynamic wind tunnel test data on low- and high-rise buildings with different configurations in various boundary layers. In this study, we are focusing on tall buildings characterized by B (breadth), D (depth) and H (height) ratios as shown in Fig. 4.3.a.

The aerodynamic database of high-rise buildings contains time series of local wind pressure coefficients measured on 22 scaled rigid models subjected to 394 wind tunnel tests.

The case study 12-storey and 16-storey buildings have the following plan dimensions $B = 60.5$ m and $D = 30.5$ m, while the heights are $H = 43.6$ m and 58 m, respectively. The corresponding geometrical ratios (B/D/H) are 200/100/145 for the 12-storey building and 200/100/193 for the 16-storey building. The considered TPU model has B/D/H = 200/100/200. The geometric scale of the test model (L) is 1/400, corresponding to full-scale building dimensions: $H = 80$ m, $B = 80$ m, and $D = 40$ m. Also, the wind profile exponent $\alpha = 0.25$ considered in the tests corresponds to a suburban terrain which is the only terrain configuration considered in the wind testing of high-rise models with (B/D/H = 2/1/2). The sampling frequency during the tests was $f_s = 1000$ Hz and the sample time step is equal to: $dt_s = 1/1000 = 0.001$ s.



a)



b)

Fig. 4.3. TPU database: a) geometric dimensions query ratio for high-rise buildings, and b) vertical profiles of incoming wind flow for $\alpha = 1/6$ & $1/4$ (www.wind.arch.t-kougei.ac.jp/info_center/windpressure/highrise/Homepage/homepageHDF.htm).

By assuming the velocity scale (V) equal to $1/2$ and to convert the aerodynamic pressure coefficients from the sample into a full-scale pressure value based on consistent scaling, the time step in the full scale becomes: $dt = T \cdot dt_s = 200 \cdot 0.001 = 0.2 \text{ s}$, where the time scale (T) is calculated from the similarity of the Strouhal number in the full and wind tunnel scale.

Fig. 4.4 below illustrates the model geometrical parameters, and the location of the pressure taps on the windward, leeward, and sideward faces of the considered TPU model with $H = 0.2 \text{ m}$, $B = 0.2 \text{ m}$, $D = 0.1 \text{ m}$. There are only 8 measuring stations along the model height, hence, there is the need to map the existing tap locations to the floor levels of the 12-storey and 16-storey buildings studied herein. This is done in a simplified way, assuming that the ground and top floor correspond

to the 0.0 m and 0.2 m levels of the scaled model shown in Fig. 4.4 and evaluating all intermediate floor levels by linear interpolation of the existing measurements.

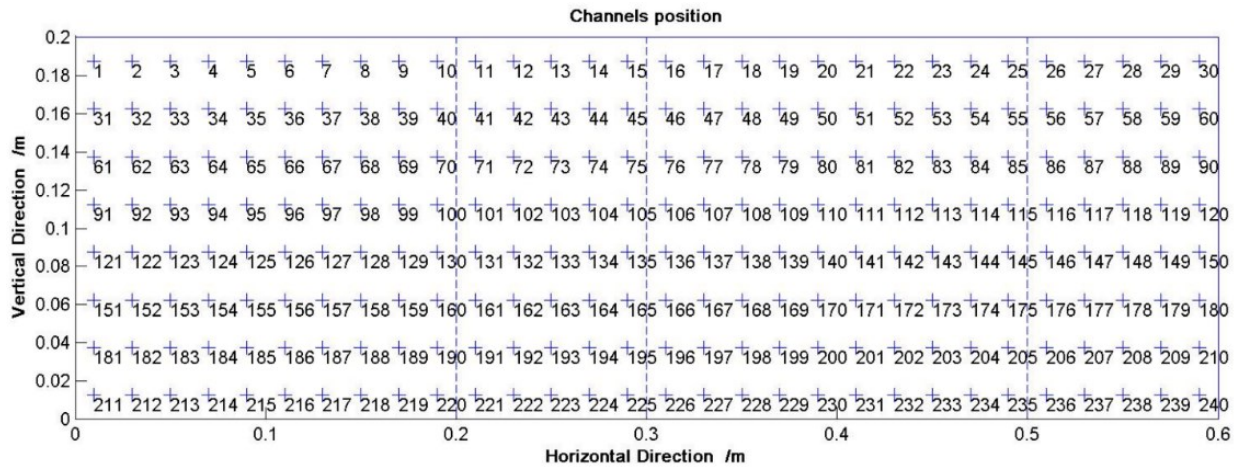


Fig. 4.4. Locations of the pressure taps on the windward, leeward and sideward faces of the considered high-rise building model with $H = 0.2\text{m}$, $B = 0.2\text{m}$, $D = 0.1\text{m}$, length scale = 1/400 (http://www.wind.arch.t-kougei.ac.jp/info_center/windpressure/highrise/Test_Result/T212_4_channels.jpg).

The model was subjected to 21 different wind attack angles varying from 0^0 to 100^0 . In this thesis, only the wind corresponding to the incidence angle 0^0 (N-S) is considered since it is the most critical as shown in Fig. 4.5. Thus, the peak values of the net pressure coefficients ($C_p C_{g,max}$) derived from the TPU database and lumped at the floor levels of the 12-storey and 16-storey buildings are computed and plotted in the figure. It is evident that the wind direction 0^0 is the most critical, providing the highest value for $C_p C_g$.

Fig. 4.6 shows the extreme wind pressure coefficients on a high-rise building at Windward, Leeward and Sideward faces of a high-rise building with $H = 0.2\text{ m}$, $B = 0.2\text{ m}$, $D = 0.1\text{ m}$ for attacking angle $\theta = 0^0$.

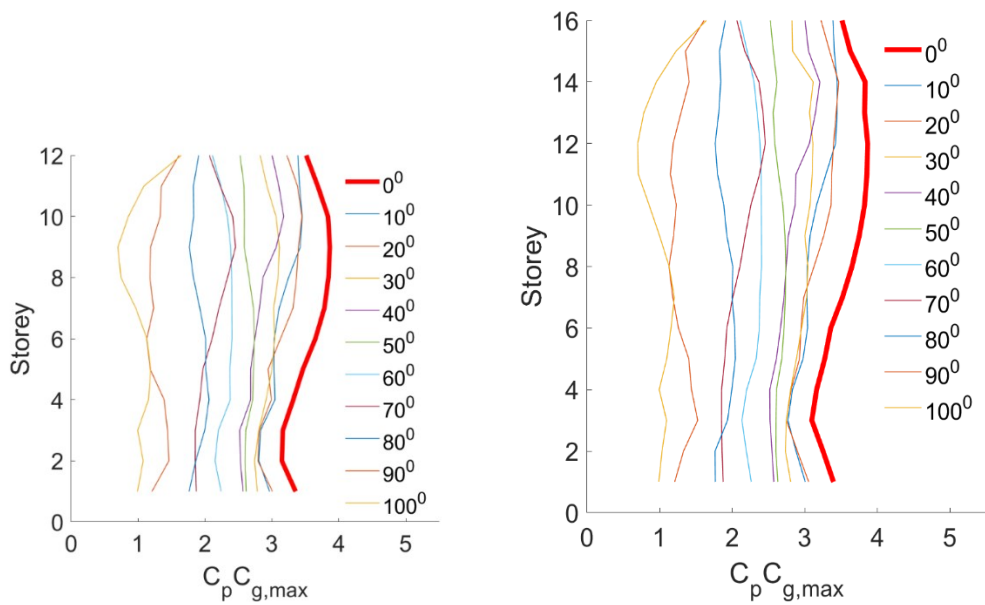


Fig. 4.5. Peak values of the net pressure coefficients, $C_p C_{g,max}$ derived from the TPU database for wind directions $0-90^\circ$ and assessed at each storey level for the: a) 12-storey and b) 16-storey buildings.

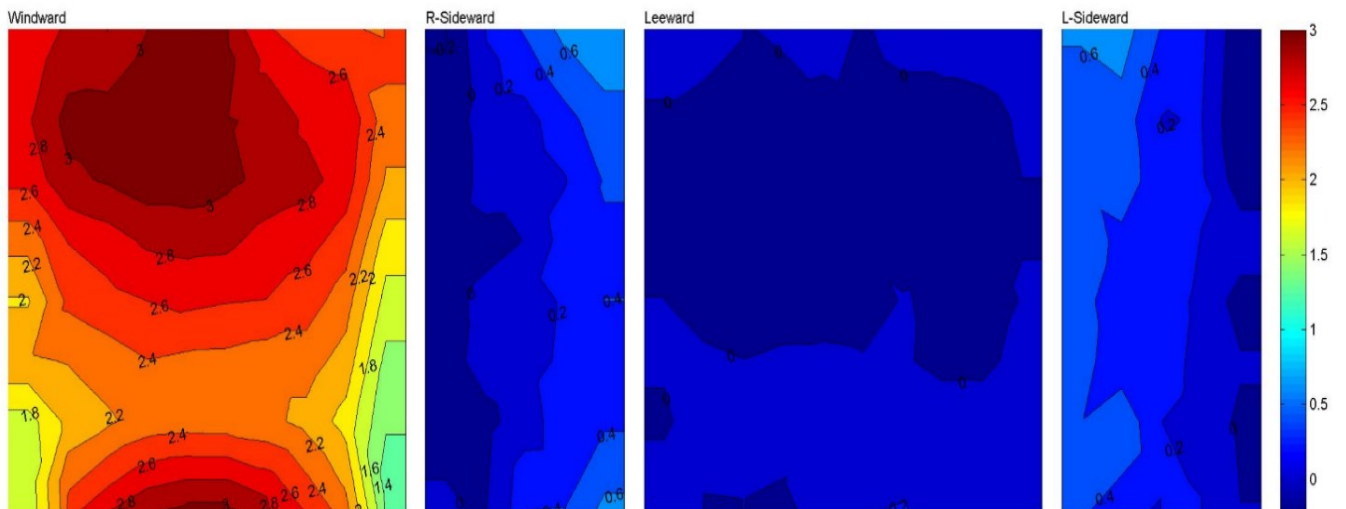


Fig. 4.6. Positive extreme wind pressure coefficients on a high-rise building at windward, leeward and sideward faces of the TPU scaled model with $H = 0.2$ m, $B = 0.2$ m, $D = 0.1$ m, model scale = $1/400$, $\theta = 0^\circ$ (http://www.wind.arch.t-kougei.ac.jp/info_center/windpressure/highrise/Test_Result/T212_4_000_max.jpg).

Fig. 4.7 and Fig. 4.8 show the time history of the net external pressure coefficients ($C_{net} = C_p C_g$) at the floor levels of the 12-storey and the 16-storey office building respectively. The mean value of the net coefficient is plotted in red.

The reference wind speed considered in the TPU database is measured at the roof level. Since NBC (2015) makes reference to the annual maxima of 60 minutes moving average wind speed at height of 10 m, the power law can be used to evaluate the wind velocity at heights greater than 10 m:

$$V_{ref} = V_{10} \left(\frac{h}{Z_{10}} \right)^\alpha \quad 4.1$$

Where V_{ref} is the wind speed in (m/s) at the height of the building $Z = h$ and V_{10} is the wind speed at height ($Z_{10} = 10 \text{ m}$) as per (NBC, 2015). In Eq. (4.1), α is the wind profile exponent taken as 1/4 for suburban areas.

The pressure histories $p(t)$ on the windward or leeward surfaces of the building can be easily calculated by multiplying the non-dimensional pressure coefficient $C_p C_g(t)$ obtained from the TPU database by the reference wind pressure:

$$p(t) = q_{ref} \cdot C_p C_g(t) \quad 4.2$$

Hence, the reference wind pressure q_{ref} is calculated using the Bernoulli's formula:

$$q_{ref} = \frac{1}{2} \rho V_{ref}^2 \quad 4.3$$

where ρ is the density of the air.

Then, the wind-induced forces acting at each storey level $F_D(t)$ can be calculated by multiplying the net pressure at each time step $p(t)$ by the corresponding tributary area A_{trib} (Table 3.5).

$$F_D(t) = p(t) \cdot A_{trib} \quad 4.4$$

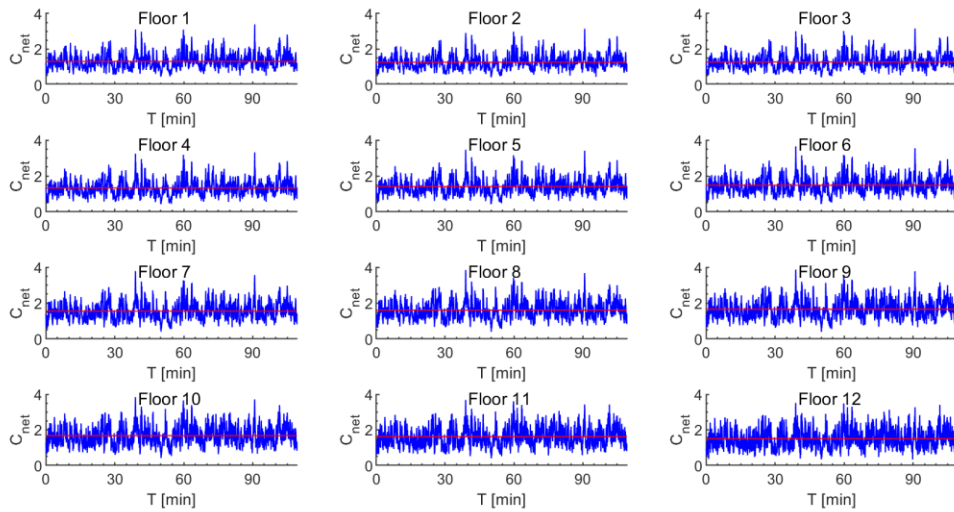


Fig. 4.7. Net pressure coefficient time histories at the floor levels of the 12-storey building model for wind acting at $\theta=0^0$. The mean coefficient is shown in red.

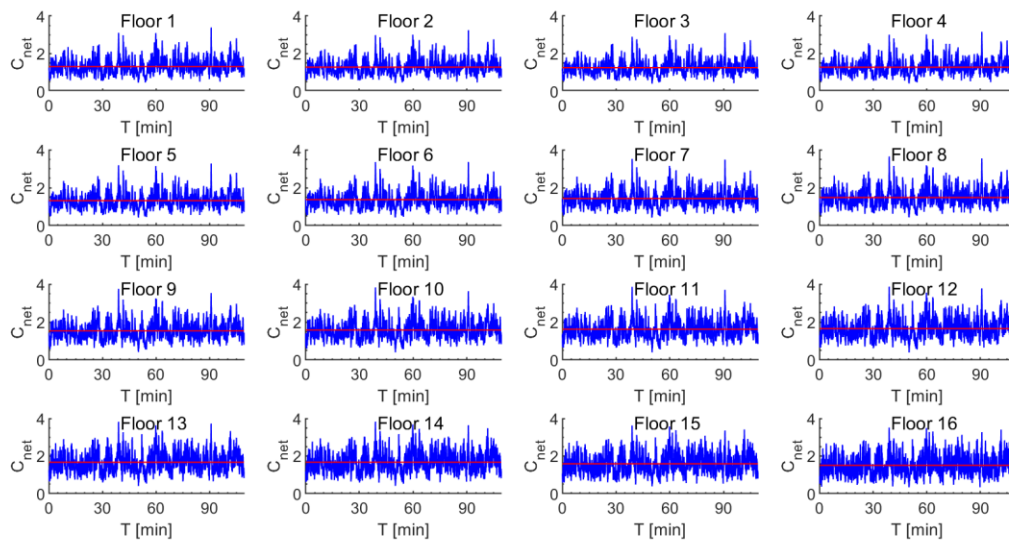


Fig. 4.8. Net pressure coefficient time histories at the floor levels of the 16-storey building model for wind acting at $\theta=0^0$. The mean coefficient is shown in red.

Fig. 4.9 compares the peak and the mean TPU-derived drag forces for the 12-storey and 16-storey buildings with the corresponding nominal wind loads, defined as per the NBC dynamic procedure.

The matching between peak experimental and design wind loads is satisfactory; hence, the experimental loads being always less than the corresponding nominal loads.

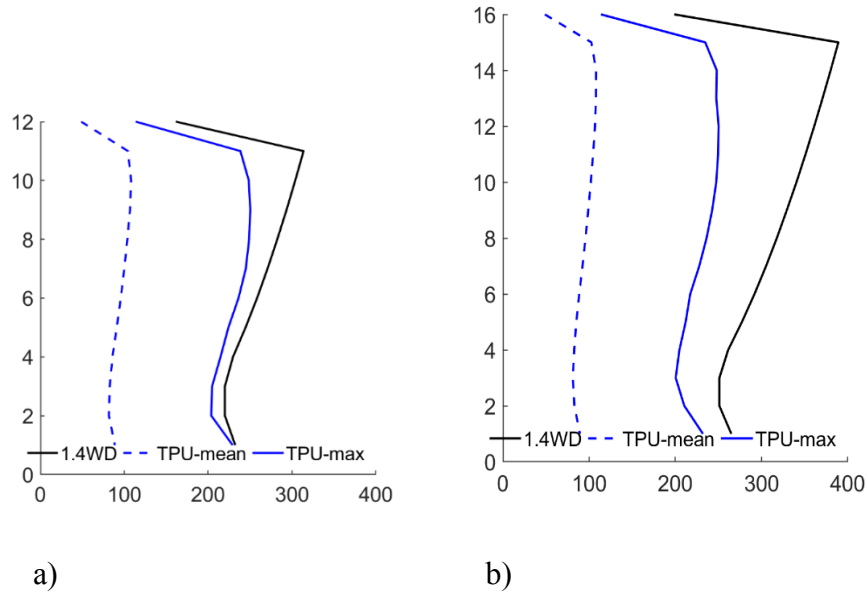


Fig. 4.9. Peak and mean values of the experimental wind load compared to the design wind load (1.4W) calculated as per the (NBC, 2015) for the, a) 12-storey building, b) 16-storey building.

4.2.1 Monte Carlo Simulations

Monte Carlo simulation is a mathematical technique that uses a wide range of computational algorithms to obtain approximate solutions based on repeated random sampling. Since the TPU provides only one set of wind tunnel data at each attack angles, the Monte Carlo simulations were implemented to generate additional wind time history realizations; hence, 500-random-wind realizations were generated with the purpose to assess the dynamic behavior of the archetypes subjected to strong wind.

The wind data were generated in MATLAB using the beta-distribution through the command *pearsrnd* and input parameters the mean, standard deviation, skewness and kurtosis of the TPU-

derived forces; for a detailed description of the wind event generation the interested reader is referred to Athanasiou et al (2022a) and Athanasiou et al (2022b).

4.3 Numerical Model in OpenSees

In order to assess the nonlinear behavior of the archetype office buildings under wind and earthquake load, a detailed two-dimensional nonlinear numerical model was developed using the Open System for Earthquake Engineering Simulation (OpenSees) framework.

Owing to the symmetry of the building in both orthogonal directions, the two-dimensional model in the N-S direction was developed to represent one quarter of the structure's floor area including one concentrically braced frame (CBF1) resisting the lateral and the gravity loads, as well as the tributary gravity columns are illustrated in Fig. 4.10. The model accounts for the P- Δ effect and large displacements. All the floor masses were lumped at the floor levels and the elevation of the numerical model is shown in Fig. 4.11.

All CBF members as braces, beams, and columns were modeled using the line-element modeling approach (Hsiao et al. 2013). Hence, the HSS brace members were modeled using 16 force-based nonlinear beam-column elements with distributed plasticity and three Gauss-Lobatto integration points per element.

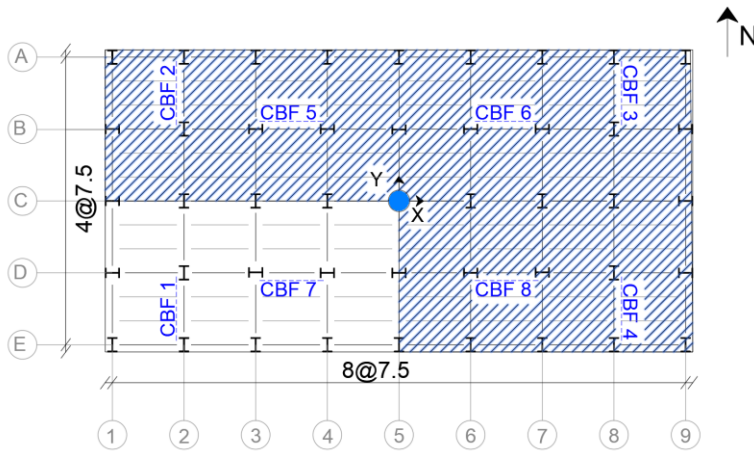


Fig. 4.10. The typical floor plan and $\frac{1}{4}$ floor area considered in the analysis.

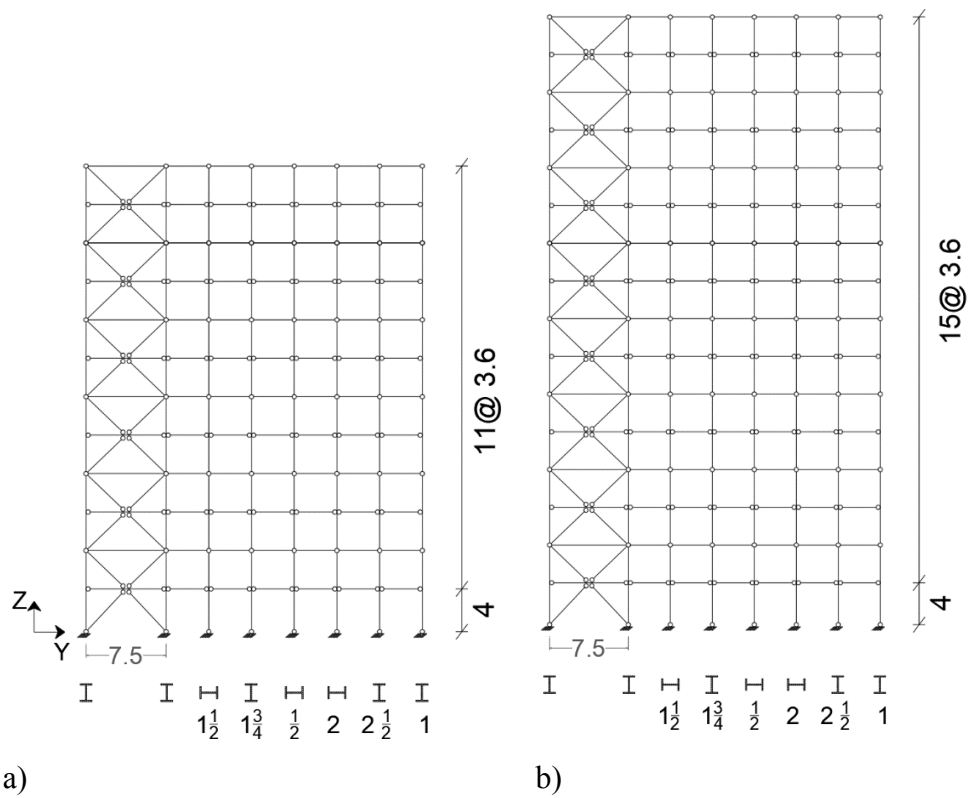


Fig. 4.11. OpenSees model of the a) 12-storey and b) 16-storey buildings with CBF-1 acting in the N-S direction and carrying $\frac{1}{4}$ of the load with the participating gravity columns.

The geometrical out-of-plane buckling of the braces was considered by assigning an initial imperfection magnitude equal to 1/500 of the effective brace length to allow the brace to buckle in the outer plane. The cross section was defined using the Fiber Discretization Technique and considering rounded fibers at the corners of the sections to detect any potential yielding or buckling. The cross section of HSS brace is discretized into a total of 240 quadrilateral shaped patches, 40 fibers for each edge segment and 20 fibers for corner segments. The material (*Steel02*), used to construct a uniaxial Giuffre-Menegotto-Pinto steel material object with isotropic strain hardening, is assigned to HSS braces, as well as to the I-shaped beam and column members of CBFs. Hence, the strain hardening is defined as $b = 1\%$.

To capture the failure that could happen due to low-cycle fatigue, a uniaxial material with fatigue properties is assigned to HSS braces and is wrapped to the parental *Steel02* material. Hence, the fatigue ductility exponent is considered as constant $m = -0.5$, whereas the fatigue ductility coefficient ϵ_0 , is calculated based on the Eq. (2.37) proposed by Tirca and Chen (2014).

For beams and columns of braced frames, the force-based nonlinear beam-column elements were assigned to capture the response of the assigned I-shape sections. For column members, an imperfection of $L/1000$ was assigned to allow buckling, where L is the column length which is equal to the storey height. The gravity columns were defined as elastic elements. The damping matrix is of Rayleigh type, evaluated assuming a damping ratio equal to 2% applied to the first and third vibration mode of the studied building. Damping was applied only on the degrees of freedom with masses and elastic/ linear elements. The brace simulation model and the cross section with the distribution of the fibers are illustrated in Fig. 2.2.

The model was initially developed to predict the seismic response of CBF buildings and can be used to assess the system performance under any lateral motion, such as wind.

5. CHAPTER 5. PERFORMANCE ASSESSMENT

5.1 Nonlinear Response Assessment at Design Level

Seismic and wind design of studied 12-storey MD-CBF and 16-storey LD-CBF office buildings, shown in Fig. 3.1 and Fig. 3.2, are presented in Chapter 3. Moreover, the results obtained from the equivalent static force procedure (ESFP) presented in Chapter 3 (e.g. building height, H , fundamental period T_a , and the base shear (V_E) are summarized in Table 5.1.

The 1-in-50-years wind pressure for Montreal is $q = 0.42$ kPa and the tributary cladding area (north facade) associated to the typical floors is $A_{trib} = 218$ m². For wind design, the dynamic procedure according to NBC (NRC, 2015) is applied and the wind base shear $1.4V_{wind}$ is also provided in the table.

Table 5.1. Characteristics of the studied CBFs buildings.

Struct. type	ESFP			Linear dynamic analysis (ETABS)			Eigenvalue analysis (OpenSees)				Dynamic analysis
	H	T_a	V_E	T_1	T_2	T_3	T_1	T_2	T_3	$S(T_1)$	$1.4V_{Wind}$
	[m]	[s]	[kN]	[s]	[s]	[s]	[s]	[s]	[s]	[g]	[kN]
12-st. ($R_d=3$)	43.6	2.18	1563	2.57	0.83	0.44	2.52	0.79	0.41	0.059	3026
16-st. ($R_d=3$)	58	2.9	3123	3.55	1.04	0.52	3.44	0.98	0.50	0.044	4940

The OpenSees nonlinear models, presented in Chapter 4, were used to evaluate the response of the archetype buildings under the suite of ground motions and wind realizations, shown also in Chapter 4. As aforementioned, the torsional effect is neglected in the analysis, while the notional loads and

the $P-\Delta$ effects are considered. Hence, the first three mode periods of the buildings obtained through eigenvalue analysis in OpenSees are very similar to the ones obtained from the 3-D ETABS model.

The engineering demand parameters (EDP) investigated independently under the wind and earthquake actions are: i) interstorey drifts (*ISDs*), ii) residual interstorey drifts (*RISDs*) and, iii) floor accelerations (*FAs*). The distribution of the selected EDP response over the height of the archetype buildings is also expressed in terms of the mean and the mean + standard deviation values ($\text{mean} + \sigma$).

5.1.1 Seismic response of buildings under design spectrum-compatible ground motion suite

The ground motions (GMs) used in analysis and the scale factor applied are presented in Table 4.1 and the scaled spectra are shown in Fig. 4.2.

5.1.1.1 Interstorey Drift of Buildings at D.L.

The interstorey drift (ISD) distributed along the 12-storey and 16-storey building height that resulted under each one of the 7 ground motions scaled to the design level, the mean of ISDs computed from the ground motion suite, and the ($\text{mean} + \sigma$) are plotted in Fig. 5.1. The ISD response under each individual ground motion is plotted in gray, the mean value of ISDs is plotted in black and the ($\text{mean} + \sigma$) is shown by a dashed black line. As illustrated, the ISD demand under the GMs tends to concentrate in the upper floors where extensive yielding occurs due to the higher mode effects.

In the case of the 12-storey MD-CBF building, higher drifts are observed at the 10th and 12th storey with a peak of mean interstorey drift among floors of $1.2\% h_s$, experienced at the top floor.

For the 16-storey LD-CBF building, the peak ISD is $1.0\% h_s$ and occurs at the 14th floor. In general, the 12-storey building experienced larger interstorey drifts compared to the 16-storey building. This is explained by the higher overstrength of the 16-storey building when comparing to the 12-storey building because both were designed for the same spectral acceleration ordinate $S(2.0)$ g, as per the building code requirement. Nevertheless, for both buildings, the peak of mean interstorey drift at design level is below the $2.5\% h_s$ code limit.

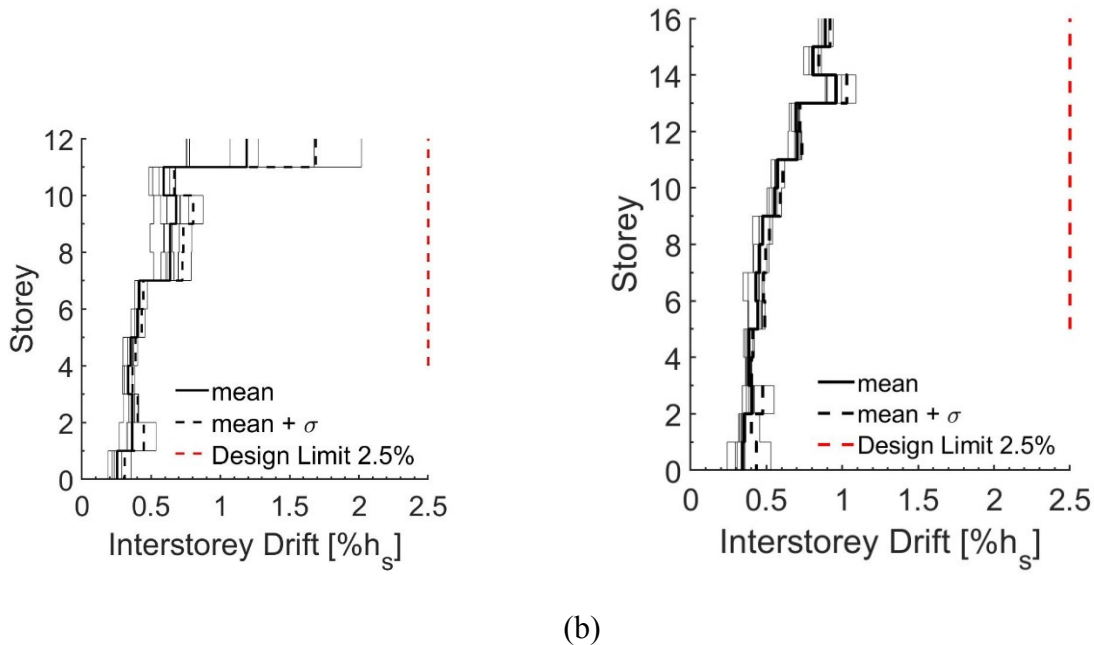


Fig. 5.1. The ISD distribution along the building height under GMs scaled to D.L.: a) 12-storey MD-CBF ($R_d=3$) and b) 16-storey LD-CBF ($R_d=2$).

5.1.1.2 Residual Interstorey Drift of Buildings at D.L.

The residual interstorey drift (RISD) of the studied 12-storey and 16-storey buildings subjected to the seven artificial ground motions scaled to the design level, is shown in Fig. 5.2.

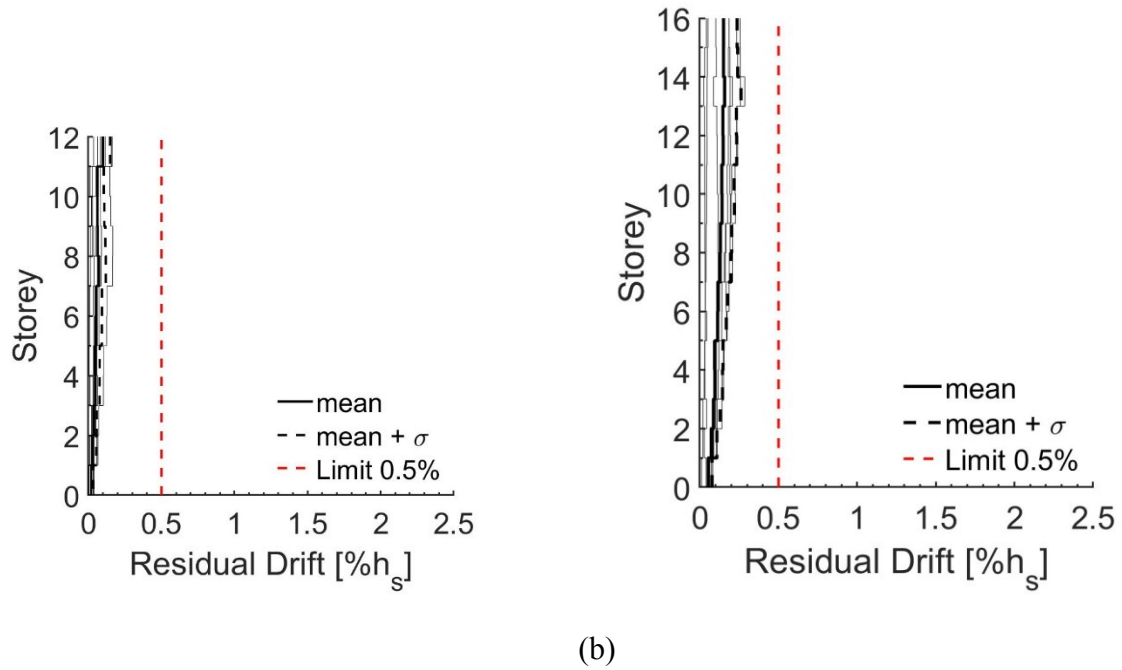


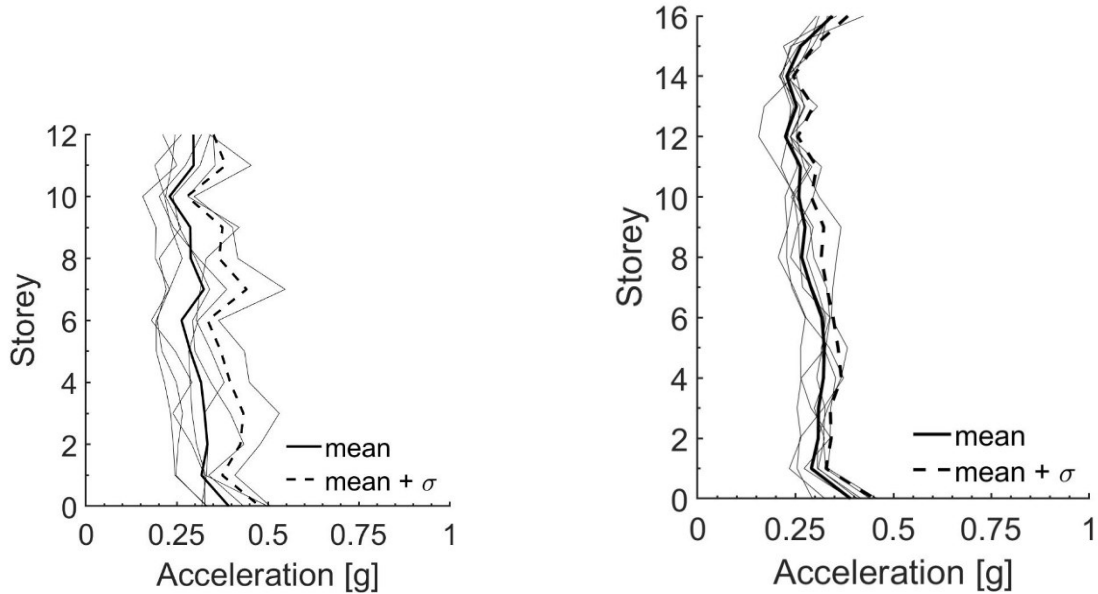
Fig. 5.2. The RISD distribution along the building height under GMs scaled to D.L.: a) 12-storey MD-CBF ($R_d=3$) and b) 16-storey LD-CBF ($R_d=2$).

As it can be seen from Fig. 5.2, the peak of mean residual interstorey drift (RISD) is always lower than ($0.5\% h_s$) in both considered case studies. According to researchers, the reparability limit state is associated with $0.5\% h_s$.

5.1.1.3 Floor Accelerations of Buildings at D.L.

The relative to the ground floor acceleration (FA) response of the studied 12-storey and 16-storey buildings, subjected to the seven artificial ground motions scaled to the design level, is illustrated in Fig. 5.3. As illustrated, the floor accelerations (FAs) are almost constant along the height of the buildings. The mean floor accelerations for the 12-storey MD-CBF building decreases upwards and the peak of mean FAs is 0.34 g observed at the 2nd level. While for the 16-storey building, it

results slightly lower demand than it is for the 12-storey buildings and shows a fluctuation between a minimum value of 0.22 g and a maximum value of 0.34 g at the top floor.



(a)

(b)

Fig. 5.3. The FA distribution along the building height under GMs scaled to D.L.: a) 12-storey MD-CBF ($R_d = 3$) and b) 16-storey LD-CBF ($R_d = 2$).

Fig. 5.4 compares the mean interstorey drift under GMs scaled to the design level, for the 12-storey MD-CBF building, before and after the braces of the 1st, 6th and 7th stories were slightly increased to respond elastically to wind load. As illustrated, significant decrease in the ISD demand happens in these stories. However, the mean interstorey drift, in the other floors, is slightly bigger and the trend of the mean drift is almost the same. This increase is limited and still within the code limit and no action is needed. It is expected to be higher for taller buildings and more research should be carried out to study the effect of increasing the stiffness on taller structures under seismic demands.

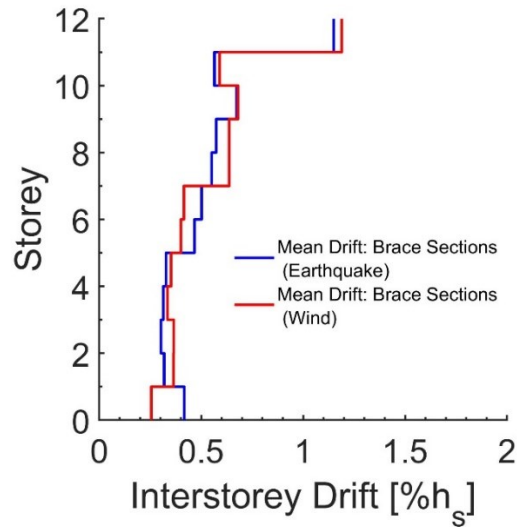
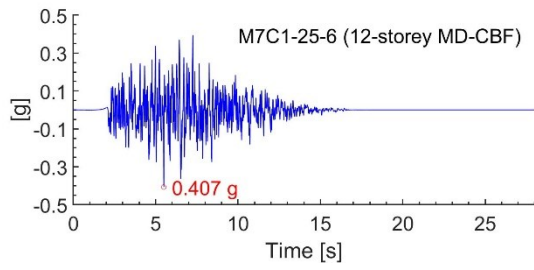


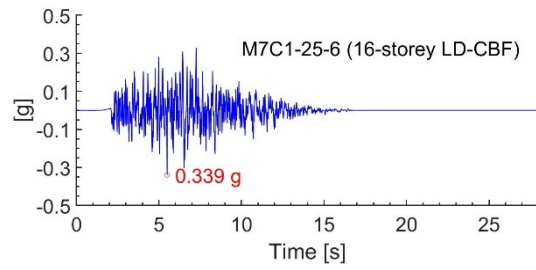
Fig. 5.4. Mean ISD distribution along the 12-storey building height under GMs scaled to D.L., when the 1st, 6th and 7th storey braces are increased for wind demand (W=Wind).

5.1.1.4 Nonlinear response of Buildings at D.L.

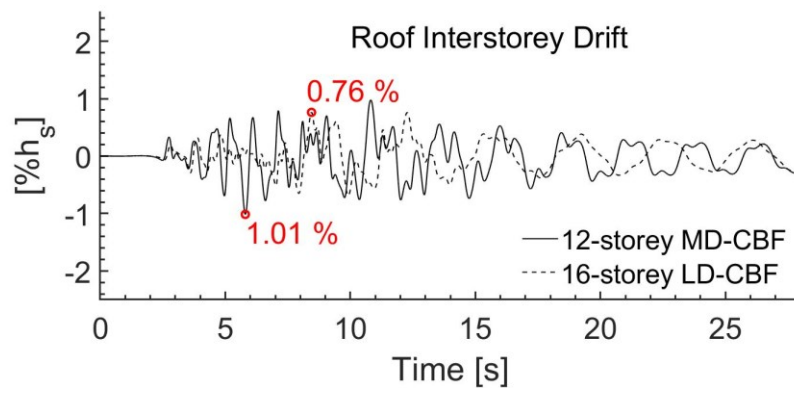
The time history ISD response of the top floor of 12-storey MD-CBF building under the M7C1_25_6 record scaled to design level, $S_a(T_1) = 0.059g$, is shown in Fig. 5.5.c and the scaled accelerogram is shown in Fig. 5.5.a. As depicted, the peak acceleration of the record is $0.407g$ and the maximum interstorey drift at the roof level is $1.01\% h_s$, which is within the code limit of $2.5\% h_s$ for office buildings. To show the difference in response among the 12-storey and 16-storey buildings, the time-history ISD of top floor of 16-storey LD-CBF building under the same M7C1_25_6 record scaled to design level, $S_a(T_1) = 0.044g$, is added with dashed line in Fig. 5.5.c. Under M7C1_25_6 record, the HSS braces respond in the nonlinear range; hence, the hysteresis behavior of the left and right HSS braces of the top floor of 12-storey MD-CBF building is plotted in Fig. 5.6a and that of top floor left and right HSS braces of 16-storey LD-CBF is shown in Fig. 5.6.c and d. As depicted, both braces of top floor of 12-storey building yield in tension.



a)



b)



c)

Fig. 5.5. Response of the 12-storey MD-CBF and 16-storey LD-CBF buildings under M7C1_25_6 record scaled to D.L.: a)-b) scaled accelerogram, c) time history ISD series at roof.

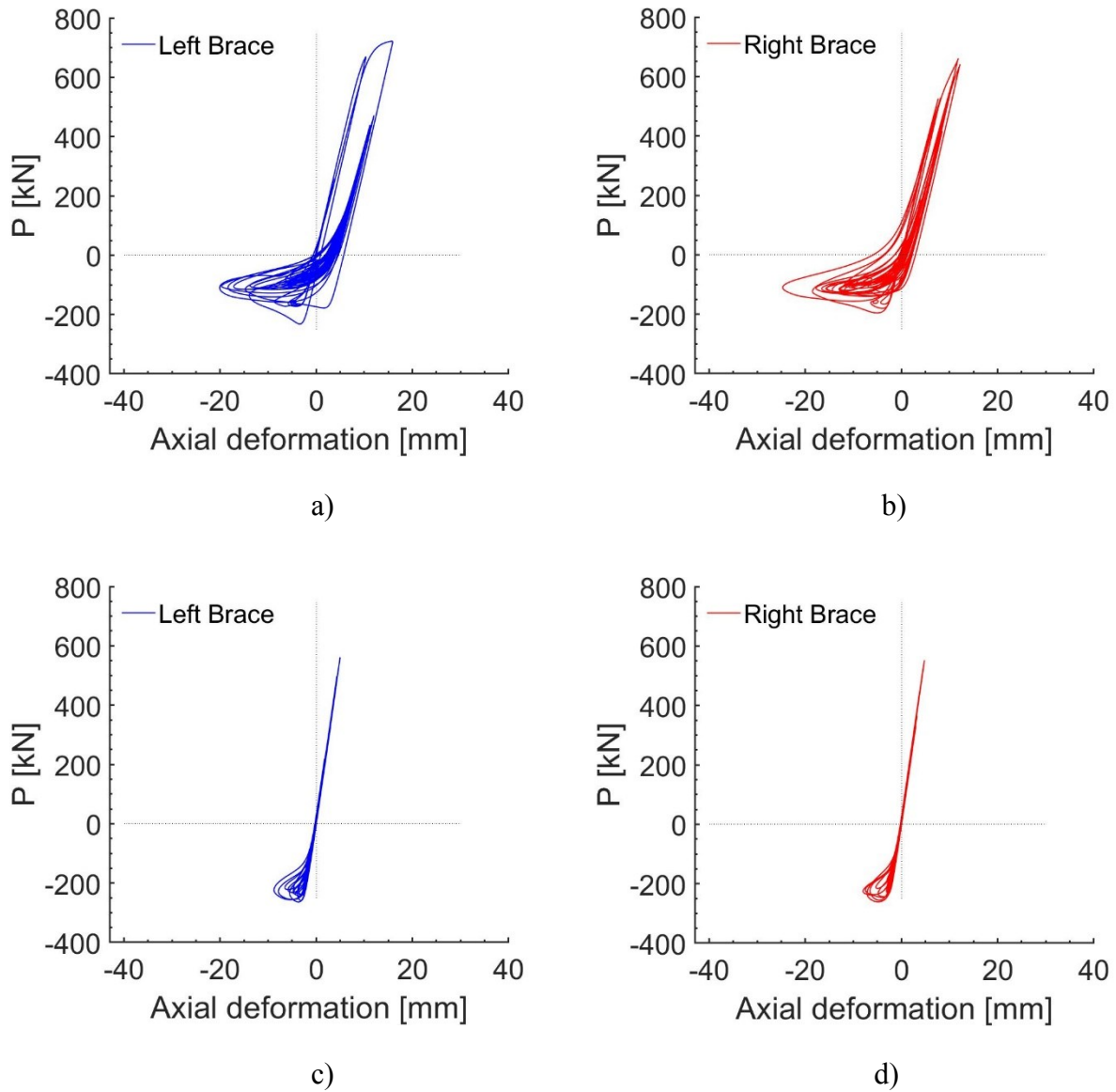


Fig. 5.6. Hysteresis response of the left and right HSS braces of top floor of studied buildings under M7C1_25_6 scaled to D.L.: a)-b) 12-storey MD-CBF and c)-d) 16-storey LD-CBF.

For the 16-storey LD-CBF building, the peak interstorey drift among floors occurs at the 14th storey under the M7C1_13_8 ground motion scaled to D.L. The time history ISD of 14th floor is shown in Fig. 5.7b and the scaled accelerogram is shown in Fig. 5.7a. As illustrated, the peak of record's acceleration is 0.436g and the peak interstorey drift at the 14th floor level is 1.12% h_s ,

which is also within the code limit of $2.5\% h_s$ for office buildings. The hysteresis response of the left and right HSS braces located at the 14th floor is illustrated in Fig. 5.7c and d.

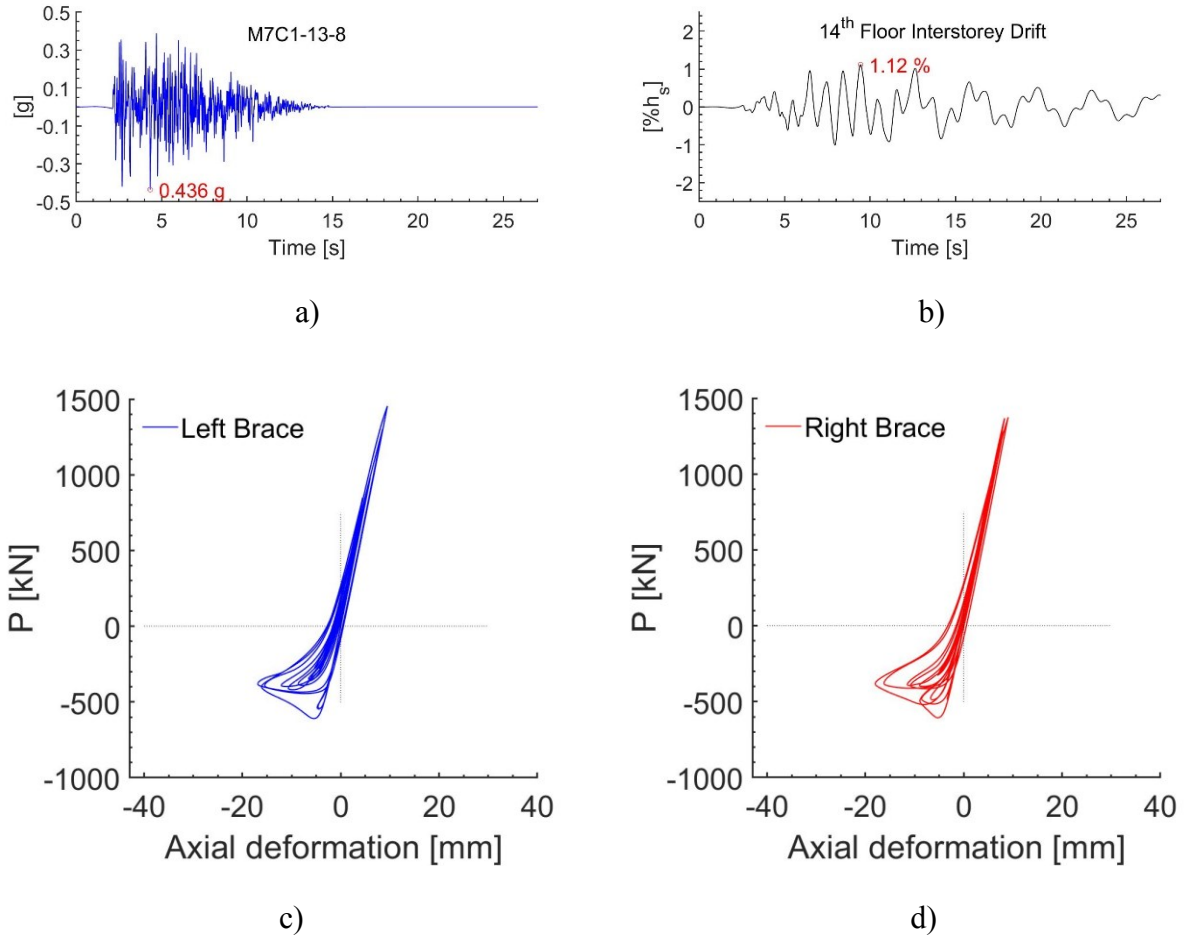


Fig. 5.7. Response of the 16-storey LD-CBF building under M7C1_13_8 scaled to D.L.: a) accelerogram, b) time history response of ISD of 14th floor, c)-d) hysteresis response of the left and right HSS braces of 14th floor.

5.1.2 Wind response of buildings to selected random events (Rand #1 - Rand #5) scaled to the design level

Five wind realizations labelled Rand #1 to Rand #5, discussed in Chapter 4, were used to excite the OpenSees models of the 12-storey and 16-storey buildings. The considered direction of applied wind force is N-S.

The dynamic time history response of the 12-storey MD-CBF building under wind Rand #3 realization, scaled to design level (*ULS*), is analyzed in terms of HSS braces response, which, according to the building code are required to behave elastically. Herein, the *ULS* is the ultimate limit state and *SLS* is the serviceability limit state. Although the interstorey drift (ISD) should be verified according to the *SLS*, where the importance factor is $I_w=0.75$, the time history ISD response computed for *ULS* is also shown for discussion purposes. Thus, Fig. 5.8a and b show the 120 min. drag forces history applied at 1st storey and the associated time history interstorey drift. The peak wind drag force shown in Fig. 5.8a is $FD = 485.5 \text{ kN}$ and the corresponding peak interstorey drift is $0.07\% h_s$, where h_s is the storey height. For the 1st floor, $h_s = 4.0 \text{ m}$ and at floors above is 3.6 m . According to building code, for buildings of normal importance category, the ISD associated to *SLS* should be $\leq h_s/400 = 10 \text{ mm}$ that corresponds to $0.25\%h_s$ for $h_s = 4.0 \text{ m}$. In Fig. 5.8c and d, the response of the left and right HSS braces of 1st floor of 12-storey MD-CBF under Rand # 3 wind is illustrated. As depicted, both braces respond in the linear range since they were designed to remain elastic under the wind force.

In the case of 12-storey MD-CBF building, the maximum axial force in bottom floor braces was registered under Rand #3 wind and in the case of 16-storey LD-CBF building under Rand #5 wind.

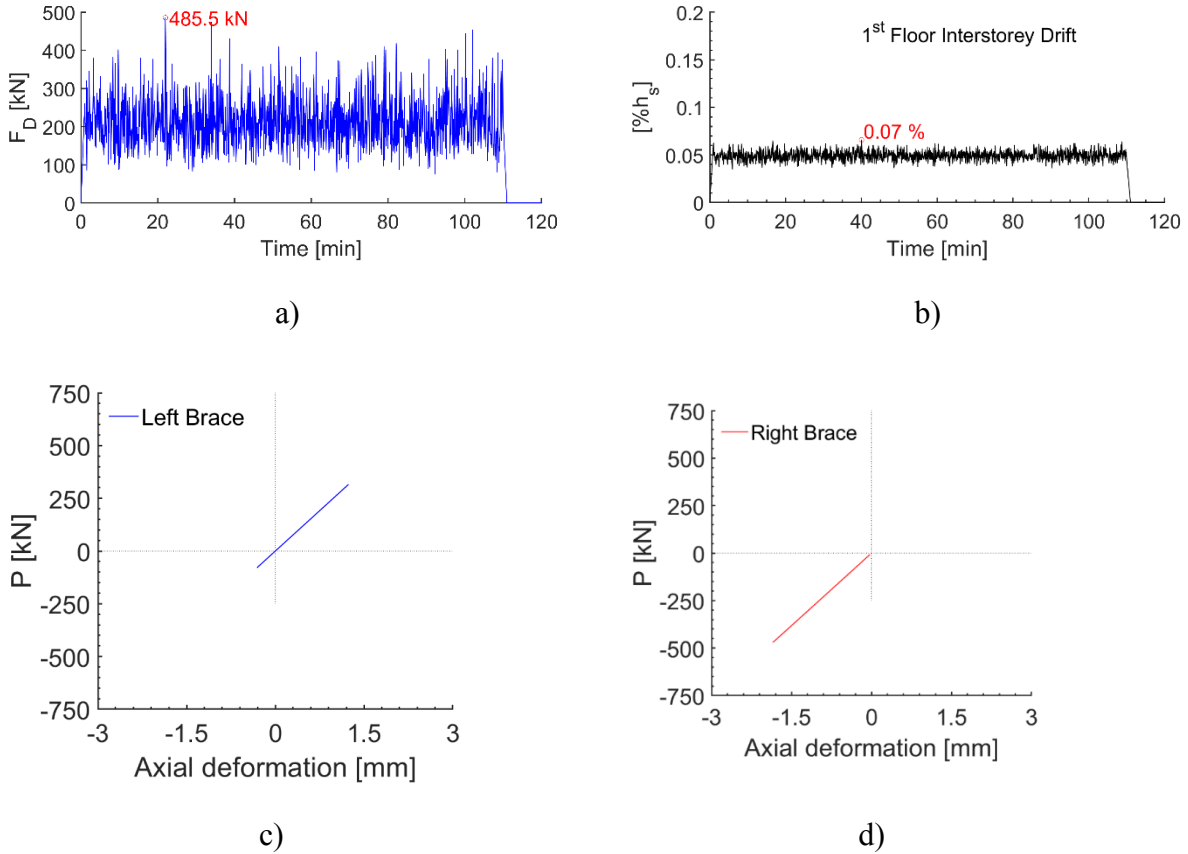


Fig. 5.8. First storey response of the 12-story MD-CBF building under wind Rand #3 realization, scaled to design level (*ULS*): a) 120 min. drag force history (Rand #3), b) time history of ISD and c)- d) hysteresis response of left and right HSS braces.

The nonlinear dynamic response of the 16-storey LD-CBF building under wind Rand #5 realization, scaled to design level (*ULS*), shows the peak response at 2nd floor. Fig. 5.9a and b show the wind Rand #5 time history applied at 2nd floor and the associated time history interstorey drift, respectively. As plotted in Fig. 5.9a, the peak wind drag force is $FD = 421.4 \text{ kN}$ and from Fig. 5.9b, it results that the peak ISD is $0.15\% h_s$, which is much below the code limit of $h_s/400 = 9 \text{ mm}$ or $0.25\%h_s$, where $h_s = 3.6 \text{ m}$. Fig. 5.9c and d show the elastic response of the left and right HSS braces of 2nd floor of 16-storey LD-CBF building. However, the wind-induced demand for the 16-storey building is bigger than that for the 12-storey building.

Similar to the previous 12-storey building, both 2nd floor HSS braces of 16-storey LD-CBF building behave elastically; hence, the elastic response of braces under wind demand is satisfied.

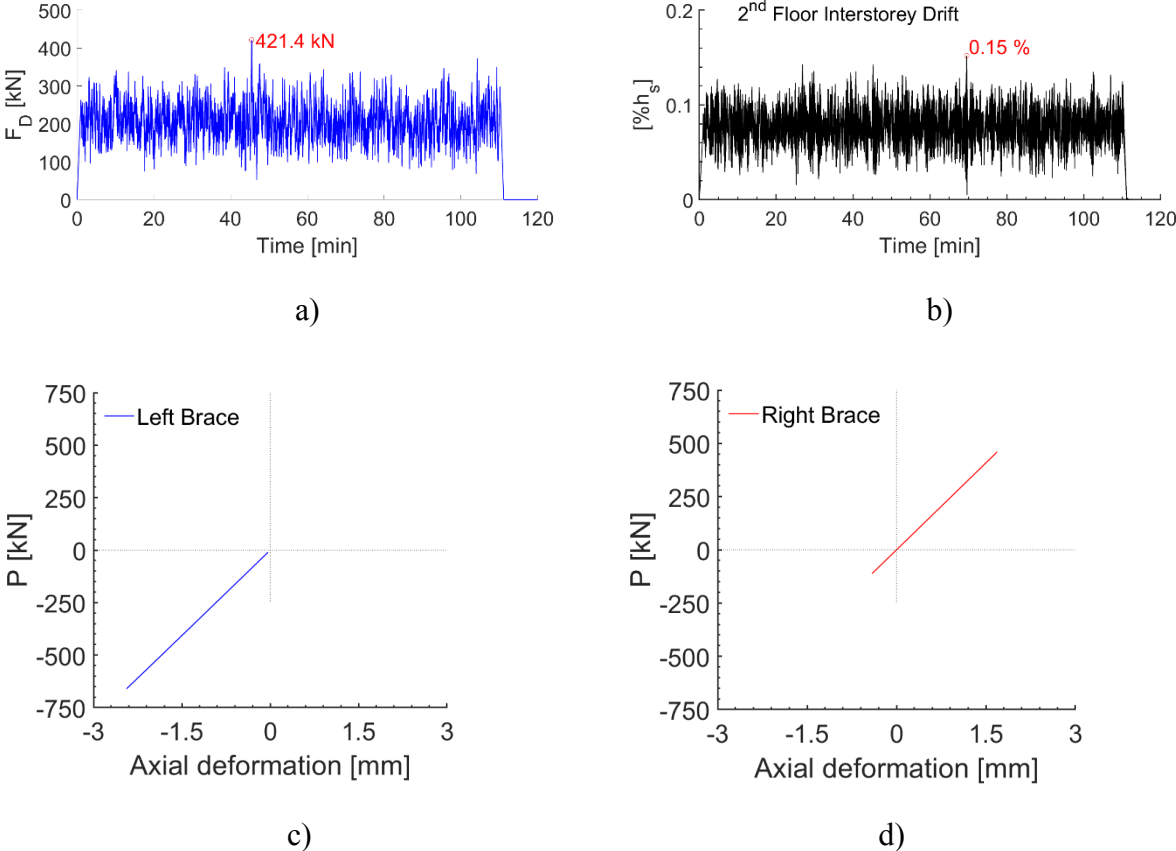


Fig. 5.9. Second storey response of the 16-storey LD-CBF building under Rand #5 realization, scaled to design level (*ULS*): a) 120 min. drag force history (Rand #5), b) time history of ISD and c)- d) hysteresis response of left and right HSS braces.

Note that the residual interstorey drift is not shown since the response is elastic and there is no permanent deformation under design wind loads.

5.1.2.1 Interstorey Drift (ISD) demand at SLS and ULS

The distribution of interstorey drift (ISD) along the height of the studied 12-storey and 16-storey buildings, subjected to the five wind realizations Rand #1 to Rand #5 is depicted in Fig. 5.10a and b, respectively.

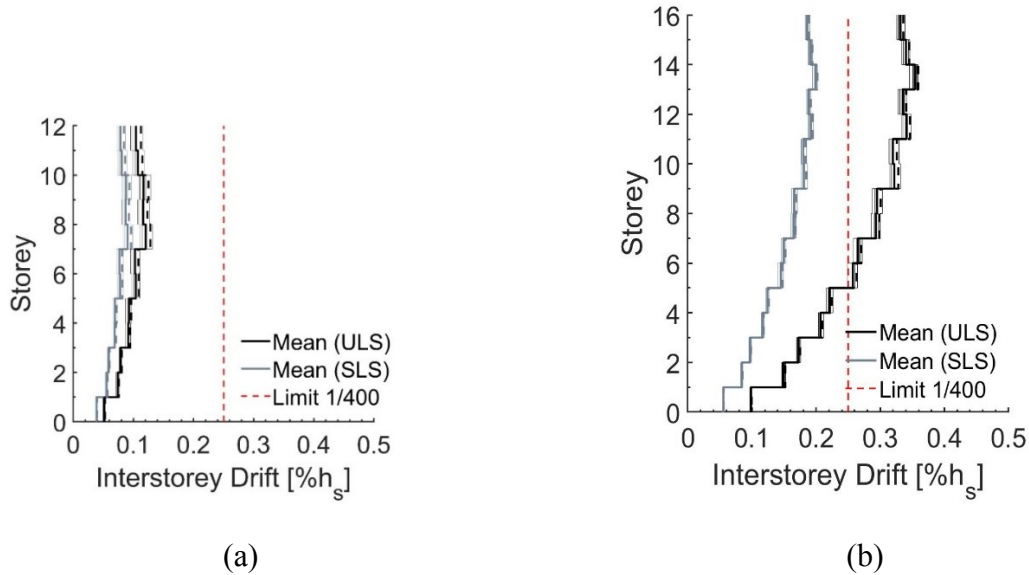


Fig. 5.10. Distribution of ISDs along the building height under wind Rand #1 - #5 at (SLS) and (ULS) for: a) 12-storey MD-CBF and b) 16-storey LD-CBF.

As observed from Fig. 5.10, for both buildings, the trend of the ISD response at the *SLS* is similar to that at increased demand (e.g. *ULS*). This is due to the elastic response that the buildings experience at the design level. The peak ISD (*SLS*) among floors increases as the height increases. Hence, in the case of 12-storey MD-CBF building, the peak ISD (*SLS*) occurs at the 8th and 10th floors but is still less than $0.1\%h_s$. The same trend is evident in the case of the 16-storey LD-CBF building, with the (*SLS*) drift increasing with the height and reaching its peak of ($0.2\%h_s$) at the 14th storey. Thus, both studied buildings experienced a peak ISD (*SLS*) which is within the code

limit of $0.25\%h_s$. In addition, the mean ISD computed from the five responses is calculated, as well as the mean plus one standard deviation ($mean + \sigma$). As illustrated, the peak among floors resulted from the maximum demand between Rand #1 and Rand #5 scaled for *SLS* is within the code limits ($0.25\%h_s$) for both buildings. The ISDs under wind demand scaled to *ULS* is illustrated to show the tendency of ISD distribution at increased demand.

5.1.2.2 Floor Accelerations (FAs) at SLS

The peak floor acceleration response of the studied 12-storey and 16-storey buildings, under the five wind realizations Rand #1 to Rand #5, scaled at SLS and ULS, is shown in Fig. 5.11a and b, respectively. Again, the FAs under wind demand scaled to *ULS* is illustrated to show the tendency of FA distribution at increased demand. As resulted, the peak floor acceleration among floors is within the habitability comfort level as per the PBWD prestandard (ASCE, 2019).

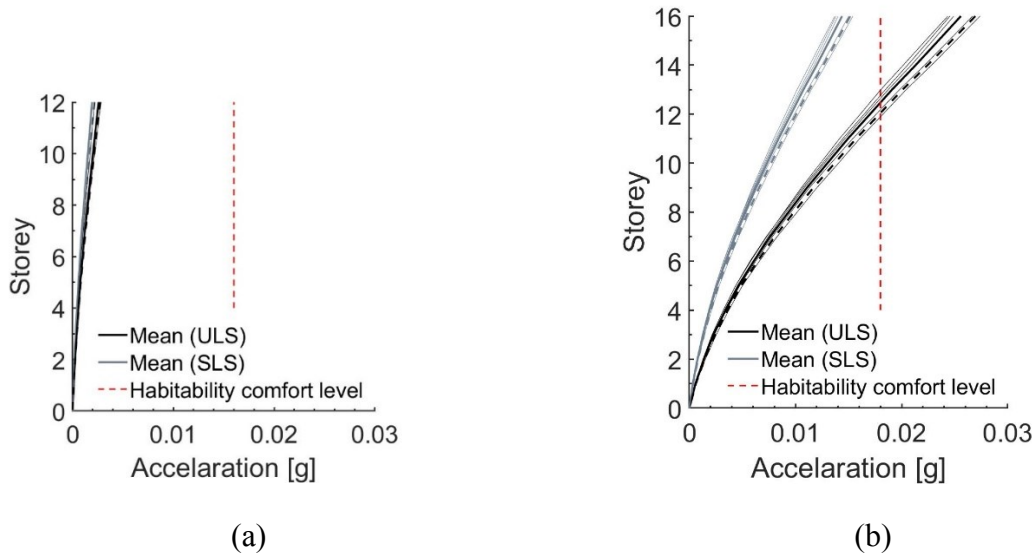


Fig. 5.11. Distribution of FAs along the building height under wind Rand #1 - #5 at (SLS) and (ULS) for: a) 12-storey MD-CBF and b) 16-storey LD-CBF.

Fig. 5.11 shows that taller buildings are more sensitive to wind developing higher FAs. Hence, occupants at the top floors experience the largest magnitude of floor acceleration due to the dynamic wind. In the case of the 16-storey LD-CBF building, the median acceleration at roof resulted under the serviceability limit state is equal to 14.4 milli-g, which is somewhat important but still less than the acceleration limit of 18 milli-g as per the ASCE PBWD pre-standard (ASCE, 2019). The peak FA among floors for the 12-storey MD-CBF building is significantly lower than that resulted for the 16-storey LD-CBF building, and is equal to 1.93 milli-g; hence, the 12-storey building satisfies the habitability comfort criteria threshold of 16 milli-g. Note that the occupant comfort criteria are harder to satisfy as the height of the building increases and may play a determinant role in the multihazard design of tall buildings.

5.2 Incremental Dynamic Analysis of Buildings under Seismic Loads

The IDA curves are computed for each studied building subjected to the same suite of seven artificial ground motions shown in Table 4.1. Each IDA curve relates the peak ISD among floors, obtained through the nonlinear response history analysis (*NRHA*), to seismic intensity, $S_a(T_1, 5\%)$, of selected ground motion that is incrementally scaled until the selected limit state is reached. Fig. 5.12a and b show the IDA curves for the 12-storey MD-CBF building and 16-storey LD-CBF building, respectively.

In Fig. 5.12, the IDA curve related to each individual ground motion is shown in gray, whereas the median curve representing the 50th percentile value for the seven ground motions is shown in red. As illustrated, each building exhibits a different response when subjected to the ground motion suite, resulting to a significant record-to-record variability. The gray circles indicate the building collapse, which, herein occurs due to the convergence issues during the nonlinear analysis.

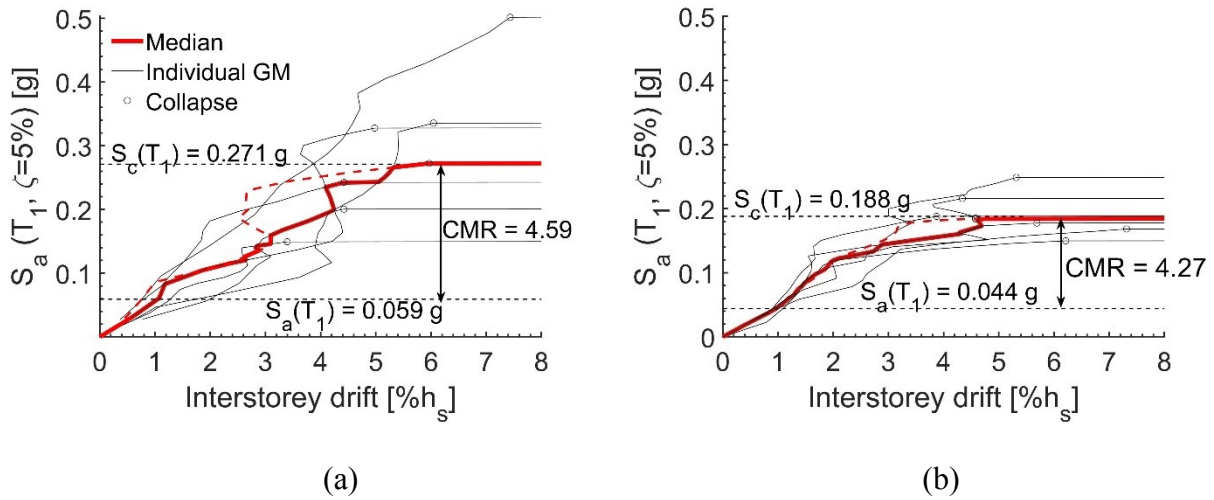


Fig. 5.12. IDA curves in terms of ISD resulted under the incremented GM suite: a) 12-storey MD-CBF building and b) 16-storey LD-CBF building.

Furthermore, the two horizontal dashed lines indicate the spectral ordinate at design level, $S_a(T_1)$, and the median collapse intensity, \hat{S}_{CT} , respectively. It is noted that the median collapse intensity is associated to the demand where half of the ground motions loaded the building to collapse (FEMA P695, 2009).

According to FEMA P58 (2012), a building is deemed to be repairable in the aftermath of an earthquake if the peak residual interstorey drift (RISD) among floors is less or equal to $0.5\% h_s$. To highlight the Reparability Limit State (RLS) associated to $0.5\% h_s$, a second EDP is selected as the RISD and the IDAs computed as a function of spectral acceleration intensity against RISD is shown in Fig. 5.13a and b for the 12-storey MD-CBF building and the 16-storey LD-CBF building, respectively.

As depicted in Fig. 5.13, in the case of 12-storey MD-CBF building, the RISD of $0.5\% h_s$ is associated with the median spectral intensity $S_a(T_1) = 0.174 g$. Under increased intensity, when $\text{RISD} = 1\% h_s$, the median spectral intensity slightly increases to $S_a(T_1) = 0.197 g$, i.e. an increase

of 13.2% in the Intensity Measure (IM). However, an increase of only 5.26% in the intensity measure, from 0.114 g to 0.12 g, is required to raise the median RISD from 0.5% h_s to 1% h_s for the 16-storey LD-CBF building. In general, both buildings start to accumulate larger damage for small increases in the spectral intensity demand.

The acceleration-sensitive components contribute also to the nonstructural loss. Thus, a third EDP as floor acceleration is considered to build the IDA curves for the studied buildings. The IDA curves associated with the floor acceleration (FAs) are illustrated for both studied buildings in Fig. 5.14a and b. As resulted, at median intensity associated to near collapse, the peak of median floor acceleration is below 1.4g.

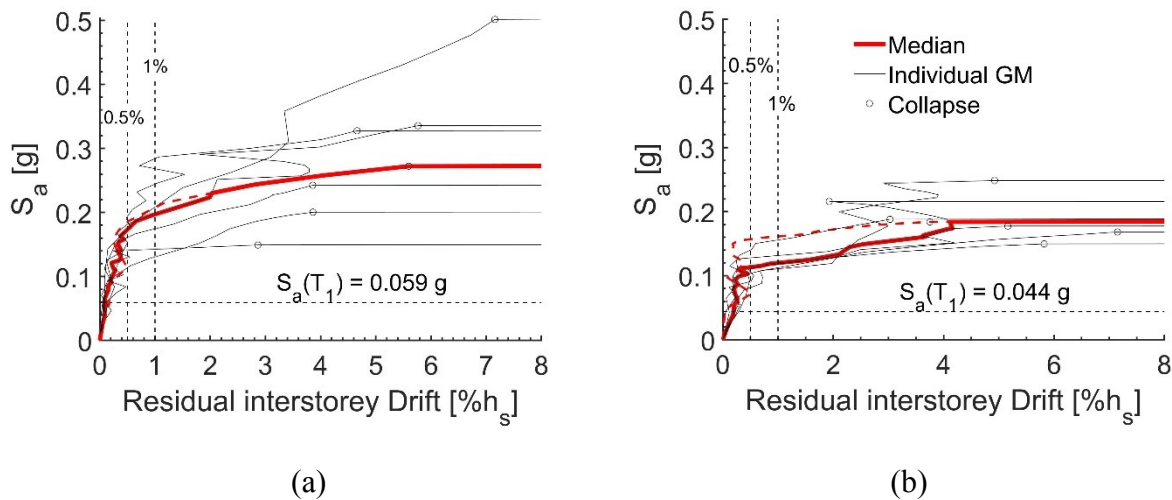


Fig. 5.13. IDA curves expressed in terms of RISD resulted under the incremented GM suite: a) 12-storey MD-CBF building and b) 16-storey LD-CBF building.

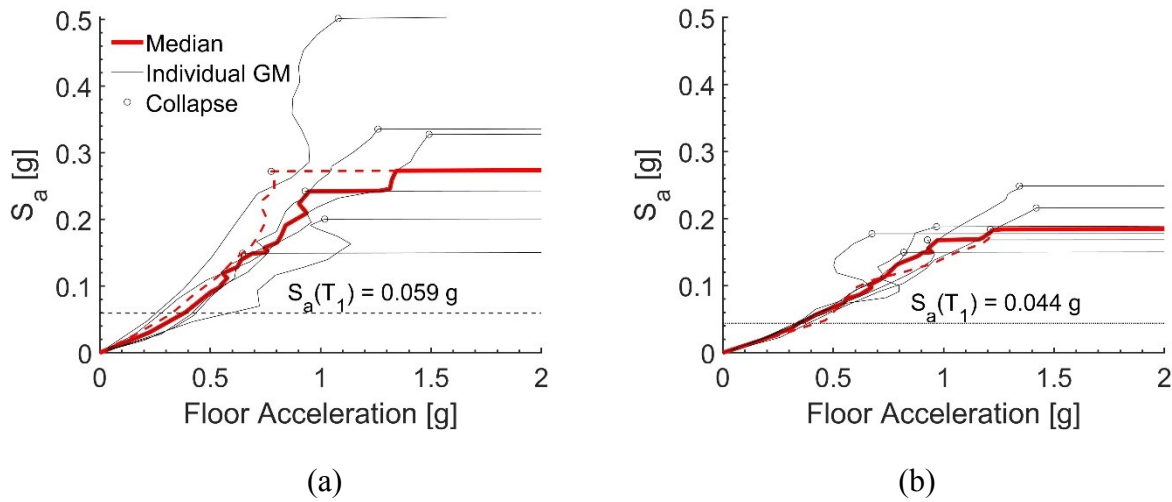


Fig. 5.14. IDA curves expressed in terms of FA resulted under the incremented GM suite: a) 12-storey MD-CBF building and b) 16-storey LD-CBF building.

The response of 12-storey and 16-storey buildings at increased demand, associated to a return period of 10000 years, or equivalent of 0.5% probability of exceedance in 50-years, is presented in terms of ISD, RISD, and FA in Fig. 5.15 and Fig. 5.16, respectively. This demand is equivalent to $2.4S_a(T_1)$. Thus, the distribution of the lateral ISD, RISD and FA over the height of the 12-storey MD-CBF building is illustrated below. As plotted in Fig. 5.15, the peak of mean ISD ($2.71\%h_s$) and the associated RISD ($0.24\%h_s$) is exhibited at the top floor. However, the peak of mean RISD of $0.47\%h_s$ is observed at the 1st and 2nd floors and is associated to a peak floor acceleration of $0.67g$ at the 1st floor.

For the 16-storey LD-CBF building, the distribution of the lateral ISD, RISD and FA over the height, associated with the $2.4S_a(T_1)$ demand, is shown in Fig. 5.16. Hence, the peak of mean ISD of $1.76\%h_s$ occurs at the 14th floor and the peak of mean RISD of $0.3\%h_s$ occurs at the 1st floors. In general, the 16-storey building exhibits slightly lower ISDs than the 12-storey building and the peak of mean RISD computed for both buildings is lower than the repairable limit of $0.5\%h_s$.

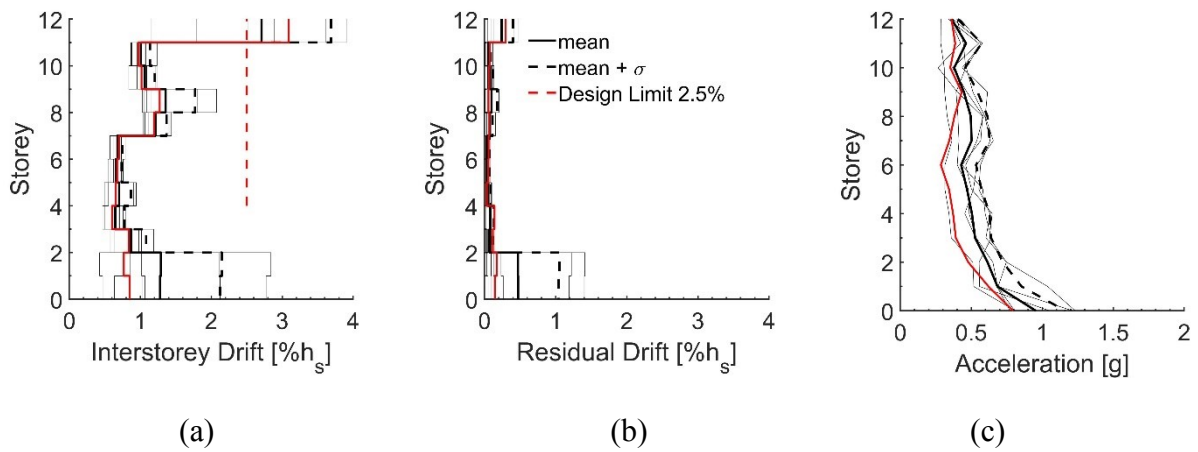


Fig. 5.15. Response of 12-storey MD-CBF building under the GM suite scaled to $2.4S_a(T_1)$: a) ISDs, b) RISDs and, c) FAs.

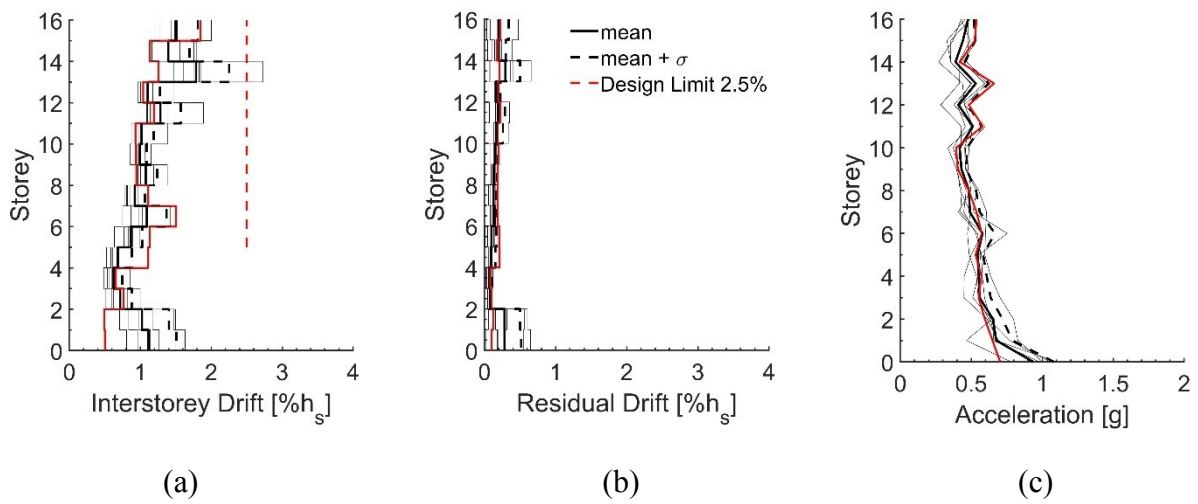


Fig. 5.16. Response of 16-storey LD-CBF building under the GM suite scaled to $2.4S_a(T_1)$: a) ISDs, b) RISDs and, c) FAs.

Fig. 5.17a, b and c show the deformed shape of the LFRS under the near collapse seismic intensity for the 12-storey MD-CBF and 16-storey LD-CBF buildings, respectively.

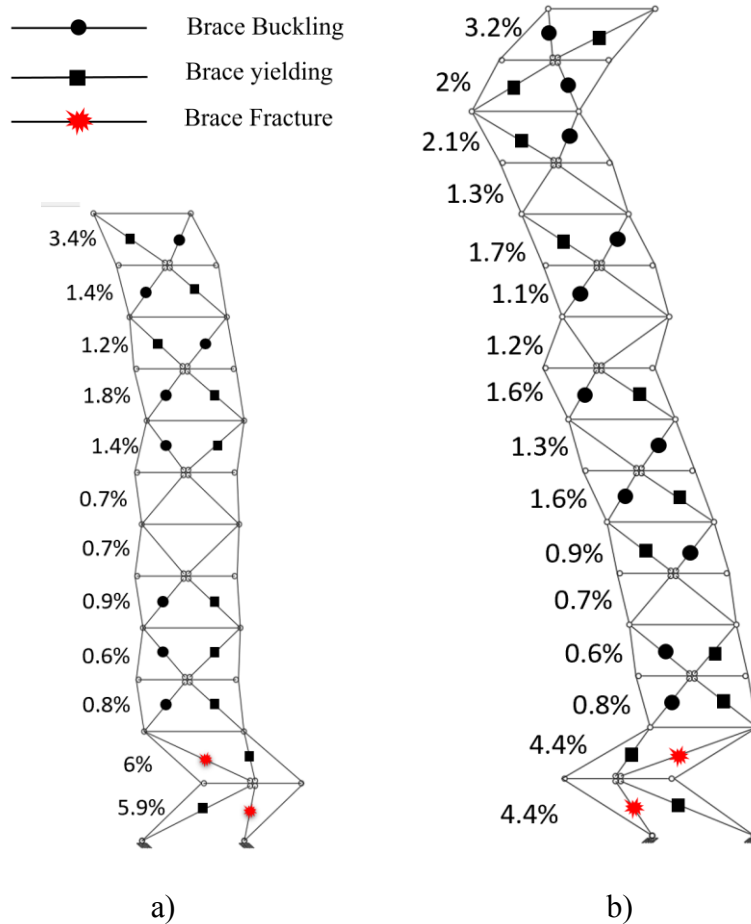
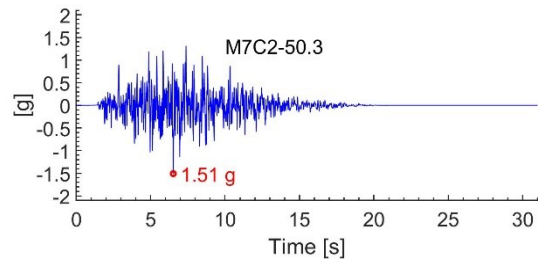


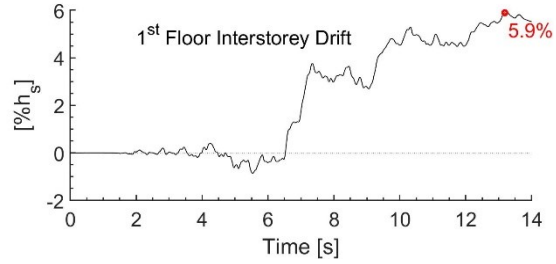
Fig. 5.17. Failure mechanism of buildings associated to Near Collapse limit state: a) 12-storey MD-CBF under M7C2_50.3 at $S_a(T_1) = 0.272g$ intensity and b) 16-storey LD-CBF buildings under M7C1_25.8 at $S_a(T_1) = 0.184g$ intensity.

Under the suite of ground motions, both studied buildings experienced two-storey failure mechanism of bottom floors followed by building collapse. Before the two-storey mechanism is formed at bottom floors, a large demand was induced at the top two floors.

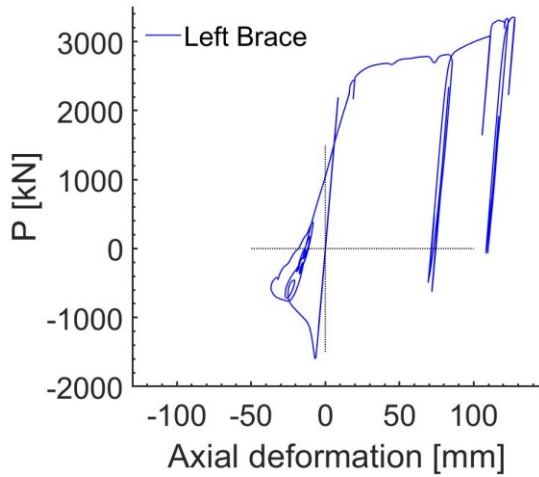
As shown in Fig. 5.18b, the 12-storey MD-CBF building experiences a maximum interstorey drift of 5.9% at the first floor under the M7C2_50_3 scaled to the near-collapse demand level. The hysteresis response of the 1st floor HSS braces show that the right brace reached the fracture failure due to low-cycle fatigue when reloaded in tension.



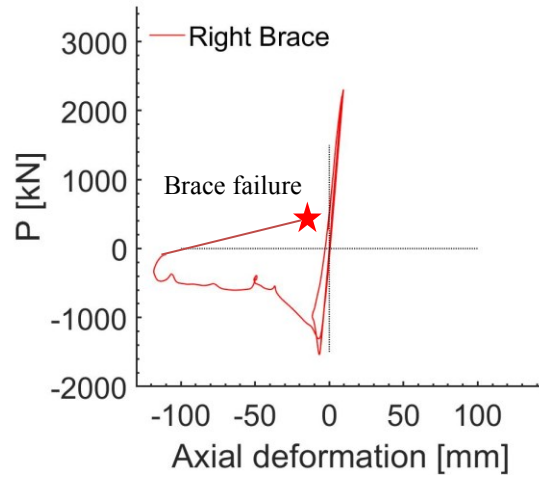
a)



b)



c)



d)

Fig. 5.18. Response of 12-storey MD-CBF building under M7C2_50_3 record scaled to near-collapse intensity: a) input ground acceleration, b) interstorey drift, c)-d) hysteresis response of the 1st floor left and right HSS braces.

The near-collapse response of 16-storey LD-CBF building is depicted under M7C1_25_8 record that is closed to the median demand (see Fig. 5.12 of IDA). As illustrated in Fig. 5.17 and Fig. 5.19b, the near-collapse mechanism is formed at bottom two floors where a maximum interstorey drift of $4.37\%h_s$ is recorded and the system is driven to collapse. The hysteresis response of the left and right HSS braces of 1st floor is plotted in Fig. 5.19 c and d. As depicted, when the right HSS brace is reloaded in tension, the fracture caused by low-cycle fatigue occurred.

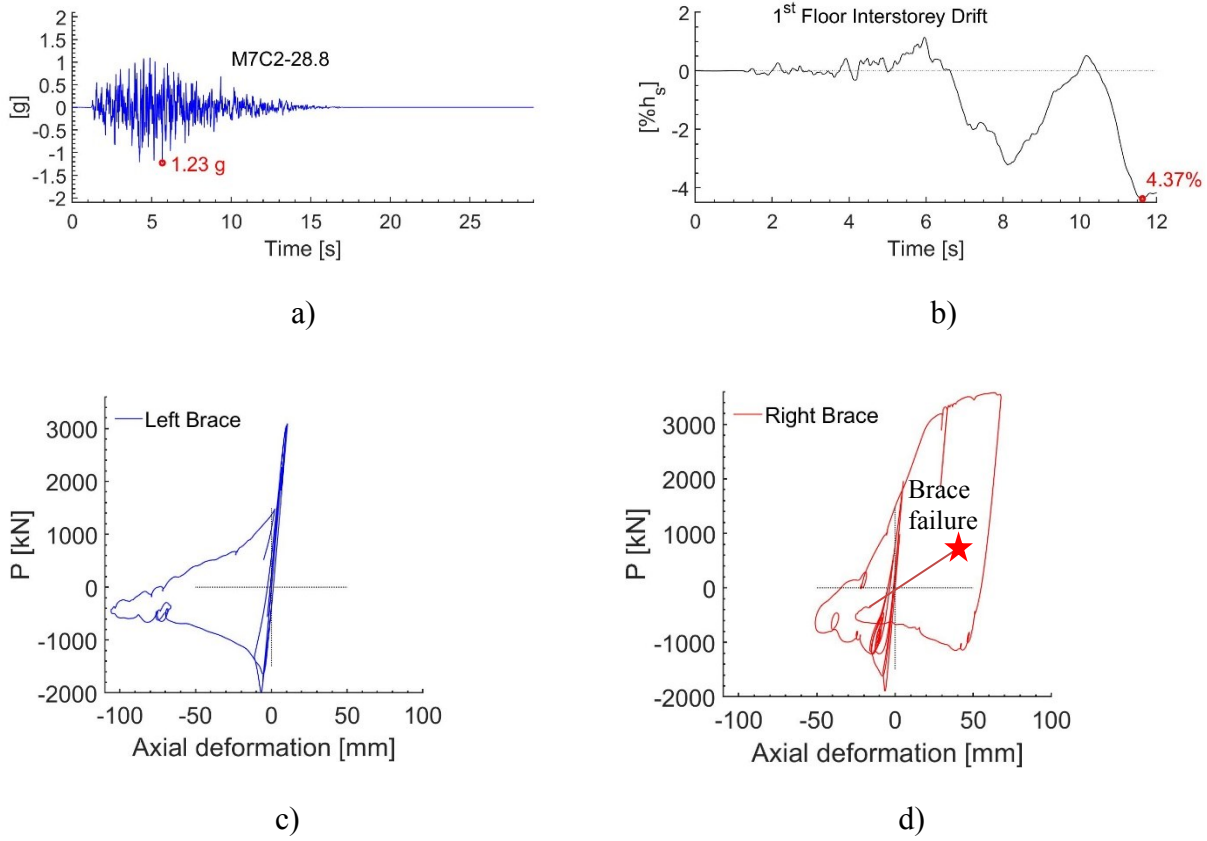


Fig. 5.19. Response of 16-storey LD-CBF building under M7C1_28_8 record scaled to near-collapse intensity: a) input ground acceleration, b) interstorey drift, c)-d) hysteresis response of the 1st floor left and right HSS braces.

5.3 Assessment of the Collapse Safety under Seismic Loads

To assess the collapse safety of studied buildings, the methodology provided in FEMA P695 (2009) is applied. Accordingly, the adjusted collapse margin ratio, ACMR, shall be bigger or equal to $ACMR_{10\%}$ ($ACMR \geq ACMR_{10\%}$), where $ACMR_{10\%}$ is the acceptable value of adjusted collapse margin ratio based on total system collapse uncertainty and value of acceptable collapse probability taken as 10%. The collapse margin ratio (CMR) is calculated as the ratio of the median collapse intensity to the spectral ordinate at design level, $S_a(T_1)$, as depicted in Fig. 5.12. The value of CMR is slightly smaller for the 16-storey LD-CBF building than that for 12-storey MD-CBF

building. However, for the 12-storey MD-CBF building same brace sections were increased to satisfy the elastic response of braces under wind demand at the design level. The adjusted collapse margin ration (ACMR) is calculated by amplifying the CMR by the spectral shape factor (SSF); hence, $ACMR = SSF \times CMR$. The SSF results from a Table from FEMA P695 as a function of period based-ductility μ and the building T_1 period. Herein, $\mu_T = \frac{\delta_u}{\delta_y}$, where δ_u is the roof interstorey drift at collapse and δ_y is the roof drift when the 1st brace experienced buckling. The CMR , $ACMR$ and SSF parameters are presented in Table 5.2. The calculation of the $ACMR_{10\%}$ resulted from a table from FEMA P695 and is a function of total uncertainty β_{TOT} calculated as per Eq. (2.41) in Chapter 2 and provided in Table 5.2. Accordingly, the sources of uncertainties are: record-to-record uncertainty, β_{RTR} , design requirements-related uncertainty, β_{DR} , test data-related uncertainty β_{TD} , and modeling uncertainty, β_{MDL} . For the purpose of assessing β_{TOT} , the test data is categorized as Good ($\beta_{TD} = 0.2$), the design requirements-related uncertainty is categorized as superior ($\beta_{DR} = 0.1$), and the modeling uncertainty is categorized as good ($\beta_{MDL} = 0.2$).

The record-to-record uncertainty computed for the 12-storey MB-CBF and 16-storey LD-CBF building is: $\beta_{RTR} = 0.3915$ and 0.166 , respectively. The total system collapse uncertainties for the 12-story MD-CBF and 16-storey LD-CBF buildings are calculated from Eq. (2.41) in Chapter 2, and are equal to 0.493 and 0.343 .

Table 5.2. Parameters for collapse safety verification of studied buildings under seismic GMs

Parameter	12-storey	16-storey
	MD-CBF	LD-CBF
$S_a(T_1)$	0.0593g	0.044g
\hat{S}_{CT}	0.2715g	0.184g
CMR	4.58	4.27
SSF	1.21	1.305
$ACMR = CMR \times SSF$	6.45	5.57
β_{TOT}	0.493	0.343
$ACMR_{10\%}$	1.705	1.556
$ACMR > ACMR_{10\%}$	OK	OK

The fragility curves of studied buildings obtained under the ground motion suite scaled to near collapse intensity are computed and adjusted to account for the effect of total uncertainty. These fragility curves at near collapse are shown in Fig. 5.20.

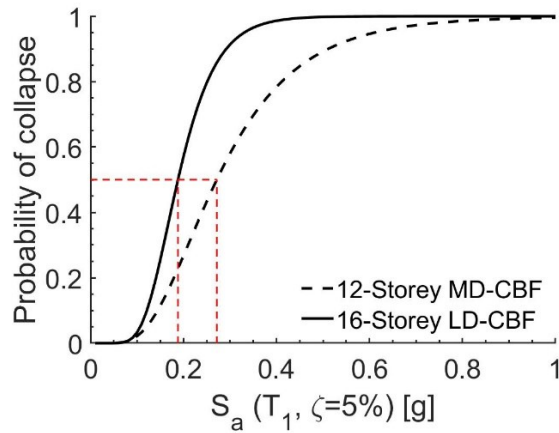


Fig. 5.20. Seismic fragility curves at near collapse for the 12-storey MD-CBF and 16-storey LD-CBF buildings.

As shown in Table 5.2, all the archetype buildings pass the acceptance criteria of the adjusted collapse margin ratio: $ACMR \geq ACMR_{10\%}$ as per FEMA P695 (2009).

A summary of seismic demand in terms of the median ISD, median RISD and median FA at and beyond the design level is provided in Table 5.3.

Table 5.3. Summary of seismic demand and response parameters at and beyond design level.

Earthquake Hazard		12-storey MD-CBF			16-storey LD-CBF		
Spectral Acc.	Return Period (prob. of exceedance)	Median ISD	Median RISD	Median FA	Median ISD	Median RISD	Median FA
		[%h _s]	[%h _s]	[g]	[%h _s]	[%h _s]	[g]
$S_a(T_1)$	2475 yrs. (2%/50yrs.)	1.05	0.11	0.38	0.96	0.20	0.34
~ 1.5x $S_a(T_1)$	5000 yrs. (1%/50yrs.)	1.37	0.19	0.49	1.29	0.26	0.49
~ 2x $S_a(T_1)$	7500 yrs. (0.75%/50yrs.)	2.55	0.22	0.56	1.54	0.26	0.63
~ 2.4x $S_a(T_1)$	10000 yrs. (0.5%/50yrs.)	2.84	0.38	0.66	1.85	0.39	0.70

5.4 Incremental Dynamic Analysis under Wind Loads

The incremental dynamic analysis (IDA) curves are built for one suite of selected random events (Rand #1 - Rand #5), provided in Chapter 4. Herein, the IDA curves relate the peak interstorey drift among floors obtained through NRHA to incremented wind intensity V_{10} , where V_{10} is the hourly mean wind velocity at 10 m height, which is 29.6 m/s at design level (1 in 500 years). Hence, wind intensity data are expressed as the mean hourly wind speed, at 10 meters height ($V_{10/n}$),

and have a 1-in- n -years chance of being exceeded in any year; $V_{1/n}$ can be evaluated using the following equation available at NBC, Appendix C:

$$V_{1/n} = \frac{1}{1.4565} \left\{ V_{1/50} + 0.4565 V_{1/10} + \frac{V_{1/50} - V_{1/10}}{1.1339} * \ln \frac{-0.0339}{\ln(1 - 1/n)} \right\} \quad 5.1$$

Thus, for Montreal, the 1-in-10, the 1-in-50 years and 1-in-500 years wind speeds is equal to $V_{1/10} = 22.6 \text{ m/s}$; $V_{1/50} = 25.5 \text{ m/s}$ and $V_{1/500} = 29.6 \text{ m/s}$, respectively. The corresponding wind pressure “ q ” in kPa can be obtained easily from the wind speed, as $q = \frac{1}{2} \rho V^2 / 1000$, where $\rho = 1.2929 \text{ kg/m}^3$ is the air density and V is provided in m/s.

Fig. 5.21a and b show the wind IDA curves for the 12-storey MD-CBF building and 16-storey LD-CBF building, respectively.

As illustrated in Fig. 5.21, the IDA curve for each individual wind realization is shown in gray, whereas the median curve representing the 50th percentile value for all the five random winds is shown in black. As depicted, the IDA curves for the five winds are remarkably similar and the waving behavior of the buildings that was exhibited under seismic load does not occur under dynamic wind loading. The wind response at the design level ($V_{1-in-500 \text{ years}} = 29.6 \text{ m/s}$) is elastic for both buildings. This type of elastic response continues until the buildings start to exhibit a nonlinear behavior at $V_{yield} = 49.7 \text{ m/s}$ and 43.1 m/s for the 12-storey MD-CBF and 16-storey LD-CBF building, respectively. Then, an accelerated development in the lateral interstorey drift of 12-storey MD-CBF and 16-storey LD-CBF building occurs before reaching the collapse point at the median wind speed $V_C = 58.2 \text{ m/s}$ and 49.04 m/s , respectively. The associated collapse margin ratios computed as V_C over $V_{1-in-500 \text{ years}}$ are $CMR = 2.58$ and 2.17 for the 12-storey MD-CBF and 16-storey LD-CBF buildings, respectively. The value of CMR would be smaller for the

12-storey MD-CBF building if the sections had not been increased to assure elastic response under wind demand.

It is worth noting that NBC (2015) checked for the interstorey drift under the effect of service wind loads (0.75W) in which it corresponds to a return period equal to 10 years.

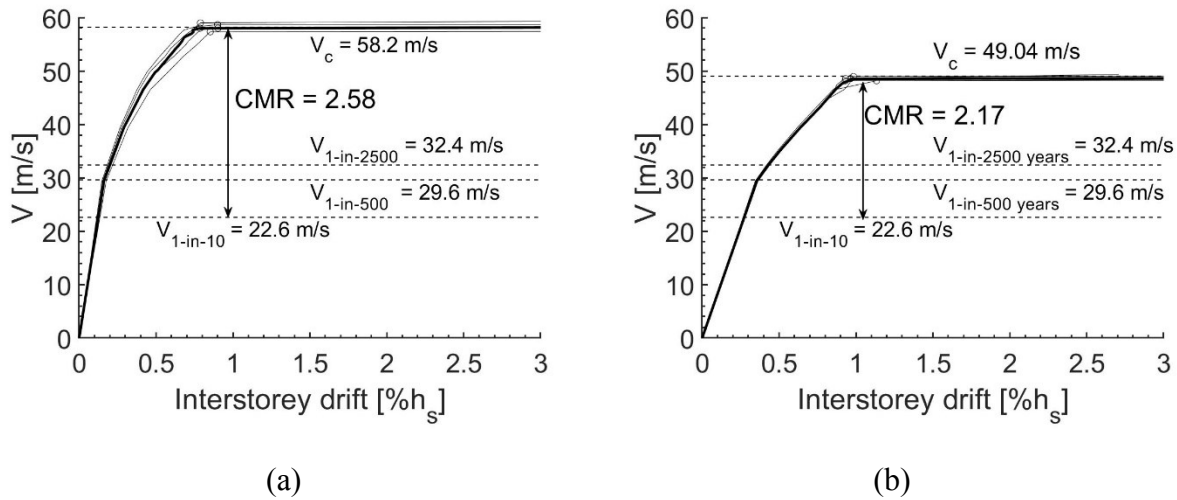


Fig. 5.21. IDA curves in term of ISD under Rand #1 - #5 wind: a) 12-storey MD-CBF building, and b) 16-storey LD-CBF buildings.

The incremental dynamic analysis (IDA) curves, expressed in terms of a second EDP as residual interstorey drift (RISD), that resulted under the five wind realizations, Rand #1 - #5, are shown in Fig. 5.22a and b for the 12-storey MD-CBF and 16-storey LD-CBF buildings, respectively. Under the design wind level with a reference wind velocity $V_{1-in-500yrs} = 29.6 \text{ m/s}$, the response is elastic and there is no permanent deformation. As illustrated, the buildings remain in the elastic range of response for winds with a return period of 2500 years, $V_{1-in-2500yrs} = 32.4 \text{ m/s}$.

It is worth noting that the reference 1-in-50 years wind velocity for Montreal, $V = 25.5 \text{ m/s}$, is about 79% of the associated 1in-2500 years wind velocity (or 62% in terms of wind pressure q),

while the intensity of an earthquake with a return period of 50 years is approximately 15% of the intensity based on a return period of 2500 years (NBC Structural Commentary, 2015).

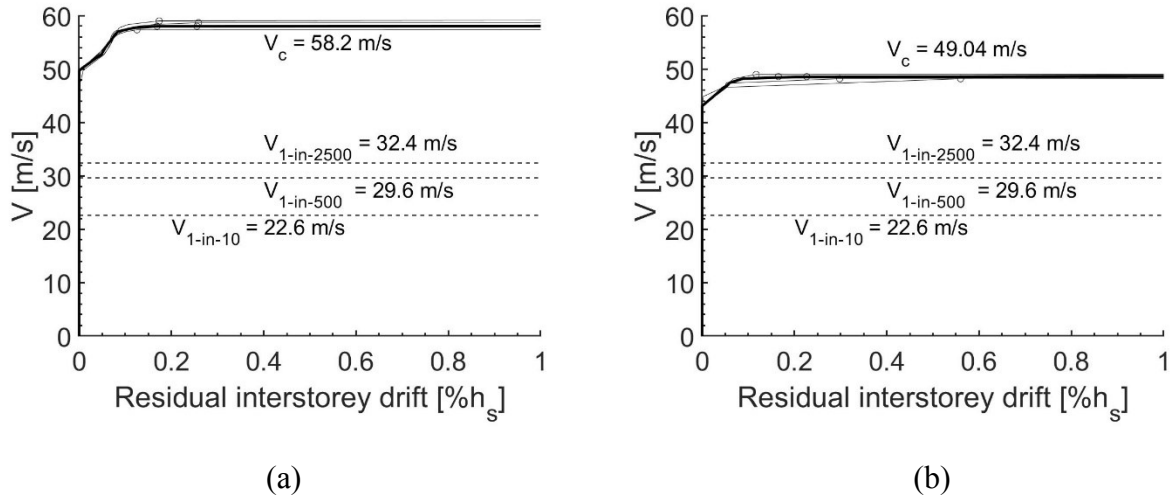


Fig. 5.22. IDA curves in term of RISD under Rand #1 - #5 wind: a) 12-storey MD-CBF building and, b) 16-storey LD-CBF building.

Thus, Fig. 5.22 shows that a significant increase of the wind speed (e.g. $V_{yield} \sim 50\text{m/s}$ for the 12-story buildings and $V_{yield} \sim 43\text{m/s}$ for the 16-story building) is requested in order to generate a nonlinear response of buildings. Furthermore, the incremental dynamic analysis (IDA) curves associated with the floor acceleration (FAs) are illustrated in Fig. 5.23a and b for both buildings, respectively.

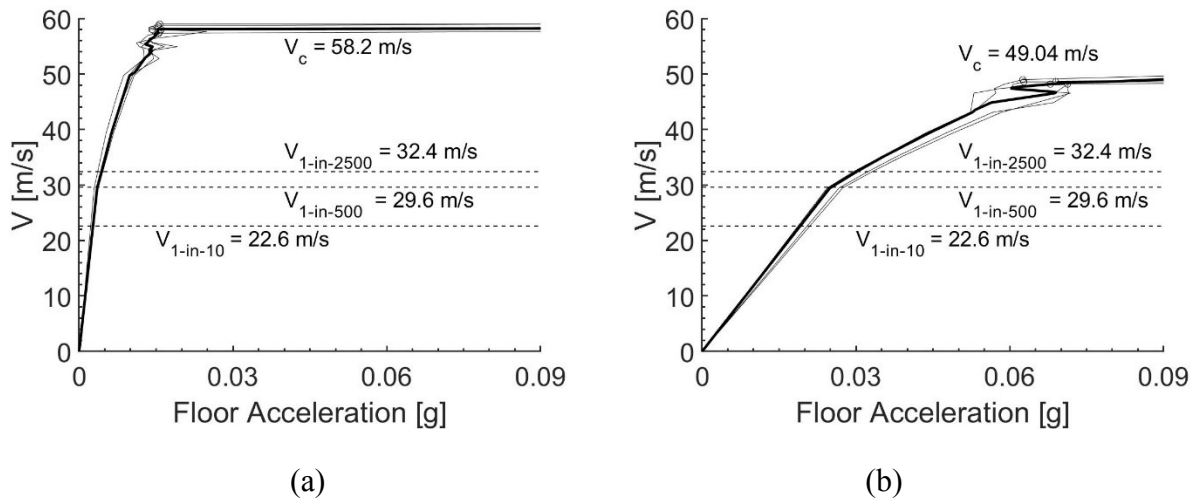


Fig. 5.23. IDA curves in terms of FAs under Rand #1 - #5: a) 12-storey MD-CBF building and, b) 16-storey LD-CBF building.

Note that the FAs are sensitive to the height and the 16-storey building experienced a higher demand of FAs than the 12-storey building. However, the two buildings do not exhibit large floor accelerations under the different wind intensities; hence, at design level, they satisfy the habitability comfort criteria, 16 milli-g and 18 milli-g, for the 12-storey MD-CBF and the 16-storey buildings LD-CBF, respectively (ASCE PBWD pre-standard, 2009).

Fig. 5.24 illustrates the distribution of ISD, RISD and FAs along the height of 12-storey MD-CBF building subjected to Rand #1- #5 winds scaled to $V_c = 58.67$ m/s which is associated to the near-collapse response resulted under Rand #3 ($V_{c, \#3} = 58.67$ m/s).

As depicted in Fig. 5.24, the peak of mean ISD of $0.82\%h_s$ and the peak of mean RISD of $0.2\%h_s$ occur at the third floor, where the C_f/C_r ratio for the selected brace section is slightly above 1. The associated mean FA is 0.011g and the peak of mean FA occurs at the top floor. It is noteworthy that at the nearest collapse point, the peak residual interstorey drift among floors is within the repairable limit of $0.5\%h_s$, which means that the building is still repairable.

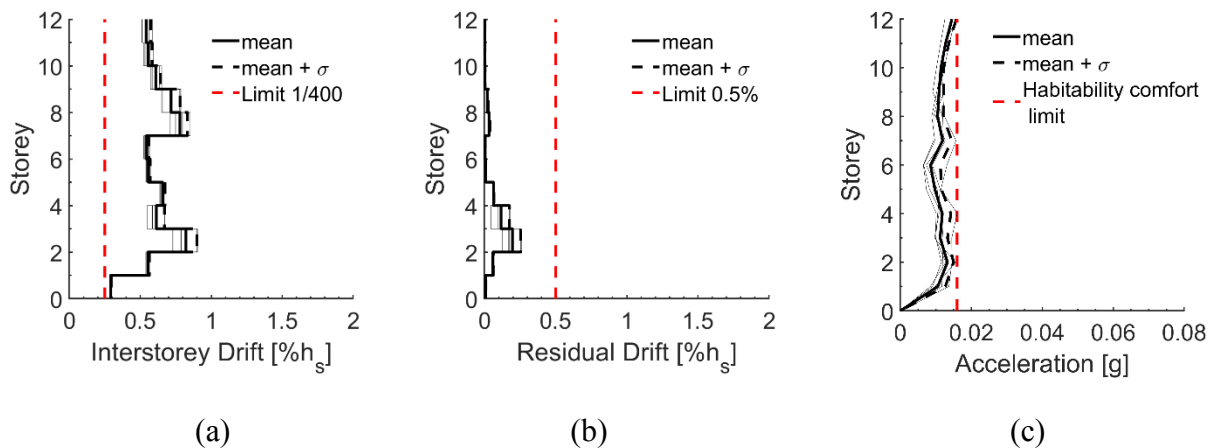


Fig. 5.24. Distribution of EDPs along the height of 12-storey MD-CBF building subjected to Rand #1-#5 winds scaled to $V_C = 58.67$ m/s (note that $V_C = V_{C, \#3} = 58.67$ m/s means the near-collapse limit state under Rand #3): a) ISD, b) RISD and c) FA.

Regarding the 16-storey LD-CBF building response at near collapse, in Fig. 5.25 is shown that the peak of mean ISD of $0.94\%h_s$ occurs at the 14th floor followed by the 7th floor and the peak of mean RISD of $0.27\%h_s$ exhibited at the bottom floor followed by the 7th floor. The peak of mean FA is recorded at the top floor and is about 0.07g.

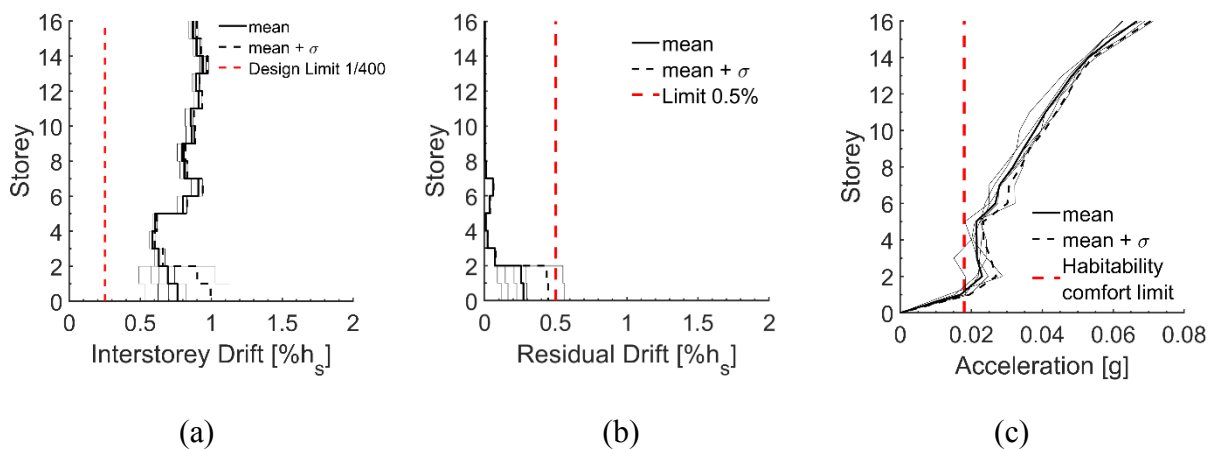


Fig. 5.25. Distribution of EDPs along the height of 16-storey LD-CBF building subjected to Rand #1-#5 winds scaled to $V_C = 58.67$ m/s (note that $V_C = V_{C, \#3} = 58.67$ m/s is the near-collapse limit state under Rand #3): a) interstorey drift, b) residual drift and c) floor acceleration.

Fig. 5.26a and b show the deformed shape of the LFRS of studied buildings under wind at near-collapse demand. The largest deformation of 12-storey MD-CBF building and 16-storey LD-CBF building was observed under wind Rand #3 demand and wind Rand #5, respectively.

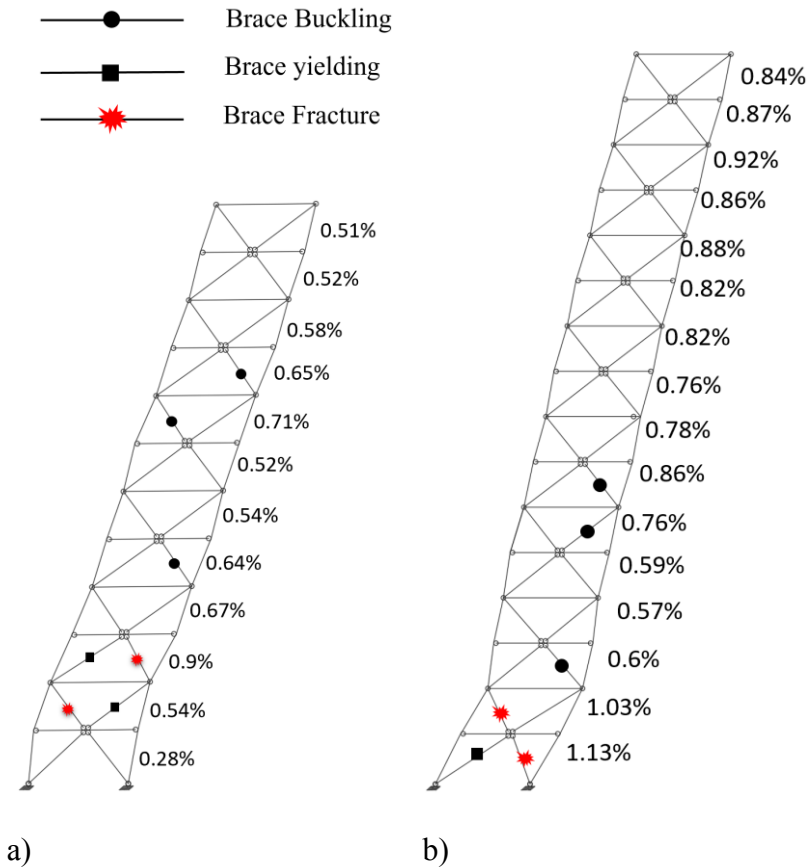


Fig. 5.26. Failure mechanism of buildings associated to near collapse: a) 12-storey MD-CBF under wind Rand #3 and b) 16-storey LD-CBF under wind Rand #5

The deformed shapes illustrated in Fig. 5.26a and b under wind loads follow the first mode shape and is characterized by the accumulation of the plastic deformations in the bottom part that are also augmented by the P- Δ effect.

Fig. 5.27 shows the near-collapse response of the 3rd floor of 12-storey MD-CBF building under the wind Rand #3 realization. Although a relatively small peak ISD of 0.9% h_s was reached at the

third-floor level, the strain in braces is accumulated due to several cycles spread over 120 min. As depicted in in Fig. 5.27b, a jump in the time history of ISD series of 3rd floor that occurred at $t = 40$ min. The jump in drift is caused by the buckling of right brace, while the failure is experienced at $t = 106$ min. The hysteresis response of the third-floor braces is shown in Fig. 5.27c and d.

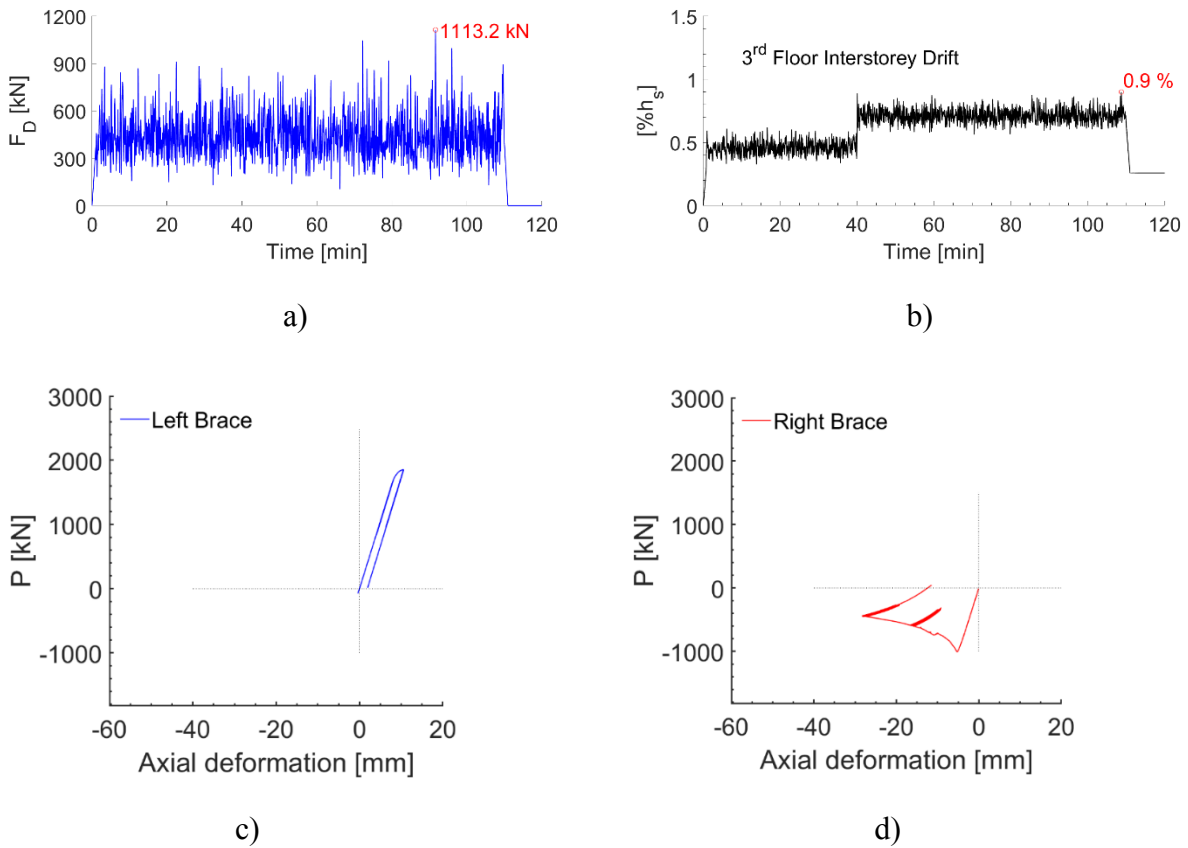


Fig. 5.27. Response of the 3rd floor of 12-story MD-CBF building under Rand #3 realization scaled to near collapse intensity: a) time history drag force at 3rd floor, b) time history ISD and c)-d) hysteresis behaviour of the left and right HSS braces.

The taller building is more sensitive to wind and experienced large wind demand in terms of ISD and hysteresis experienced by braces, etc. In particular, the wind-induced peak interstorey drift of the 16-storey LD-CBF building is approximately 1.6 and 1.8 times the corresponding values of the

12-storey MD-CBF building. Fig. 5.28 shows the near-collapse response of 1st floor of 16-storey LD-CBF building under the wind Rand #5 realization.

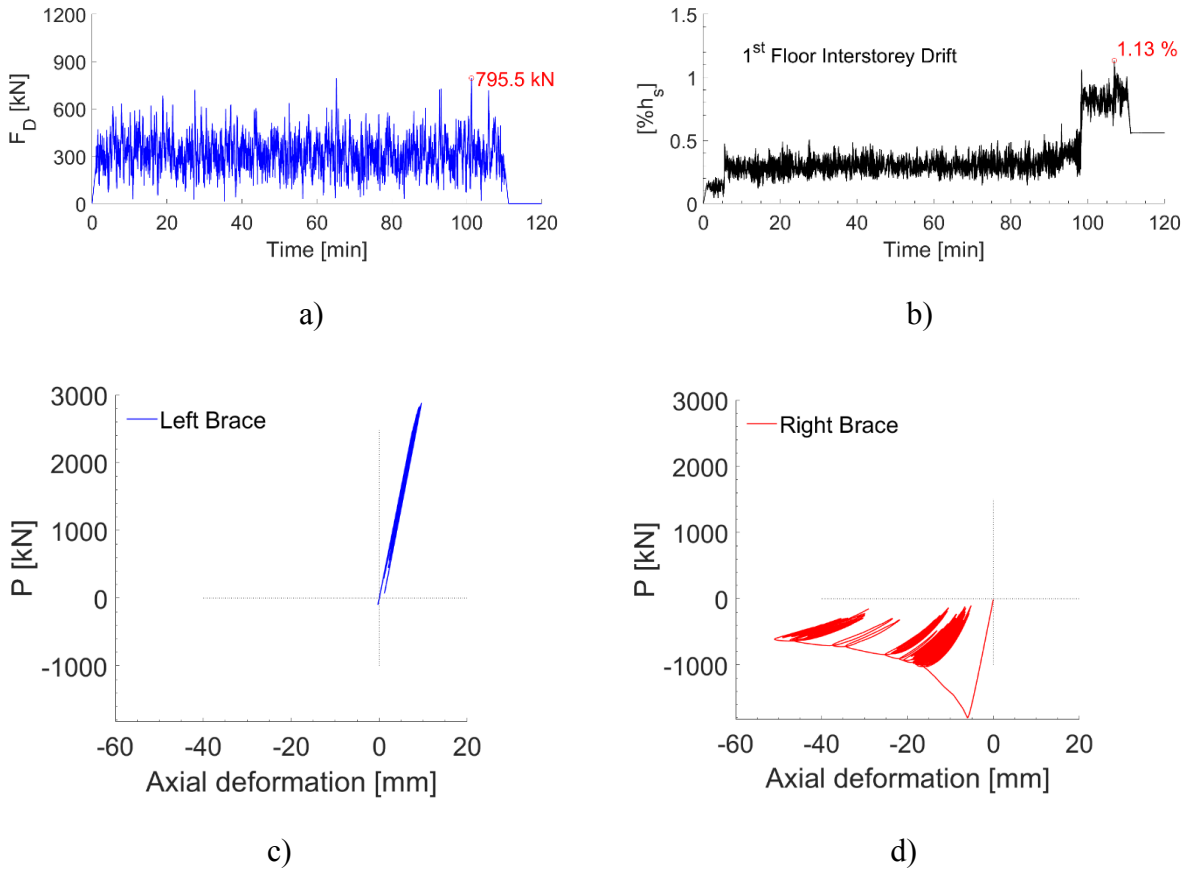


Fig. 5.28. Response of the 1st floor of 16-storey LD-CBF building under Rand #5 realization scaled to the near collapse intensity: a) time history drag force at 1st floor, b) time history ISD, and c)-d) hysteresis behaviour of the left and right braces.

As depicted in Fig. 5.28b, a jump in the time history ISD series of 1st floor is recorded at $t = 100$ min. and the failure is experienced at $t = 110$ min. The hysteresis response of the third-floor braces is shown in Fig. 5.28c and d.

A summary of the wind demand in terms of median ISD, median RISD, and median FA is provided in Table 5.4 at and beyond the design level.

Table 5.4. Summary of wind demand and response parameters at and beyond design level.

Wind Hazard		12-storey MD-CBF			16-storey LD-CBF		
Wind Speed V_{10}	Return Period (prob. Of exceedance in 50 years)	Median ISD	Median FA	Habitability comfort L.S.	Median ISD	Median FA	Habitability comfort L.S.
[m/s]		[%h _s]	[milli-g]	[milli-g]	[%h _s]	[milli-g]	[milli-g]
22.6	10 yrs.	0.12	2.70	16	0.27	19.12	18
25.5	50 yrs.	0.14	3.04		0.31	21.57	
29.6	500 yrs. (10%/50yrs)	0.16	3.56		0.36	25.20	
32.4	25000 yrs. (2%/50yrs)	0.20	4.35		0.43	30.15	
33.6	5000 yrs. (1%/50yrs)	0.22	4.69		0.46	32.45	
46.5(1 st yield)	7,900*10 ³ yrs. (0.00063%/50yrs)	-	-		0.87	68.49	
49.8(1 st yield)	50,657*10 ³ yrs. (0.0001%/50yrs)	0.50	9.95		-	-	

5.5 Wind Assessment

The collapse fragility curve of the studied buildings under the considered random wind realizations are shown in Fig. 5.29. The record-to-record uncertainty is equal to $\beta_T = 0.0111$ for the 12-storey MD-CBF building and $\beta_T = 0.0036$ for the 16-storey LD-CBF building, respectively. The dispersion used to construct the fragility curve is increased from its initial value to $\beta = (\beta_T^2 + \beta_f^2 + \beta_m^2)^{1/2} \sim 0.16$ for both buildings. Herein, according to ASCE 2019, Appendix B.2, the uncertainties concerning the quality and completeness of the model is $\beta_m = 0.10$ and the uncertainty in the collapse mode capacity is $\beta_f = 0.12$.

The reliability criterion defined in the PBWD prestandard (ASCE, 2019) requires that the design velocity ($V_{1/500}$) is greater than the velocity at which there is a 0.01% conditional probability of failure ($V_{0.01\%}$). The reliability criterion is satisfied, since $V_{1/500} = 29.6$ m/s $>$ $V_{0.01\%} = 28.95$ and 24.41 m/s respectively for the 12-storey MD-CBF and 16-storey LD-CBF buildings. The $V_{0.01\%}$ values can be easily retrieved from the collapse fragility curves of Fig. 5.29. Thus, the building heads to collapse without taking advantage of the system ductility and overstrength under wind load.

However, a direct comparison of the safety margin resulted under wind and seismic loads is not reasonable due to the different nature of the two hazards and in particular the different return periods of winds and earthquakes. A summary of the total system collapse uncertainty and the collapse margin ratio under wind load is provided for both buildings in Table 5.5.

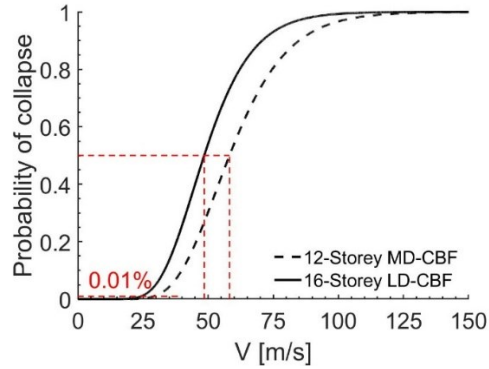


Fig. 5.29. Wind collapse fragility curves for the 12-storey MD-CBF and the 16-storey LD-CBF buildings.

Table 5.5. Total system collapse uncertainty and reliability criterion evaluation as per PBWD pre-standard (ASCE, 2019) under wind loads.

Parameter	12-st. MD-CBF	16-st. LD-CBF
V_{design}	29.6	29.6
\hat{V}_C	58.2	49.04
CMR	2.58	2.17
β_{TOT}	0.16	0.16
$V_{0.01\%}$	29.3	24.4
$V_{1/500} > V_{0.01\%}$	OK	OK

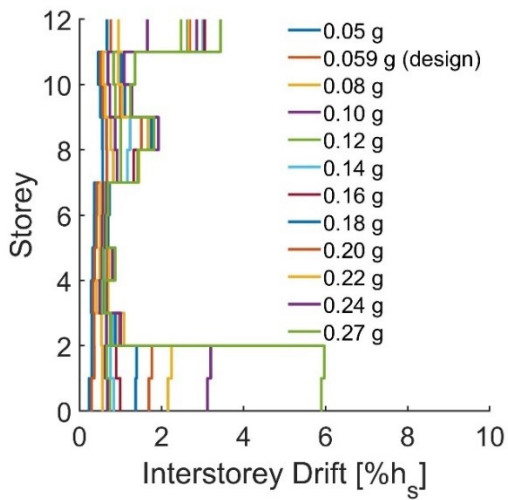
5.6 Comparison of buildings response under Wind and Earthquake

To provide insights in the development of the collapse mechanisms illustrated in Fig. 5.17 (earthquake) and Fig. 5.26 (wind), the progressive development of peak interstorey drift under incremented intensity of earthquake and wind is presented for the 12-storey and 16-storey buildings in Fig. 5.30a-b and c-d, respectively. For the 12-storey MD-CBF building, the

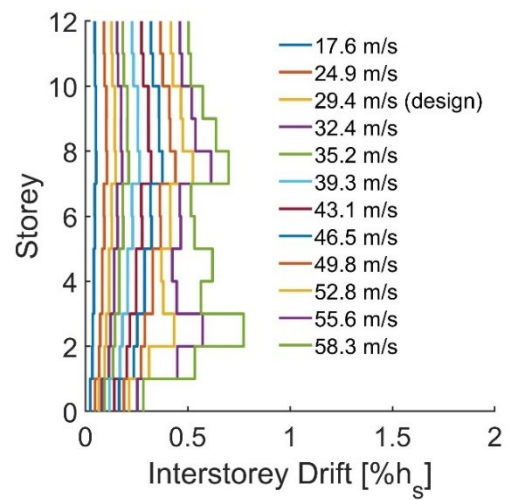
exemplification is illustrated under M7C2_50.3 record and Rand #3 realization wind. For the 16-storey LD-CBF building, the exemplification is illustrated under M7C1_25.8 record and Rand #5 realization wind. Note that the selected records and wind realizations are nearest the median response, as shown from IDA curves.

At the design level ($S_a = 0.059 g$) and up to intensities 3.7 times the design intensity ($S_a = 0.22 g$), the 12-storey MD-CBF building exhibits nonlinear response under the M7C2_50.3 ground motion and the damage is concentrated in the 9th floor and top floor. With the increasing seismic demand, a larger interstorey drift demand occurs in the lower two floors leading to excessive damage and potential failure. The same response is noticed for the 16-storey LD-CBF building, where a sudden increase of the interstorey drift was observed under $S_a = 0.16g$ (3.6 times the design level) intensity. The peak ISDs is concentrated at the lower floors which triggers failure and the near-collapse state.

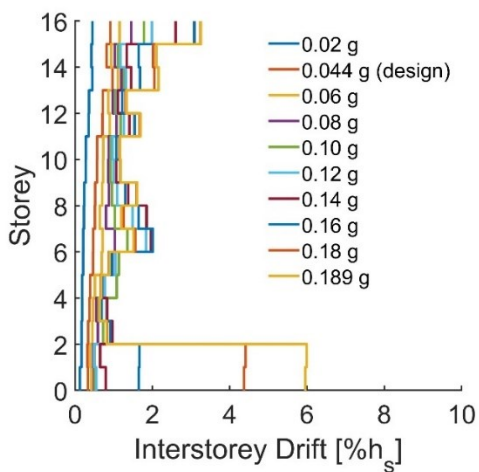
However, conservative wind design leads to linear response following the first mode pattern response. Nonlinearity occurs at higher levels of wind excitations, and the collapse is triggered at the bottom floors under $V = 58.3$ and $48.6 m/s$ for the 12-storey MD-CBF building and the 16-storey LD-CBF building respectively. It is worth mentioning that failure caused by wind occurs for much smaller interstorey drifts ($< 1\%h_s$) when compared to the drift triggered by seismic GMs. Similar conclusions can be drawn for the 16-storey building under the Rand #5 wind.



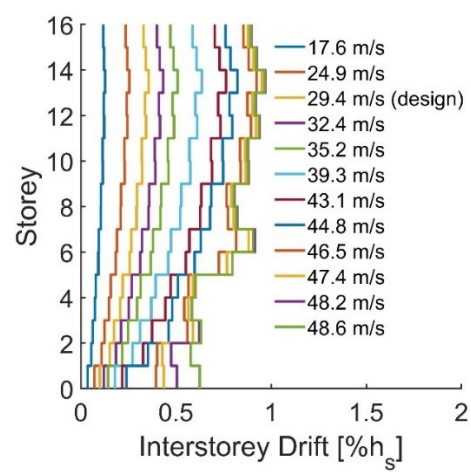
(a)



(b)



(c)



(d)

Fig. 5.30. Progressive development of peak interstorey drift under earthquake and wind incremented intensity for the 12- and 16-storey buildings under: a)-b) M7C2_50.3 and wind Rand #3 for 12-st MD-CBF and, c)-d) M7C1_25.8 and wind Rand #5 for 16-st LD-CBF building.

6. CHAPTER 6. CONCLUSIONS AND FUTURE WORK

6.1 Conclusions

This study was conducted to evaluate the wind and earthquake nonlinear dynamic performance of two archetype office buildings, located in Montreal, Canada. The buildings share the same floor plan and are equipped with four concentrically braced frames (CBFs) in each orthogonal direction to resist the lateral actions, moderate-ductility CBFs (MD-CBF) for the 12-storey building and limited-ductility CBFs (LD-CBF) for the 16-storey building.

Firstly, both office buildings were designed to resist the earthquake loads and to respond elastically to wind loads at each level following the provisions of NBC (2015) and the Steel Design Standard S16-2014. Hence, the buildings were designed according to the Equivalent Static Force procedure and the Wind Dynamic method. The notional loads and P- Δ effects were considered in the analysis while the accidental torsional effect was not accounted for. The capacity design approach was applied to seismic design to proportion the members attached to ductile fuses (e.g. braces).

Secondly, the performance of the designed buildings, at increasing levels of intensity, was assessed through nonlinear time history analysis using a set of seven artificial ground motions and five wind realizations generated from wind tunnel data. The assessment of buildings performance is based on the FEMA P695 (2009) procedure and the ASCE PBWD pre-standard. The seismic and wind Incremental Dynamic Analyses (IDA) were performed independently to predict the failure mechanism and to assess the collapse margin ratios (*CMR*) which is considered as an essential parameter in identifying the collapse safety of a structure and wind reliability acceptance criteria, respectively.

For the present research study, the following findings were concluded:

- The seismic response under design spectrum-compatible ground motions shows that nonlinearity occurs at lower demand than that associated to design. However, under the selected random wind events (Rand #1 - Rand #5) associated with the design level, the response is linear and dominated by the first mode.
- At the near collapse limit state, the damage in the 12-storey MD-CBFs with X-split braces initiates at the top two floors, then, for a slight increase in the input seismic load, the damage migrates to the bottom two floors where a two-storey failure mechanism is formed. The failure mechanism under earthquake loads is similar for the 16-storey LD-CBFs buildings. However, in the latter case, increased damage is observed at the upper two floors.
- The response of both buildings to increased wind load intensity associated to near collapse, is remarkably similar. Nonlinearity occurs at high intensity of wind excitations and it is characterized by accumulation of plastic strain in HSS braces of bottom floors, which eventually causes instability and leads the buildings to collapse. It is worth mentioning that failure caused by wind occurs for much smaller interstorey drifts ($< 1\%h_s$) when compared to the drift triggered by seismic ground motions.
- The performance under earthquake loads was assessed according to FEMA P695 (2009) methodology. The Incremental Dynamic Analysis (IDA) was implemented to estimate the median collapse capacity (\hat{S}_{CT}) and the Adjusted Collapse Margin Ratio ($ACMR$). It was shown that both steel buildings satisfy the collapse safety criteria ($ACMR > ACMR_{10\%}$). The IDA data served also for the construction of collapse fragility curves, relating the

intensity (spectral acceleration or reference wind velocity) to the probability of structural collapse.

- The wind reliability acceptance criterion, as defined in the ASCE wind pre-standard was also satisfied for both buildings. It is worth noting that conservatism in wind design is due to the codes approach, where the first significant yielding point is considered as an ultimate limit state for wind design of buildings. More flexibility could be permitted to wind design by accounting for the inherent structural overstrength and ductility, while challenging aspects may still arise due to inherent differences between earthquake and wind loads. From the case studied, a ductility-related force reduction factor applied to wind load can be considered as $R_w=2$ if nonlinear history response analysis is conducted.
- It is concluded that the studied 12-storey and 16-storey steel buildings designed for Montreal region are subjected to wind and earthquake events, where both are critical. This observation is significant for the multihazard assessment.

6.2 Future Work

This research focussed only on buildings of the same length-to-width ratio. Two different heights and one brace configuration, split-X bracing, were investigated. Future studies could explore this issue further by choosing different aspect ratios, taller buildings, other brace configurations and different Lateral Force Resisting Systems. Different locations in Canada shall be considered to explore the differences in multihazard design and assessment when one or both hazards are critical. In addition, the performance assessment can be expanded further to include economic losses caused by the damage under multihazard events, which is considered of great interest to stakeholders. Life cycle cost estimations shall include the evaluation of repair cost and downtime under strong winds,

when allowing for controlled plastic deformations of the CBF braces. This might prove an important area for future research.

7. REFERENCES

- Aguero, A., Izvernari, C., & Tremblay, R. (2006). "Modelling of the Seismic Response of Concentrically Braced Steel Frames Using the OpenSees Analysis Environment". *International Journal of Advanced Steel Construction*, 2, 242-274.
- American Society of Civil Engineers (ASCE). (2012). *Wind Tunnel Testing for Buildings and Other Structures*.
- ASCE. (2019). *Prestandard for Performance-Based Wind Design*. Reston, Virginia: ASCE/SEI.
- Aswegan, K., Larsen, R., Klemencic, R., Hooper, J., & Hasselbauer, J. (2017, April 6-8). "Performance-Based Wind and Seismic Engineering: Benefits of Considering Multiple Hazards". *Structures Congress*, 473-484.
- Athanasiou, A., Dakour, M., Pejmanfar, S., Tirca, L., & Stathopoulos, T. (2022,a). "Multihazard performance-based assessment framework for multi-story steel buildings". *ASCE Journal of Structural Engineering*, 148(6), 04022054.
- Athanasiou, A., Tirca, L., & Stathopoulos, T. (2020). "Discussion Paper on Performance-Based Wind-Resistant Optimization Design for Tall Building Structures" by Deng et al.(2019)". *Journal of Structural Engineering, ASCE*, 146(8).
- Athanasiou, A., Tirca, L., & Stathopoulos, T. (2022,b). "Nonlinear wind and earthquake loads on tall steel-braced frame buildings". *ASCE, Journal of Structural Engineering, in press*.
- Bezabeh, M. A., Bitsuamlak, G. T., & Tesfamariam, S. (2020). "Performance-based wind design of tall buildings: Concepts, frameworks, and opportunities". *WIND AND STRUCTURES*, 31(2), 103-142.

- Chuang, W.-C., & Spence, S. M. (2017). "A performance-based design framework for the integrated collapse and non-collapse assessment of wind excited buildings". *Engineering Structures*, 150, 746–758.
- Ciampoli, M., Petrini, F., & Augusti, G. (2011). "Performance-Based Wind Engineering: Towards a general procedure". *Structural Safety*, 33, 367–378.
- Cornell, C. A., & Krawinkler, H. (2000). "Progress and Challenges in Seismic Performance Assessment". *PEER Center News, Pacific Earthquake Engineering Research Center, Univ. of California, Berkeley, CA*.
- CSI ETABS. (2018). *Integrated Analysis and Design of Building Systems, Computers & Structures Inc. US*.
- Der Kiureghian, A. (2006, July 10-12). "Structural system reliability, revisited". *Proceedings, 3rd ASRANet International Colloquium, Glasgow, UK*.
- Duthinh, D., & Simiu, E. (2010, MARCH). "Safety of Structures in Strong Winds and Earthquakes: Multihazard Considerations". *Journal of Structural Engineering* © ASCE, 136(3), 330-333.
- EL Damatty, A. A., & Elezaby, F. (2018, August 27 - 31). "The integration of wind and structural engineering". *The 2018 World Congress on Advances in Civil, Environmental, & Materials Research (ACEM18)*.
- Ellingwood, B. R., Rosowsky, D. V., Li, Y., & Kim, J. H. (2004, December). "Fragility Assessment of Light-Frame Wood Construction Subjected to Wind and Earthquake Hazards". *Journal of Structural Engineering* © ASCE, 130(12), 1921-1930.

- Fajfar, P., & Krawinkler, H. (2004, September). "PERFORMANCE-BASED SEISMIC DESIGN CONCEPTS AND IMPLEMENTATION". *PEER Report 2004/05, Pacific Earthquake Engineering Research Center, University of California, Berkeley.*
- Federal Emergency Management Agency (FEMA). (2009). "*Quantification of Building Seismic Performance Factors.*" *FEMA P695, Washington, D.C.*
- Federal Emergency Management Agency (FEMA). (2012, 2018). "*Seismic performance 754 assessment of buildings*". *Volume 1. FEMA P58-1. Washington, D.C.*
- Fisher, J. W., Kulak, G. L., & Smith, I. F. (1997). 'A Fatigue Primer for Structural Engineers'. *Advanced Technologies for Large Structural Systems (ATLSS), Lehigh University; Bethlehem, Pennsylvania, USA.*
- Griffis, L., Patel, V., Muthukumar, S., & Baldava, S. (2012). "A Framework for Performance-based Wind Engineering". *ATC & SEI Conference on Advances in Hurricane Engineering.*
- Hsiao, P.-C., Lehman, D. E., & Roeder, C. W. (2012). "Improved analytical model for special concentrically braced frames". *Journal of Constructional Steel Research, 73, 80–94.*
- Hsiao, P.-C., Lehman, D. E., & Roeder, C. W. (2013). "A model to simulate special concentrically braced frames beyond brace fracture". *EARTHQUAKE ENGINEERING & STRUCTURAL DYNAMICS, 42, 183–200.*
- Jeong, S. Y., Alinejad, H., & Kang, T. H.-K. (2021). "Performance-Based Wind Design of High-Rise Buildings Using Generated Time-History Wind Loads". *Journal of Structural Engineering, 147(9), 04021134.*
- Judd, J. P. (2018). "Windstorm Resilience of a 10-Story Steel Frame Office Building". *ASCE-ASME J. Risk Uncertainty Eng. Syst., Part A: Civ. Eng, 4(3), 04018020.*

- KANG, Y.-J., & WEN, Y.-K. (2000). "Minimum Life-Cycle Cost Structural Design Against Natural Hazards". *Structural Research Series 629, University of Illinois*.
- Kleingesinds, S., Lavan, O., & Venanzi, I. (2021). "Life-cycle cost-based optimization of MTMDs for tall buildings under multiple hazards". *Structure and Infrastructure Engineering, 17*(2), 921–940.
- Li, Y., & Ellingwood, B. R. (2009, FEBRUARY). "Framework for Multihazard Risk Assessment and Mitigation for Wood-Frame Residential Construction". *Journal of Structural Engineering* © ASCE, *135*(2), 159-168.
- Lignos, D. G., & Karamanci, E. (2013, March 1-2). "PREDICTIVE EQUATIONS FOR MODELING CYCLIC BUCKLING AND FRACTURE OF STEEL BRACES". *10th International Conference on Urban Earthquake Engineering*.
- Lindt, J. W., & Dao, T. N. (2009, FEBRUARY). "Performance-Based Wind Engineering for Wood-Frame Buildings". *JOURNAL OF STRUCTURAL ENGINEERING* © ASCE, *135*(2), 169-177.
- Mahmoud, H., & Cheng, G. (2017). "Framework for Lifecycle Cost Assessment of Steel Buildings under Seismic and Wind Hazards". *Journal of Structural Engineering, 143*(3), 04016186.
- Matsuishi, M., & Endo, T. (1968). "Fatigue of metals subjected to varying stress". *Japan Society of Mechanical Engineers, Fukuoka, Japan, 68*(2), 37- 40.
- Mohammadi, A. (2016). "Wind Performance Based Design for High-Rise Buildings". *Doctoral dissertation, Dept. of Civil and Environmental Engineering, Florida International University , FIU Electronic Theses and Dissertations. 3032*. Retrieved from <https://digitalcommons.fiu.edu/etd/3032>.

- Mohammadi, A., Azizinamini, A., Griffis, L., & Irwin, P. (2019). "Performance Assessment of an Existing 47-Story High-Rise Building under Extreme Wind Loads". *Journal of Structural Engineering*, 145(1), 04018232.
- National Research Council of Canada. (2015). *National Building Code of Canada (NBC) and User's Guide – NBC 2015 Structural Commentaries (Part 4 of Division B), 2015, ON.*
- Nikellis, A., Sett, K., & Whittaker, A. S. (2019). "Multihazard Design and Cost-Benefit Analysis of Buildings with Special Moment–Resisting Steel Frames". *Journal of Structural Engineering*, 145(5), 04019031.
- PEER, Pacific Earthquake Eng. Research Center. (2015). *Open systems for earthquake engineering simulation (OpenSees).*
- Petrini, F., Ciampoli, M., & Augusti, G. (2009, July 19–23). "A probabilistic framework for Performance-Based Wind Engineering". *5th European & African Conference on Wind Engineering.*
- Petrini, F., Gkoumas, K., Rossi, C., & Bontempi, F. (2020). "Multi-Hazard Assessment of Bridges in Case of Hazard Chain: State of Play and Application to Vehicle-Pier Collision Followed by Fire". *Frontiers in Built Environment*, 6, 580854.
- Porter, K. A. (2003, July 6-9). "An Overview of PEER's Performance-Based Earthquake Engineering Methodology". *Ninth International Conference on Applications of Statistics and Probability in Civil Engineering (ICASP9).*
- Song, J., Kang, W.-H., Lee, Y.-J., & Chun, J. (2021). "Structural System Reliability: Overview of Theories and Applications to Optimization". *ASCE-ASME J. Risk Uncertainty Eng. Syst., Part A: Civ. Eng.*, 7(2), 03121001.

- Spence, S. M., & Kareem, A. (2014). "Performance-based design and optimization of uncertain wind-excited dynamic building systems". *Engineering Structures*, 78, 133–144.
- Suksuwan, A., & Spence, S. M. (2018). "Performance-based multi-hazard topology optimization of wind and seismically excited structural systems". *Engineering Structures*, 172, 573–588.
- Tirca, L., Chenb, L., & Tremblay, R. (2015). "Assessing collapse safety of CBF buildings subjected to crustal and subduction earthquakes". *Journal of Constructional Steel Research*, 115, 47–61.
- Tirca1, L., & Chen, L. (2014). "NUMERICAL SIMULATION OF INELASTIC CYCLIC RESPONSE OF HSS BRACES UPON FRACTURE". *Advanced Steel Construction*, 10(4), 442-462.
- Tokyo Polytechnic Aerodynamic Database TPU. (2021). Retrieved from TPU: <http://wind.arch.tokouei.ac.jp/system/eng/contents/code/tpu>
- TRIFUNAC, M. D., & BRADY, A. G. (1975). "A Study on the Duration of Strong Earthquake Ground Motion". *Bulletin of the Seismological Society of America*, 65(3), 581-626.
- Uriz, P. (2005). "Towards Earthquake Resistant Design of Concentrically Braced Steel Buildings". *Ph.D. Dissertation, University of California, Berkeley*.
- Uriz, P., & Mahin, S. A. (2008, NOVEMBER). "Toward Earthquake-Resistant Design of Concentrically Braced Steel-Frame Structures". *PACIFIC EARTHQUAKE ENGINEERING RESEARCH CENTER (PEER)*. University of California, Berkeley.
- Vamvatsikos, D., & Cornell, C. A. (2002). "Incremental dynamic analysis". *EARTHQUAKE ENGINEERING AND STRUCTURAL DYNAMICS*, 31, 491–514.

- Venanzi, I., Lavan, O., Ierimonti, L., & Fabrizi, S. (2018). "Multi-hazard loss analysis of tall buildings under wind and seismic loads". *Structure and Infrastructure Engineering*, 14(10), 1295–1311.
- Wen, Y. K., & Kang, Y. J. (2001, MARCH). "MINIMUM BUILDING LIFE-CYCLE COST DESIGN CRITERIA". *JOURNAL OF STRUCTURAL ENGINEERING*, 127(3), 330-337 & 338-346.
- Yang, F., & Mahin, S. A. (2005). "Limiting Net Section Failure in Slotted HSS Braces". *Structural Steel Education Council, Moraga, CA*.
- Zaghi, A. E., Padgett, J. E., Bruneau, M., Barbato, M., Li, Y., Mitrani-Reiser, J., & McBride, A. (2016). "Establishing Common Nomenclature, Characterizing the Problem, and Identifying Future Opportunities in Multihazard Design". *Journal of Structural Engineering*, 142(12), H2516001.